

THE CALCULATION OF
THEORETICAL CHROMOSPHERIC MODELS AND
THE INTERPRETATION OF
SOLAR SPECTRA FROM ROCKETS AND SPACECRAFT

NASA Grant NSG-7054

Semiannual Report No. 20 and 21

For the period 1 January 1985 through 30 June 1985
and the period 1 July 1985 through 31 December 1985

Principal Investigator
Eugene H. Avrett

February 1986

Prepared for
National Aeronautics and Space Administration
Washington, D.C. 20546

Smithsonian Institution
Astrophysical Observatory
Cambridge, Massachusetts 02138



The Smithsonian Astrophysical Observatory
is a member of the
Harvard-Smithsonian Center for Astrophysics

The NASA Technical Officer for this grant is Dr. Tomas Gergely, Code
EZ-7, Headquarters, National Aeronautics and Space Administration,
Washington, D.C. 20546.

N86-20995

Unclas
05579

G3/46

(NASA-CR-176573) THE CALCULATION OF
THEORETICAL CHROMOSPHERIC MODELS AND THE
INTERPRETATION OF SOLAR SPECTRA FROM ROCKETS
AND SPACECRAFT Semiannual Report, 1 Jan. -
31 Dec. 1985. (Smithsonian Astrophysical

THE CALCULATION OF
THEORETICAL CHROMOSPHERIC MODELS AND
THE INTERPRETATION OF
SOLAR SPECTRA FROM ROCKETS AND SPACECRAFT

NASA Grant NSG-7054

Semiannual Report No. 20 and 21

For the period 1 January 1985 through 30 June 1985
and the period 1 July 1985 through 31 December 1985

Principal Investigator
Eugene H. Avrett

February 1986

Prepared for
National Aeronautics and Space Administration
Washington, D.C. 20546

Smithsonian Institution
Astrophysical Observatory
Cambridge, Massachusetts 02138

The Smithsonian Astrophysical Observatory
is a member of the
Harvard-Smithsonian Center for Astrophysics

The NASA Technical Officer for this grant is Dr. Tomas Gergely, Code
EZ-7, Headquarters, National Aeronautics and Space Administration,
Washington, D.C. 20546.

THE CALCULATION OF
THEORETICAL CHROMOSPHERIC MODELS AND
THE INTERPRETATION OF
SOLAR SPECTRA FROM ROCKETS AND SPACECRAFT

NASA Grant NSG-7054
Semiannual Report No. 20 and No. 21

This year we have been completing improved versions, begun last year, of the multi-component VAL solar models that include opacities for 17 million atomic and molecular lines computed by Kurucz. These models now produce a consistent match to observations in the ultra-violet and far infrared and to the Ca H and K lines. We are preparing a large paper for the Astrophysical Journal. The same techniques have now been applied to chromospheric flare models in collaboration with Marcos Machado. Avrett discussed this work at the flare workshop at Sac Peak in August and at the SOT meeting in Munich in September. A preprint for the Sac Peak proceedings by Avrett, Machado, and Kurucz is appended to this report. Figure 1 shows the calculated spectra from models of the quiet solar disk and a very bright flare region, at disk center and at $\mu = 0.3$ near the limb, in 1 nm bandpasses centered at 361, 386.2, and 427.5 nm. The 386.2 and 427.5 nm bands are both located in the Paschen continuum, and respond in roughly the same way to hydrogen emission, but the 386.2 band has a greater sensitivity to line emission in a strong flare, particularly near the limb. The 361 band is in the Balmer continuum and shows substantial hydrogen emission as a result of chromospheric overheating. The limb enhancement at 361 nm is several times stronger than at disk center. The calculations are in general agreement with flare observations. The calculations in the appended report suggest that the enhanced emission due to chromospheric overheating can lead to radiative heating deeper in the atmosphere.

This year we have continued to work on models and spectra of sunspots in collaboration with Per Maltby and Olav Kjeldseth-Moe of the Institute for Theoretical Astrophysics in Oslo. Kjeldseth-Moe is analyzing the sunspot observations in the ultraviolet region 140-168 nm obtained by the NRL High Resolution Telescope and Spectrograph. Maltby has made extensive photometric observations of sunspot umbrae and penumbrae in 10 channels covering the wavelength region 387-3800 nm. The paper "A new sunspot umbral model and its variation with the solar cycle" by Maltby, Avrett, Carlsson, Kjeldseth-Moe, Kurucz, and Loeser has been accepted for publication in the Astrophysical Journal. Figure 2 is taken from that paper. It shows the calculated disk and spot spectra, the calculated atmospheric transmission spectrum, the calculated transmitted disk and spot spectra, the calculated instrumentally degraded transmitted disk and spot spectra, and finally, the observed disk and spot spectra from Hall's sunspot atlas. We are continuing to work on detailed calculation of the spectrum and comparison with observations. The Oslo group is also reducing HRTS data for other solar features and they plan to make those data available to us. Maltby is visiting Cambridge during January so that we can plan for the calculations necessary to analyze the data.

Kurucz spent November and December at Los Alamos working on atomic and molecular opacities, but significant Cray time was not available. We cannot plan on getting Cray time in the future because Los Alamos computers are becoming more saturated. There is unlimited VAX time available, however. Kurucz has not been able to get access to large computers at any other laboratory. It would be very helpful if there were some way that NASA could provide us with computer time. Kurucz has applied to NSF for supercomputer time at San Diego for 1986 but he has not yet received an answer.

There are several regions between 200 and 350 nm where the predicted solar intensities are several times higher than observed, e.g., 85% line blocking predicted instead of the 95% observed. The integrated flux error of these regions is several per cent of the total. Kurucz has determined that this discrepancy is caused by missing iron group atomic lines that go to excited configurations that have not been observed in the laboratory. Most laboratory work has been done with emission sources that cannot strongly populate these configurations. The sun, however, shows these lines in absorption without difficulty.

Kurucz has used Cowan's Hartree-Fock programs at Los Alamos to compute Slater single-configuration and configuration-interaction integrals for the lowest 50 configurations of the first 10 stages of ionization for elements up through Zn and for the first 5 stages for heavier elements. These calculations are used to determine eigenvectors by combining least squares fits for levels that have been observed with computed integrals for higher configurations. Each least squares iteration takes a large amount of computer time and many iterations are required. Thus far new line lists have been completed only for Fe I and II, which produce the strongest effect on the spectrum. Cr I and II and Ni I and II are still in the least squares fitting phase. Other less abundant elements have not yet been started, but they should play only a secondary role in the opacity, in any case, and will be easier to compute because most of them have simpler spectra. Radiative, Stark, and van der Waals damping constants and Lande g values are automatically produced for each line. The complexity of these calculations is illustrated by the following table,

	Fe I		Fe II	
	even	odd	even	odd
number of configurations	26	20	22	16
number of levels	5401	5464	5723	5198
largest Hamiltonian matrix	1069	1094	1102	1049
number of least squares parameters	963	746	729	541
(many fixed at scaled HF)				
total number of lines saved	583,814		1,112,322	

Figure 3 shows the blocking in the solar ultraviolet spectrum produced by Fe lines. The calculation was done once with the old line data mentioned above and again with the newly calculated data. The increase in opacity is dramatic. Once the calculations for the iron group elements are complete, Kurucz will recompute the opacity tables for use in our model calculations.

We made very little progress on molecules in 1985 because of the large effort needed for the atomic calculations.

Kurucz is now reducing the center and limb intensity spectra in the visible that were taken with the FTS at Kitt Peak to produce an atlas like the Kurucz, Furenlid, Brault, and Testerman Solar Flux Atlas that he published this year. He has also begun to remove the terrestrial lines from the flux spectrum to determine the spectrum above the atmosphere. In collaboration with the UVSP group Kurucz is also reducing SMM spectra that cover the whole ultraviolet from Lyman alpha to 350 nm.

Figure 1

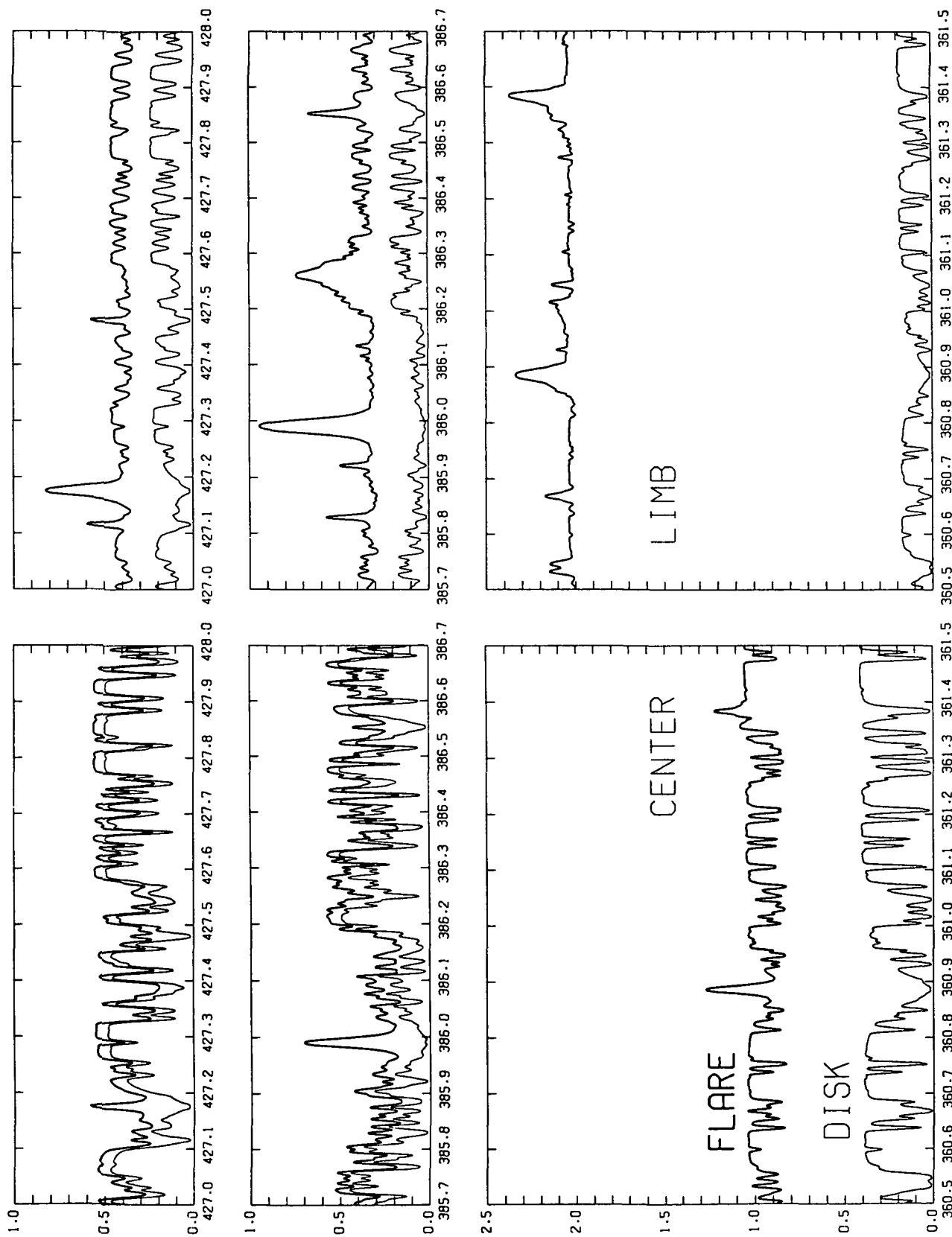


Figure 2

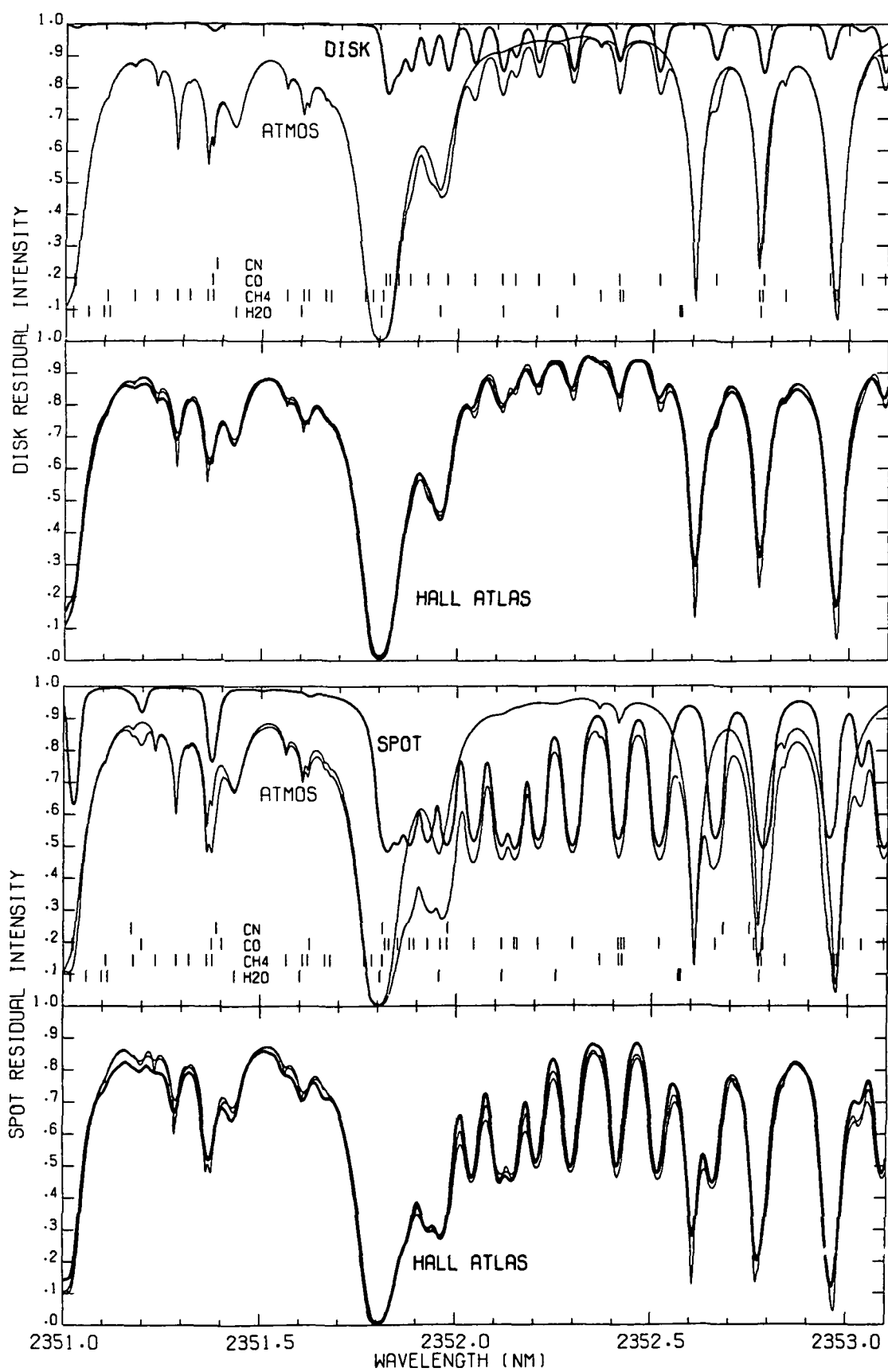
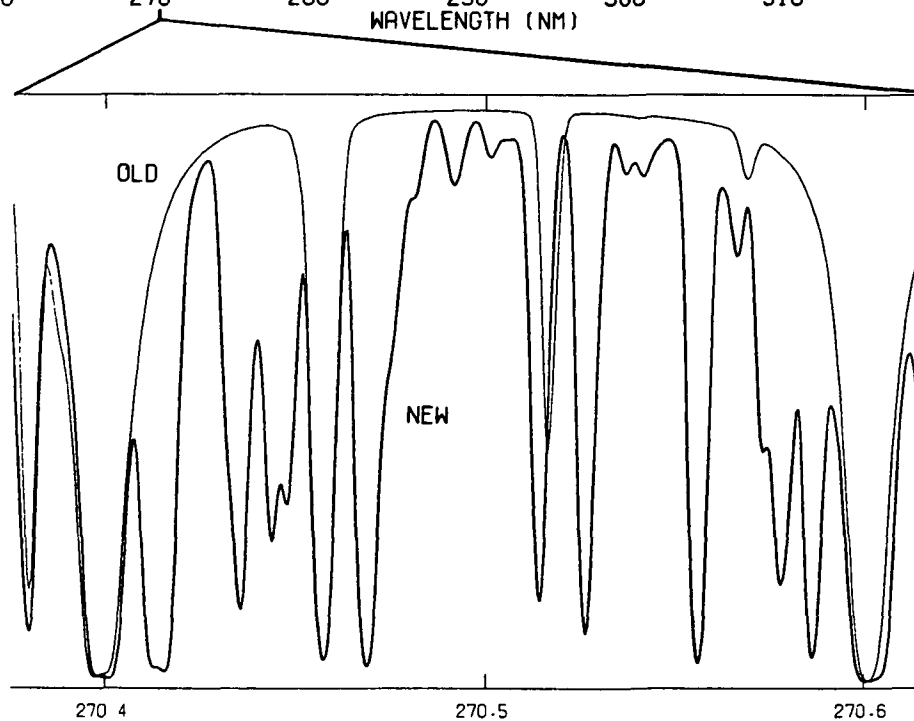
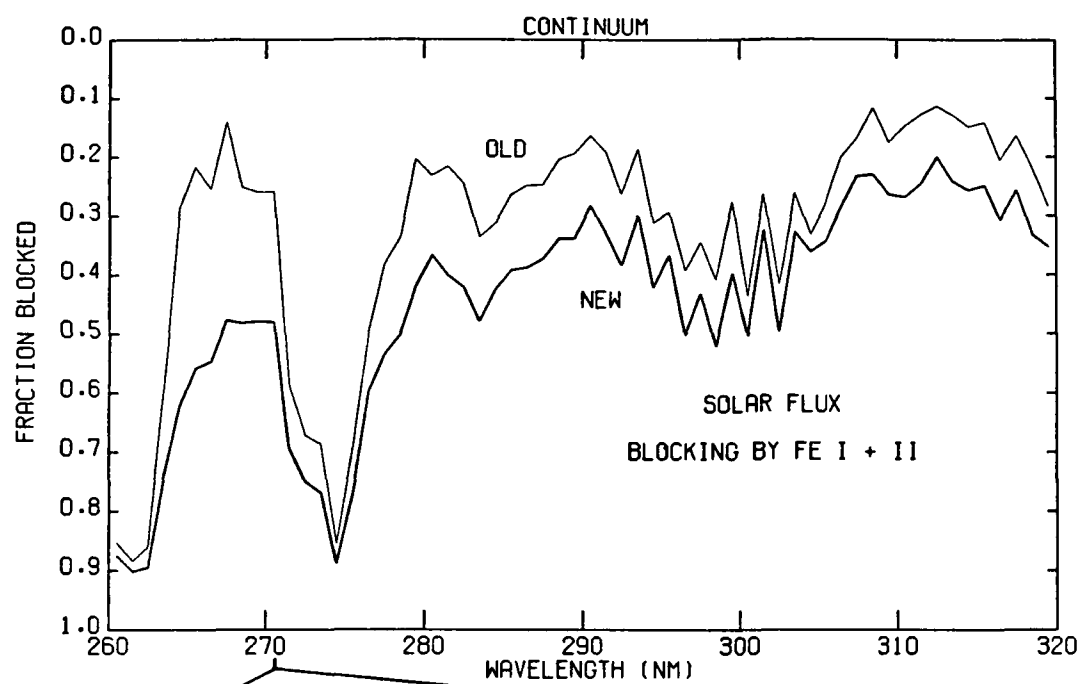


Figure 3



CHROMOSPHERIC FLARE MODELS

EUGENE H. AVRETT

Harvard-Smithsonian Center for Astrophysics
60 Garden Street, Cambridge, MA 02138, USA

MARCOS E. MACHADO

Space Science Laboratory, ES52, Marshall Space Flight Center
Huntsville, AL 35812, USA
NAS/NRC Research Associate, on leave from CNIE, Argentina

and

ROBERT L. KURUCZ

Harvard-Smithsonian Center for Astrophysics
60 Garden Street, Cambridge, MA 02138, USA

ABSTRACT

We present further calculated results based on the two chromospheric flare models F1 and F2 of Machado *et al* (1980). Two additional models are included: F1* which has enhanced temperatures relative to the weak-flare model F1 in the upper photosphere and low chromosphere, and F3 which has enhanced temperatures relative to the strong-flare model F2 in the upper chromosphere. Each model is specified by means of a given variation of the temperature as a function of column mass. The corresponding variation of particle density and the geometrical height scale are determined by assuming hydrostatic equilibrium. We solve the coupled equations of statistical equilibrium and radiative transfer for H, H⁻, He I-II, C I-IV, Si I-II, Mg I-II, Fe, Al, O I-II, Na, and Ca II. The overall absorption and emission of radiation by lines throughout the spectrum is

determined by means of a reduced set of opacities sampled from a compilation of over 10^7 individual lines. For the flare models and quiet-Sun model C we show 1) the computed depth variation of the electron number density and the number density of hydrogen in the $n=2$ level, 2) Lyman continuum intensities, 3) intensity distributions over the wavelength range 1500 to 8500Å, 4) spectra computed in detail in 10Å bands centered at 3610, 3862, and 4275Å, 5) computed line profiles for 26 selected lines, from 304 to 10830Å, produced by H, He I-II, Na, Mg I-II, Ca II, Si I-II, Fe, C I-IV, and O I-II, and 6) the net radiative cooling rates due to H, H⁺, Ca II, Mg II, Fe, Na, Mg, Si, C, and He I-II.

We show that the white light flare continuum may arise by extreme chromospheric overheating as well as by an enhancement of the minimum temperature region. These two possibilities, which have been discussed in many previous papers, are treated here with the help of detailed semiempirical models. The model calculations show the relationship between observations and atmospheric parameters, and provide estimates of the energy needed to produce flare enhancements.

The radiative cooling rate calculations for our brightest flare model suggest that chromospheric overheating provides enhanced radiation that could cause significant heating deep in the flare atmosphere.

1. INTRODUCTION

Semiempirical modeling of flare atmospheres, even in the static plane-parallel approximation, gives useful information about the physical properties of solar flares. In semiempirical modeling we assume a temperature distribution, calculate the remaining atmospheric parameters at each height, and then calculate the emergent spectrum. We try to select a temperature distribution leading to an emergent spectrum that agrees with observations.

We do not specify the flare heating mechanism that produces the atmospheric stratification; but solve the equations of statistical equilibrium and radiative transfer, for all the required spectral lines and continua, in order to understand how various observable spectral features correspond to the physical characteristics of the atmosphere.

In addition, the model calculations give a detailed description of the depth variation of the net energy losses due to radiation that must be balanced by various nonradiative heating and transport mechanisms, such as electron and proton acceleration, heat conduction, and XUV irradiation (see Emslie, *et al* 1981; Henoux and Nakagawa 1977; Machado, *et al* 1978, 1980). Kinetic-energy and enthalpy fluxes also must be considered. See the summaries by Canfield and Machado in this volume. The model calculations also indicate that under certain conditions radiative heating can occur deep in the flare atmosphere. See Aboudarham and Henoux (1985) and the papers by Emslie and by Mauas and Machado in this volume.

In this paper we address two particular aspects of chromospheric flare observations in relation to model calculations:

a) the origin of white light flare (WLF) events, in view of the improved observations in recent years (Neidig and Cliver 1983), and the recognition that some white light flares correspond to the brightest flares seen in the narrow wavelength bandpasses of strong spectral lines; and

b) how a variety of spectral lines, observed in different regions of the spectrum (some never analyzed in detail) respond to varying atmospheric conditions.

In order to study WLF events, we show results from the F1 (weak flare) and F2 (strong flare) models of Machado *et al.* (1980, hereafter MAVN) and two new models F1* and F3 depicted in Figure 1. Figure 1 also shows quiet-Sun model C from Vernazza *et al.* (1981, hereafter VAL), but with the higher temperatures in the minimum region discussed by Avrett, Kurucz, and Loeser (1984) and Avrett (1985) (see also the photospheric model tabulated by Maltby *et al.* 1986).

Model F3 is our attempt to mimic, and explore the consequences of, a dense overheated region in the upper chromosphere as some WLF observations suggest (see Machado *et al.* in these proceedings and references therein; Neidig and Wiborg 1984; Donati-Falchi *et al.* 1984). In this case, hydrogen free-bound emission is found to be the major source of continuum enhancement.

Observations of some WLF events show only moderately broadened Balmer lines and a weak enhancement at the head of the Balmer continuum (Hiei 1982; Boyer *et al.* 1985). These observations suggest that H^- could be the main contributor to the flare continuum at visible wavelengths. We explore this possibility with the help of model F1* which is the F1 weak-flare model except for higher temperatures in the upper photosphere and temperature minimum region.

With regard to point (b) above, we note that in recent years there have been few additional observations of the spectral features used by MAVN to determine models F1 and F2 (the Lyman lines and continuum, and the C I and Si I continua). On the other hand, a wealth of new data exists mainly at visible wavelengths, as well as more detailed analyses of He I-II features in the visible and extreme ultraviolet ranges. (See the papers by Lites *et al.*, Porter *et al.* and Zirin in this volume, and references therein.) Also there have been improvements in opacity data and computational techniques that enable us to compute spectra in better detail than in earlier years. (See Kurucz 1985; Avrett 1985.) Thus we have computed for model C and for all four flare models the profiles of a large number of lines at a variety of wavelengths. The comparison of these profiles with observations should help determine the atmospheric properties of flare regions and the physical processes that occur in flares.

2. MODEL CALCULATIONS

Given any of the temperature distributions shown in Figure 1, we obtain the density distribution and a geometrical height scale from the equation of hydrostatic equilibrium (see VAL 1973 and 1981). Figure 1 shows temperature as a function of column mass $m(\text{g cm}^{-2})$. The total pressure is given by $p(\text{dyn cm}^{-2}) = mg$, where $g = 2.74 \times 10^4 \text{ cm s}^{-2}$. Computed values of geometrical height in km are shown in each case. In each of the flare model calculations we have chosen, for simplicity, to use the same turbulent pressure as a function of height as used in the VAL (1981) model C calculation.

We determine the excitation and ionization of hydrogen and other atoms and ions by solving the equations of statistical equilibrium and radiative transfer. The electron number density n_e is needed to solve these equations, but is not known in advance. Successive ionization-equilibrium calculations are carried out for H, He, C, Si, Mg, Fe, and other electron donors until self-consistent values of n_e are obtained. The photoionization rates in these calculations depend on level populations and radiation intensities, two quantities having a global interdependence that we determine by solving the coupled equations of statistical equilibrium and radiative transfer. Since the photoionization rates also depend on the opacity as a function of wavelength, we must know the ionization equilibrium of all continuum-opacity contributors, and must properly represent all the lines that fill the spectrum. The way we represent the line opacity is discussed in the next section.

Figure 2 shows the electron number density distribution computed from each model. Figure 3 shows the computed number density for the hydrogen $n = 2$ level, and the corresponding column density.

Given the electron and hydrogen densities and the temperature as functions of height, we calculate the emergent Lyman continuum intensities shown in Figure 4. Other spectrum calculations are given in the following sections.

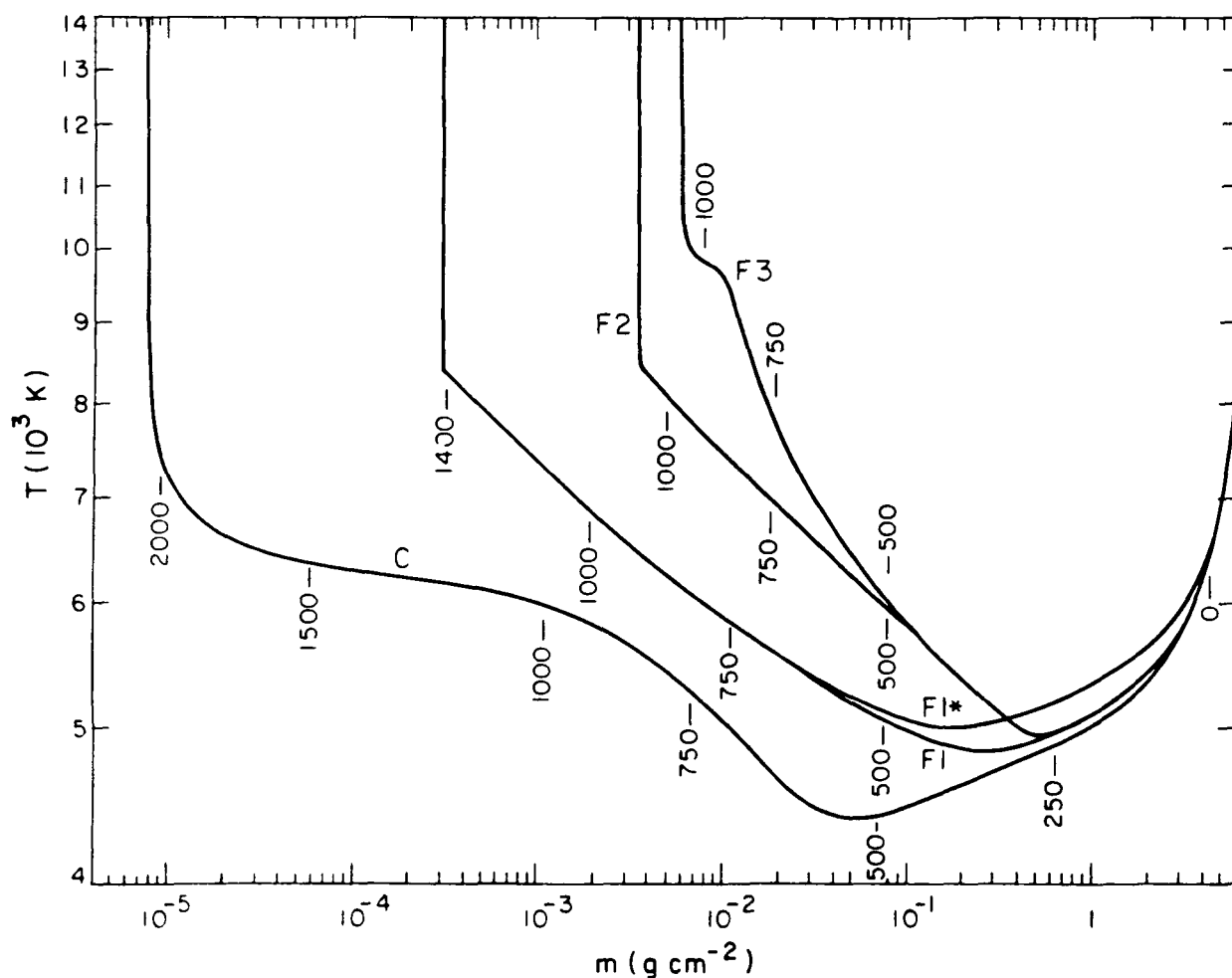


Fig. 1 - Temperature as a function of column mass for the quiet-Sun model and the four flare models. Geometrical heights in km are indicated in each case.

3. SPECTRUM CALCULATIONS

Kurucz (1985) has compiled opacity data for over 1.7×10^7 atomic and molecular lines. His line list can be used to synthesize the spectrum in detail for limited wavelength regions, as in Figure 6 shown later. A very large amount of computer time would be needed to synthesize the entire solar spectrum in this way. As a simplification, Kurucz has used the full line list to obtain the total line opacity at a uniform set of frequencies $\Delta\nu = 2 \times 10^{-4} \nu$ (corresponding to $\Delta\lambda \sim 1\text{\AA}$ in the visible and ultraviolet). In the wavelength range between the Lyman limit and $10\text{ }\mu\text{m}$ we obtain the total line opacity sampled at about 23,000 frequencies. This is still too large a number of frequencies to use for exploratory calculations. Moreover, some of the sampled frequencies occasionally will occur near the centers of strong lines, giving unusually large opacity values.

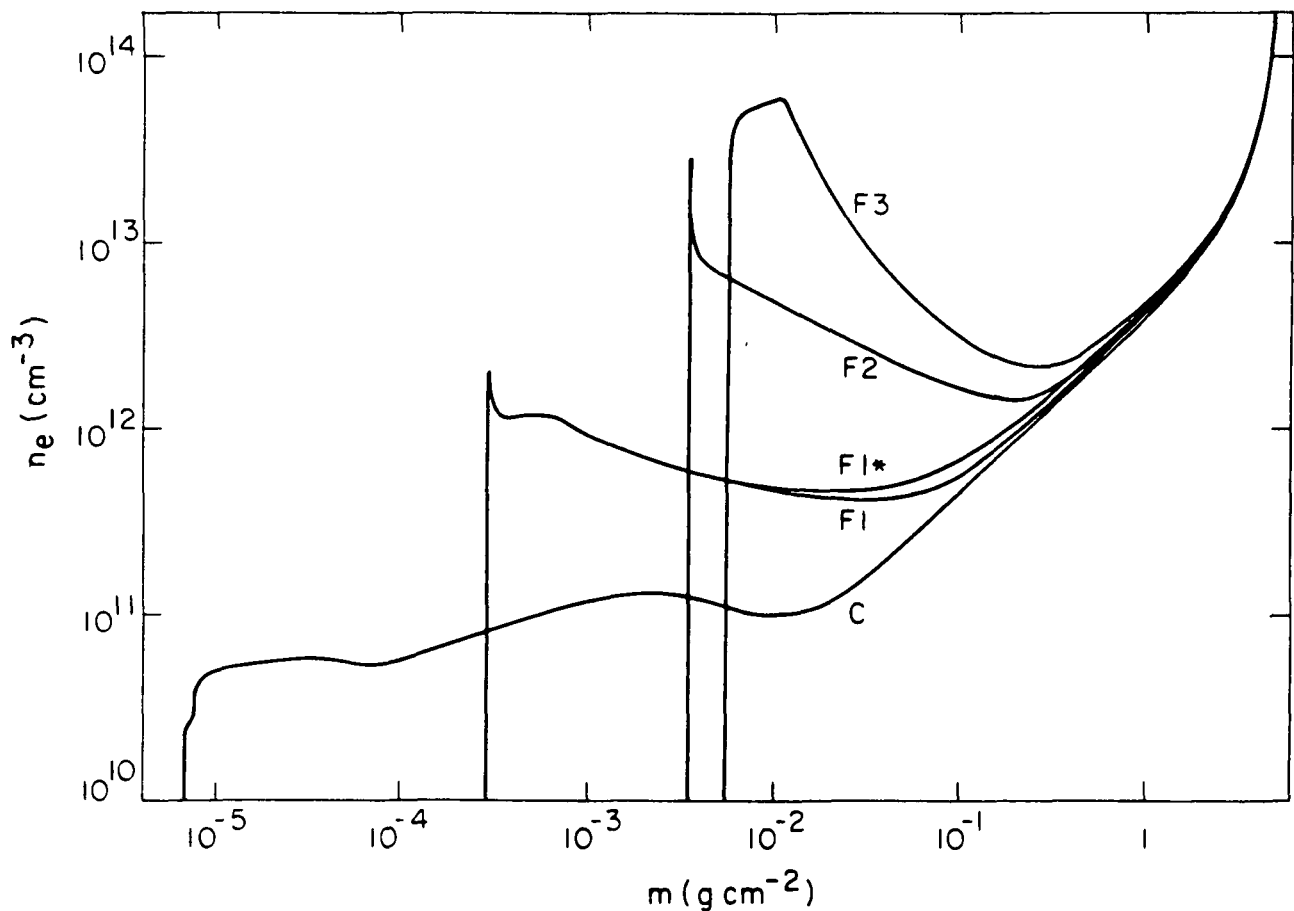


Fig. 2 - The calculated electron number density as a function column mass for each model.

For these reasons, we use a new approximate treatment of line opacity which differs from ordinary opacity sampling and from the use of distribution functions. In this treatment, every 100 of Kurucz's sampled values are replaced by five representative ones chosen as follows. The 100 values are arranged in order, from lowest to highest opacity. Then we choose those numbered 10, 30, 50, 70, and 90 from the sequence. These five values are assigned to frequencies uniformly distributed over the original interval, but in the order in which they occurred in the original sample. The selected opacity values thus are kept reasonably close to their original frequencies. The original sampled opacities are

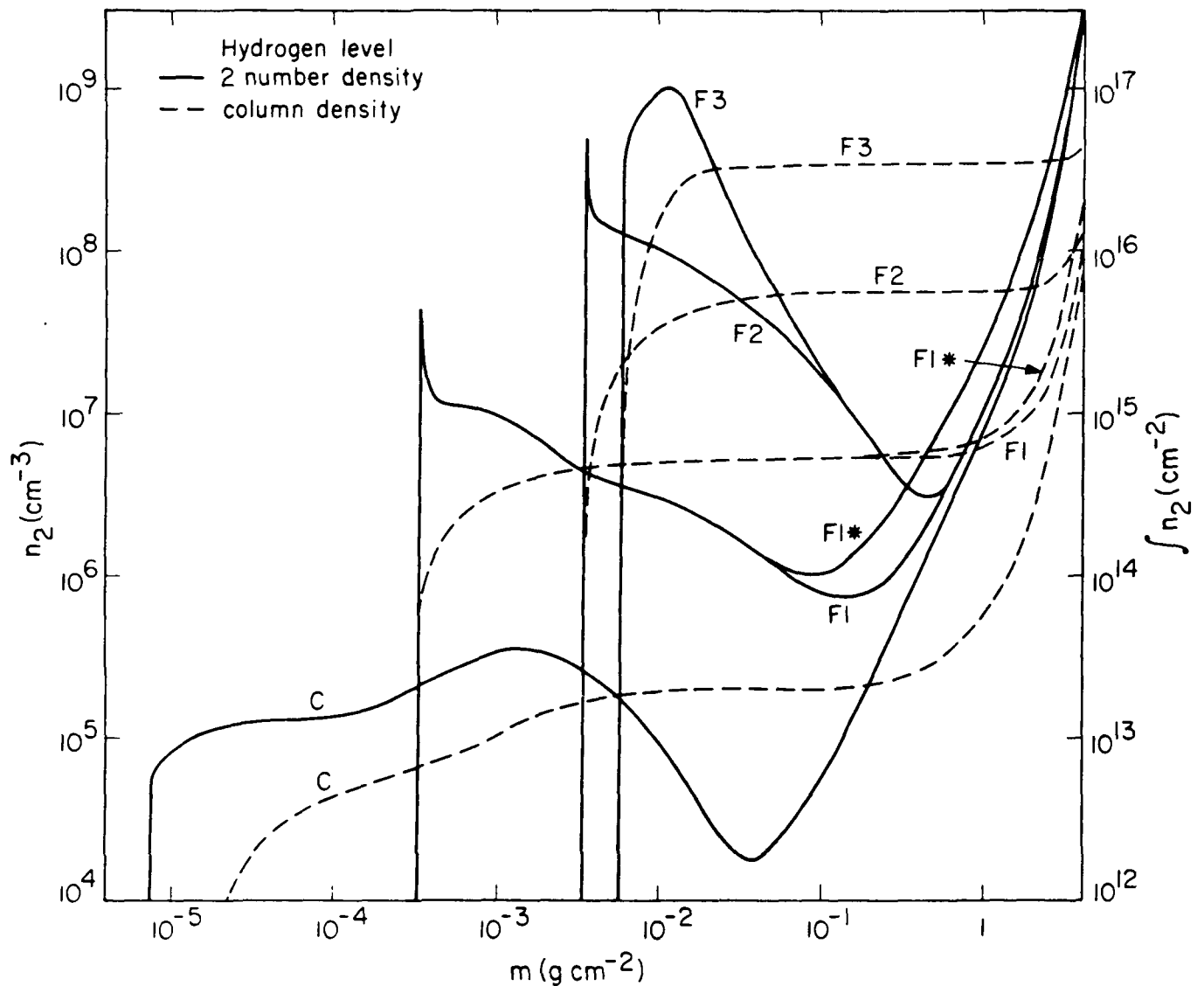


Fig. 3 - The hydrogen n_2 number density and the corresponding n_2 column density calculated for each model.

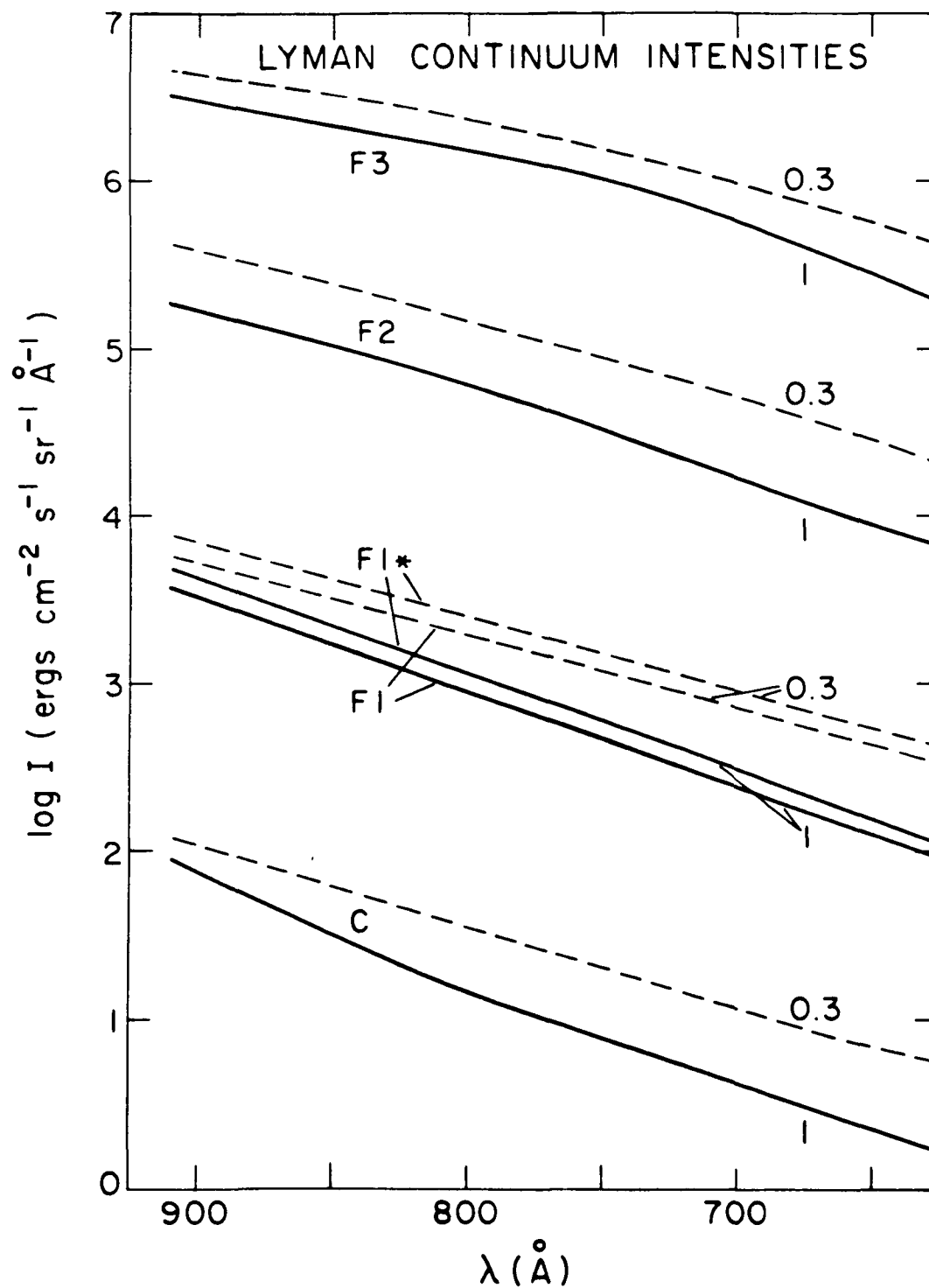


Fig. 4 - Intensity in the hydrogen Lyman continuum, from the center ($\mu = 1$) and limb ($\mu = 0.3$) of the solar disk for each model.

tabulated as functions of temperature and pressure. From the values of temperature and pressure at each depth in a model, we interpolate to find each group of 100 sampled values and then determine the five representative ones. At each depth, the five representative values are obtained independently, and are independently assigned to the five uniformly spaced frequencies in their original order. In this way we avoid assigning all the largest opacities at each depth to one frequency and all the smallest opacities at each depth to another. Associating large (or small) opacities at one depth with the large (or small) opacities at other depths is a disadvantage of the method of line opacity distribution functions (see Carbon 1984).

It is necessary to explain a further important feature of the calculations before showing the results. We cannot assume LTE and use the Planck function as the source function corresponding to line opacities; enormously strong chromospheric emission lines would result. While we calculate the non-LTE source functions for many individual lines, it is impractical to identify each of our representative lines and then explicitly calculate these source functions. In order to obtain a reasonable set of results to study, the scattering albedo α is introduced such that the source function S_ν corresponding to our representative lines is given by

$$S_\nu = \alpha J_\nu + (1 - \alpha) B_\nu$$

where B_ν is the Planck function, J_ν is the calculated mean intensity, and α is a given function of depth. We let

$$\alpha = \begin{cases} 0, & h \leq h_1, \\ (h-h_1)/(h_2-h_1), & h_1 < h < h_2, \\ 1, & h \geq h_2. \end{cases}$$

In the four flare model calculations we chose h_1 as the height where the temperature has a minimum value and h_2 as the height at the base of the chromosphere-corona transition region. The calculated line emission should be compared with flare observations to see if this variation of α is reasonable. For model C we have chosen $h_2 = 700$ km (and $h_1 = 200$ km) after finding that a larger h_2 (*e.g.*, 1000 km) gives too many strong ultraviolet emission lines in comparison with quiet-Sun observations. We need to compare our results with ultraviolet flare observations to determine whether or not our adopted values of h_2 in the flare model calculations also should be reduced (*e.g.*, see the paper by Foing *et al.* in this volume).

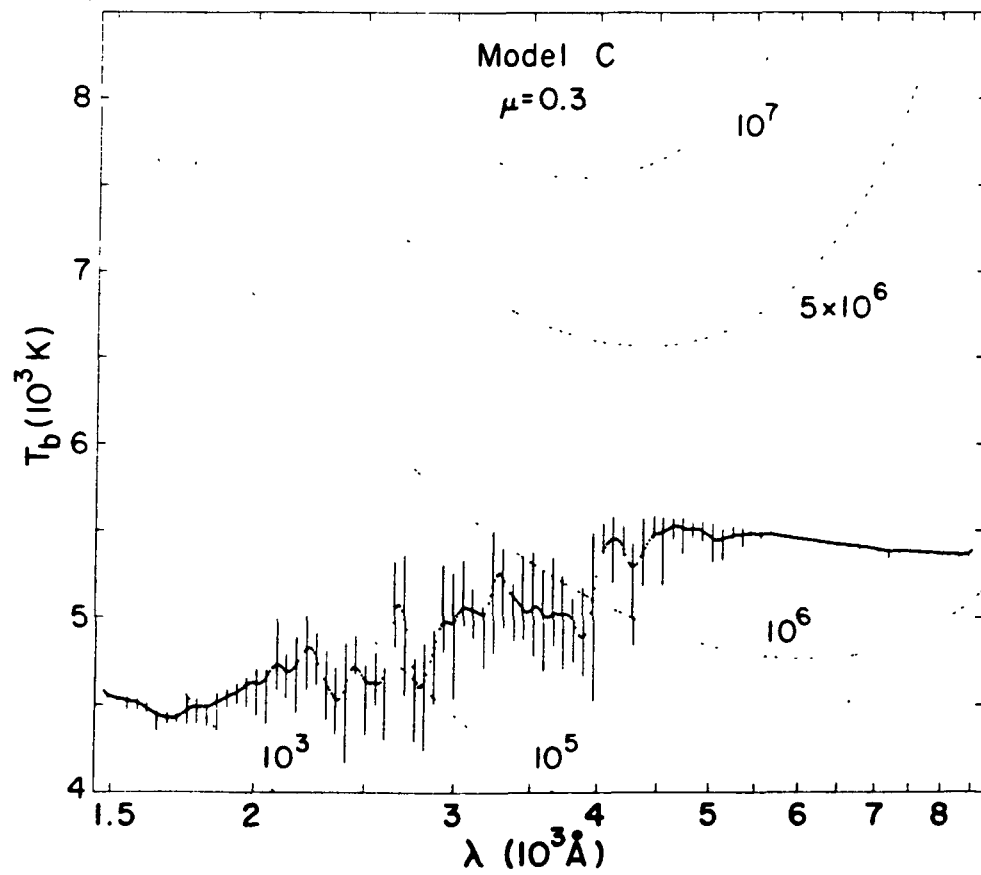
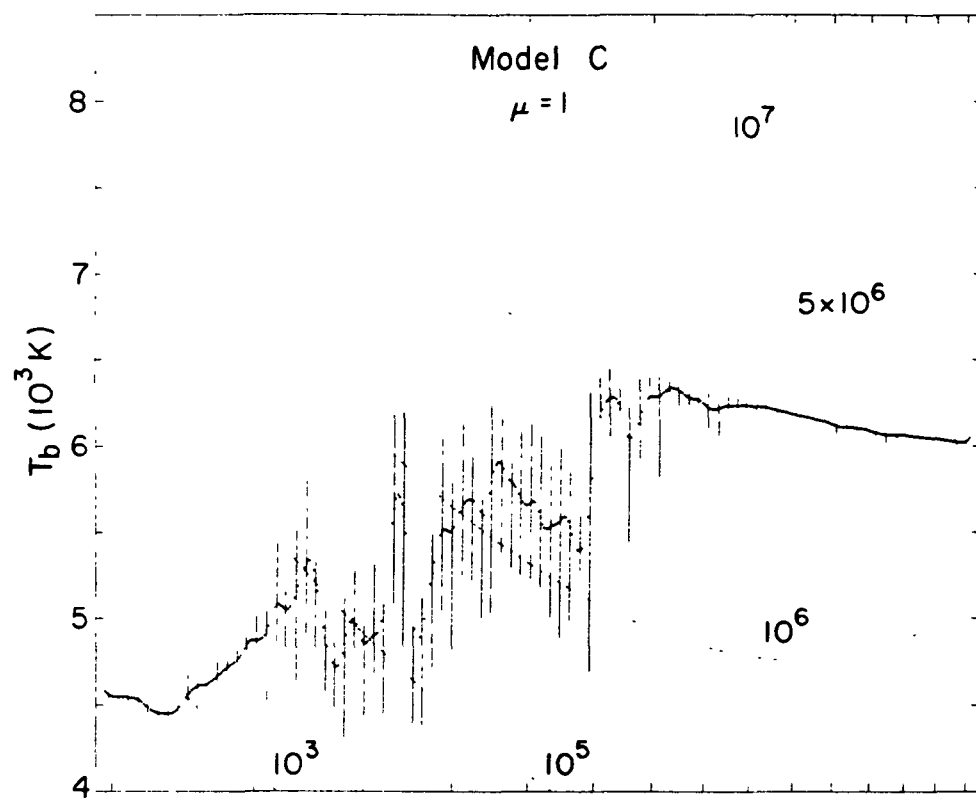
4. RESULTS

Figure 5 shows the calculated emergent intensity distribution over the wavelength range 1500-8500Å, at the disk center and at $\mu = 0.3$, for models C, F1, F1*, F2, and F3. The results are plotted as brightness temperature vs. wavelength, and intensity values in $\text{ergs cm}^{-2} \text{s}^{-1} \text{sr}^{-1} \text{Å}^{-1}$ are plotted for reference. The results for models C, F1 and F1* are shown in Figures 5a, 5b, and 5c, and compared in Figure 5d. The intensity ratios $I(\text{F1})/I(\text{C})$ and $I(\text{F1}^*)/I(\text{C})$ are plotted in Figure 5e. The results for models F2 and F3 are shown in Figures 5f and 5g, and are compared (along with C and F1) in Figure 5h. The ratios $I(\text{F1})/I(\text{C})$, $I(\text{F2})/I(\text{C})$, and $I(\text{F3})/I(\text{C})$ are plotted in Figure 5i. The vertical lines in Figures 5a, b, c, f, and g indicate the maximum intensity and minimum intensity in each group of five frequencies as explained above. The dotted curve is obtained by successively averaging neighboring intensity values until a smooth distribution is obtained. Figures 5d, e, h, and i show only these smooth distributions.

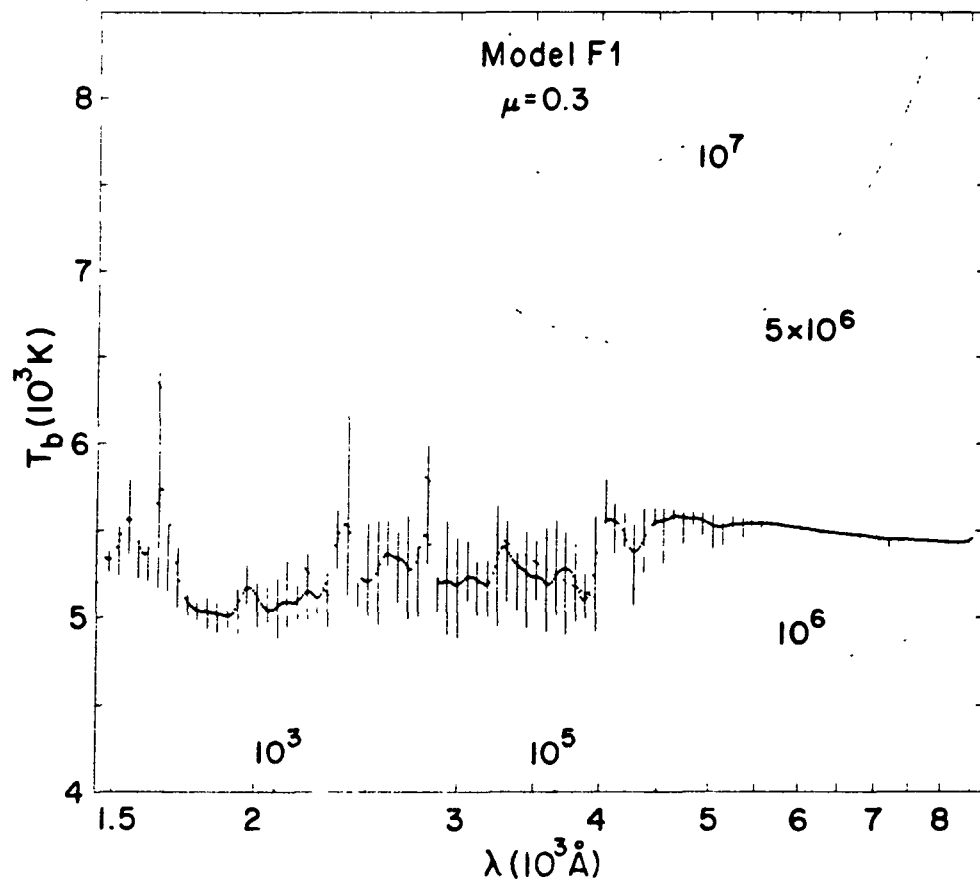
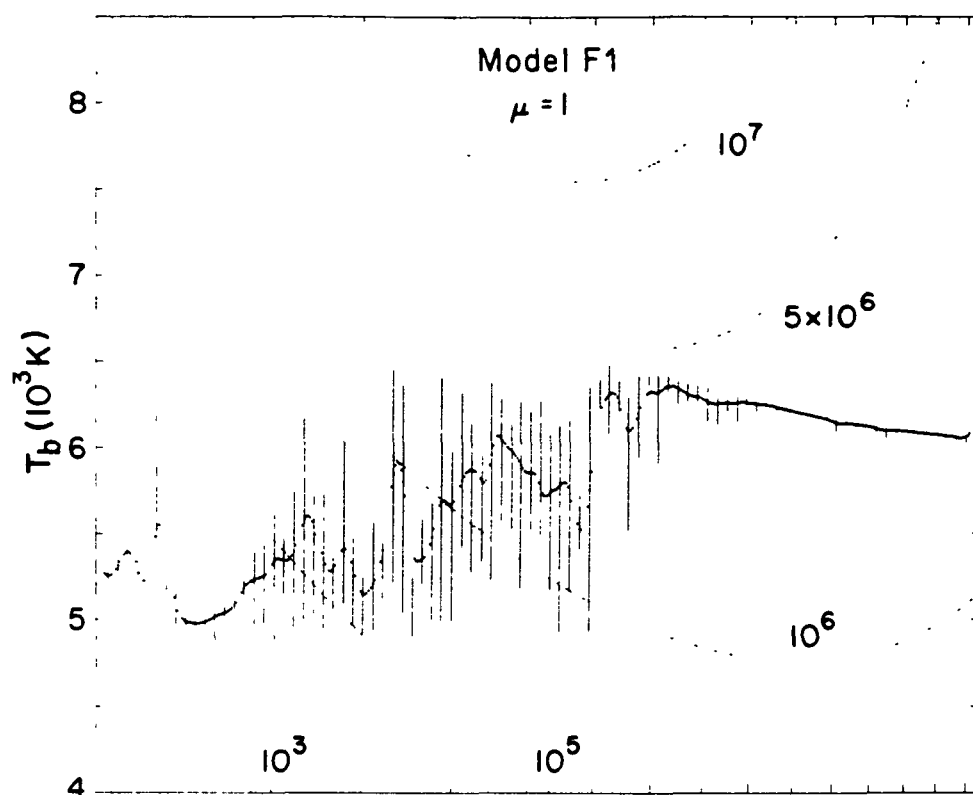
It should be noted that our selection of representative opacities at different frequencies may not account for the intensity enhancements due to individual strong lines. In particular, the results shown in Figure 5 may not fully account for the merging of highly Stark broadened Balmer lines close to the Balmer continuum limit, which would enhance the intensity distribution shortward of 4000Å as shown in calculations by Donati-Falchi *et al.* (1985).

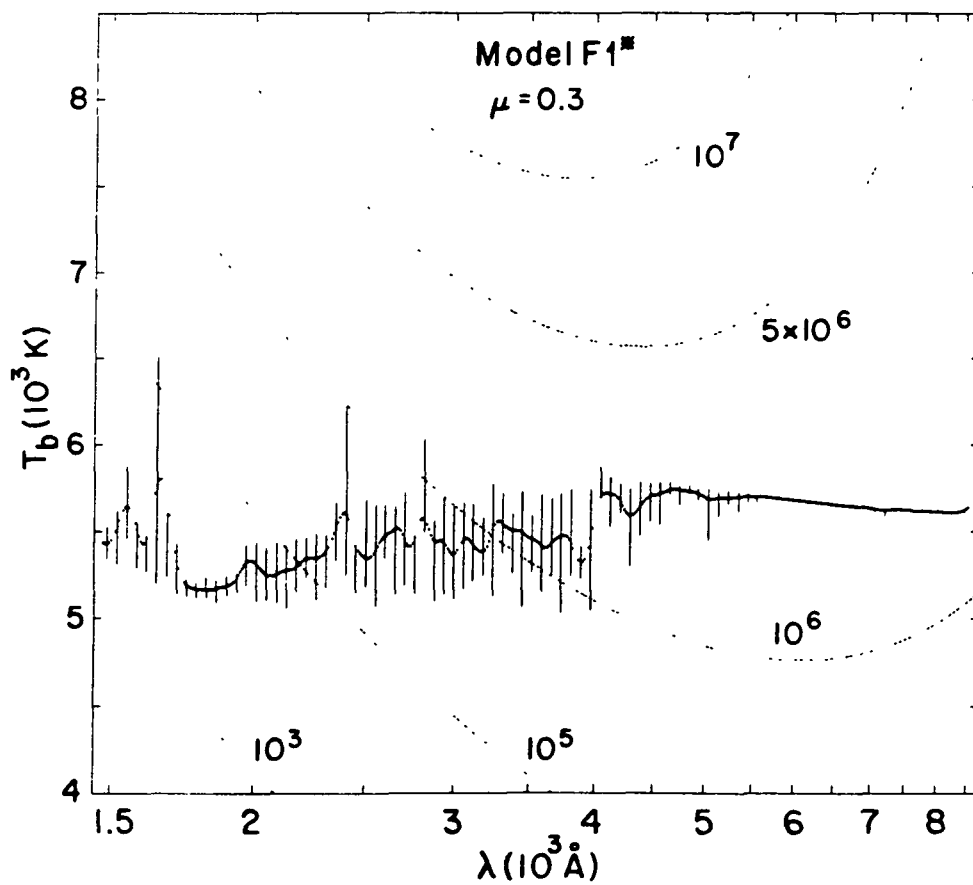
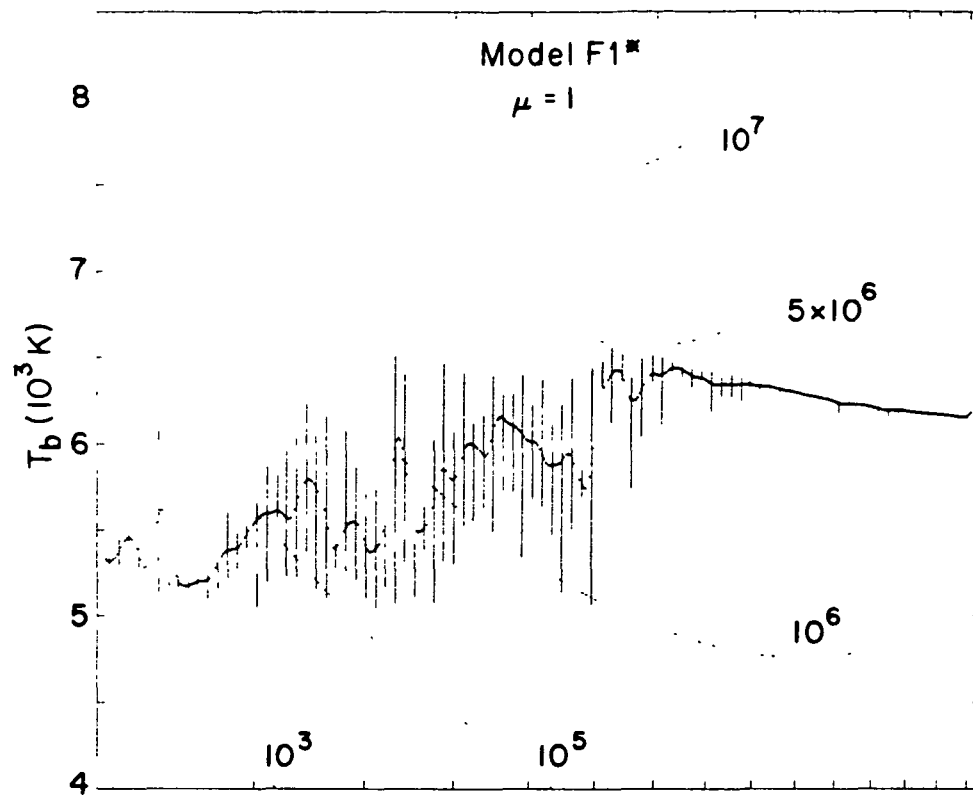
Fig. 5 (a-i, next 9 pages) - Calculated brightness-temperature and intensity distributions over the wavelength range 1500 - 8500Å for each model. The brightness-temperature graphs show the values of intensity ($10^3 - 10^7$) in units of $\text{ergs cm}^{-2} \text{s}^{-1} \text{sr}^{-1} \text{Å}^{-1}$. The vertical lines correspond to the maximum and minimum values computed from each set of five representative frequencies, as explained in the text. The dotted curve is a smoothed distribution. Figures 5(a), (b), and (c) show the results for models C, F1, and F1*; (d) compares the three distributions and (e) shows the intensity ratios F1/C and F1*/C; (f) and (g) show the results for models F2 and F3; (h) compares the distributions for models C, F1, F2, and F3; and (i) shows the intensity ratios F1/C, F2/C, and F3/C.

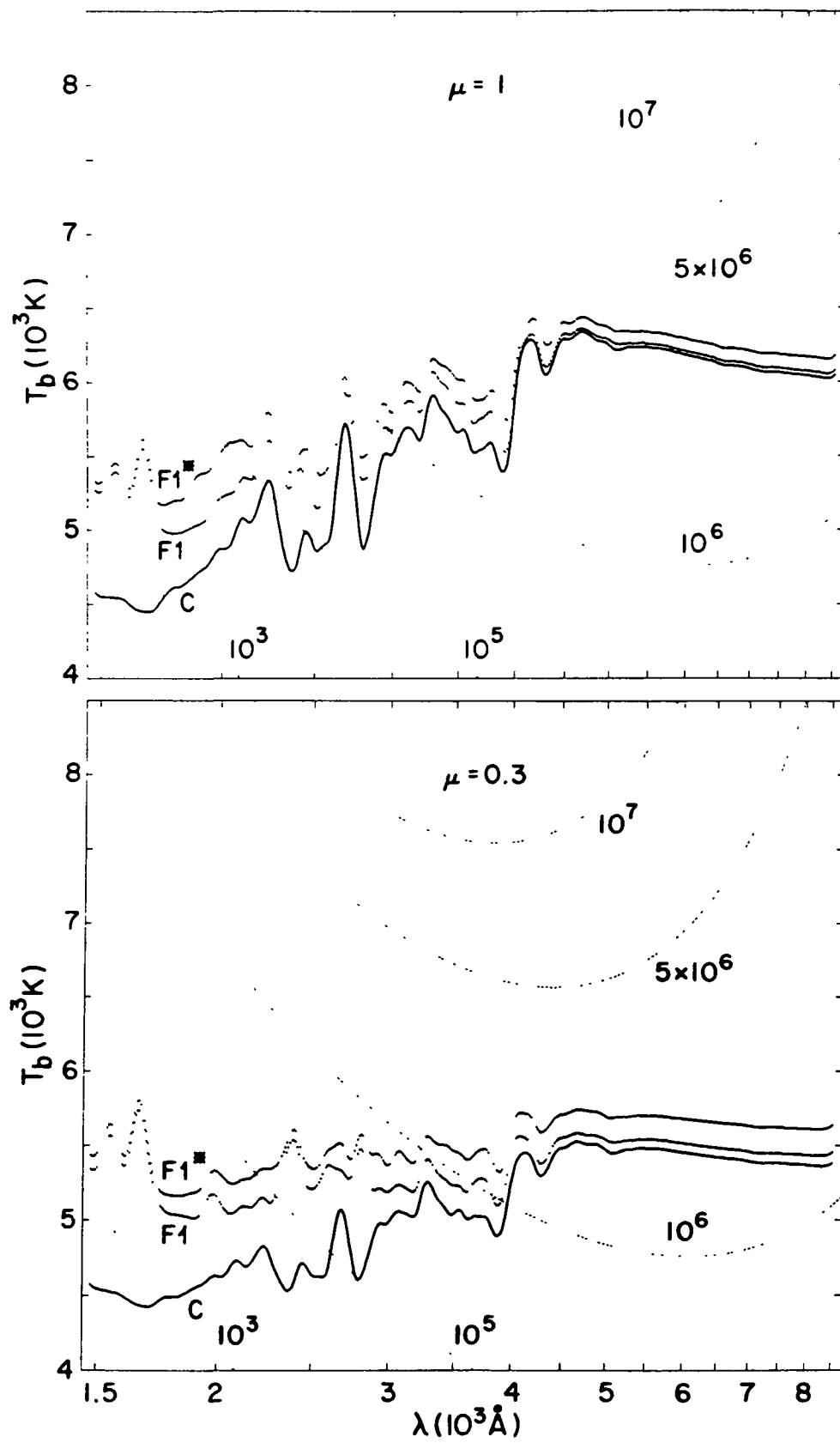
a

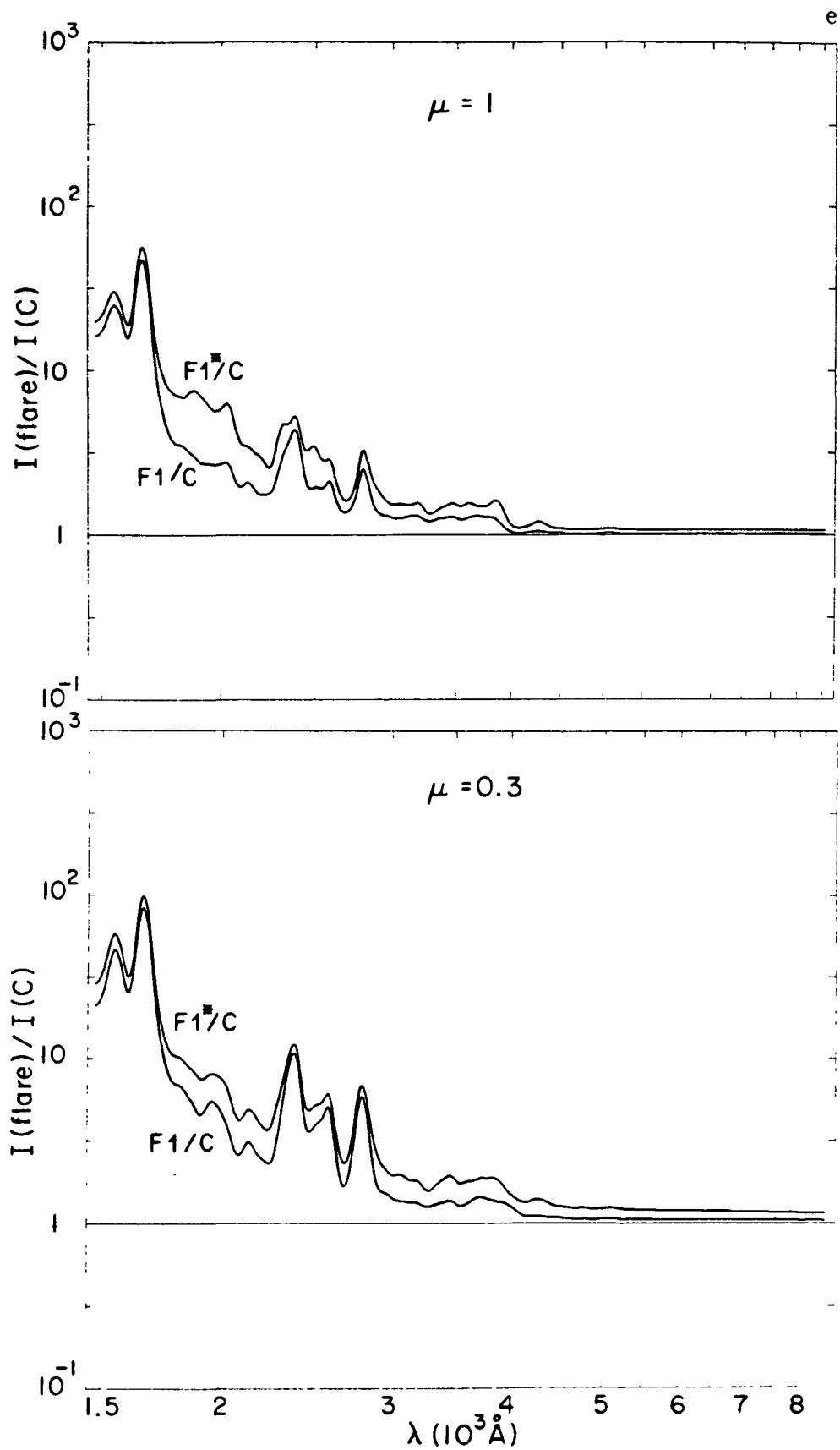


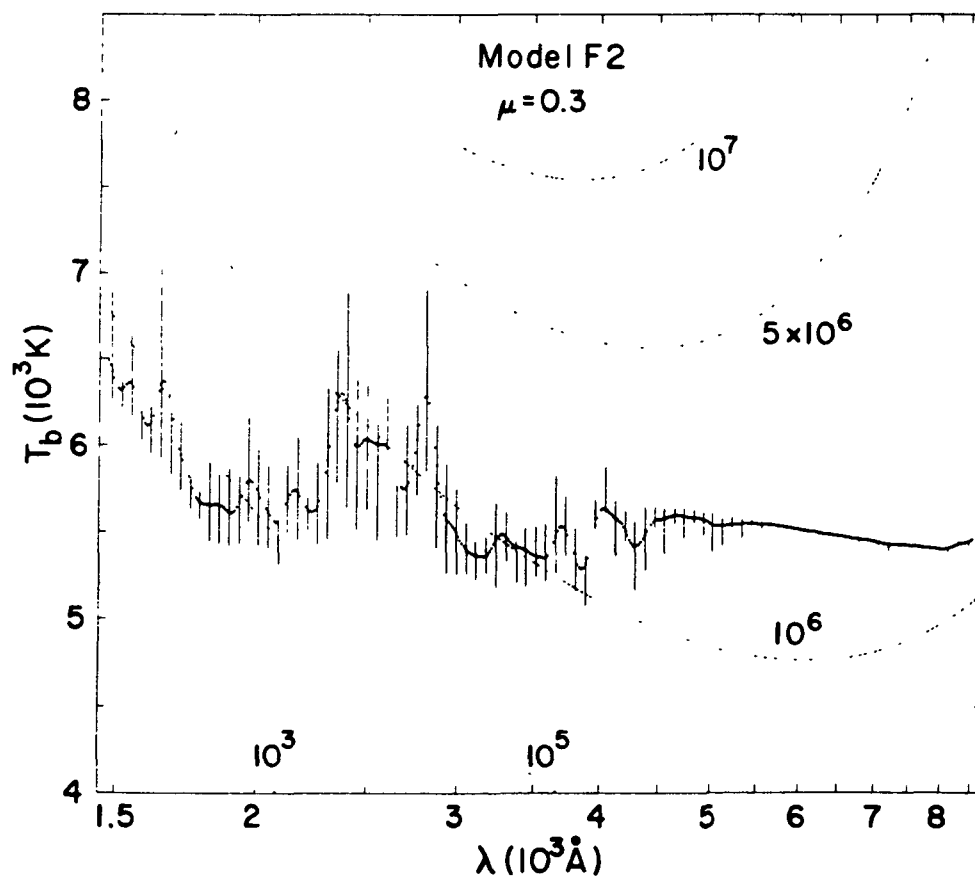
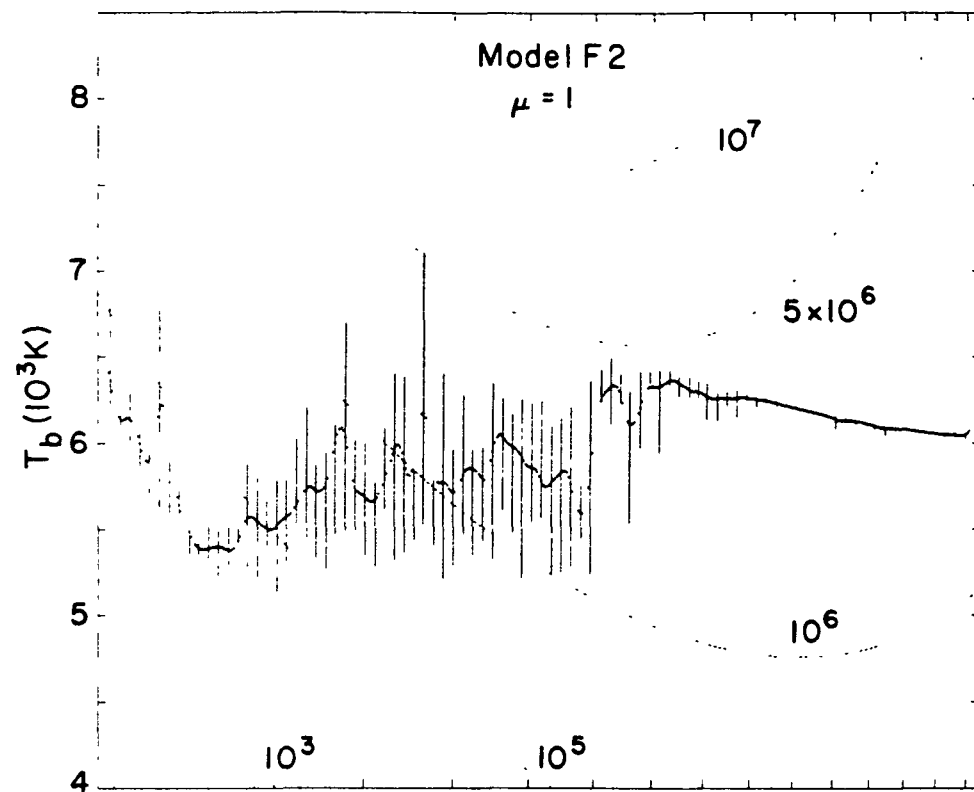
b





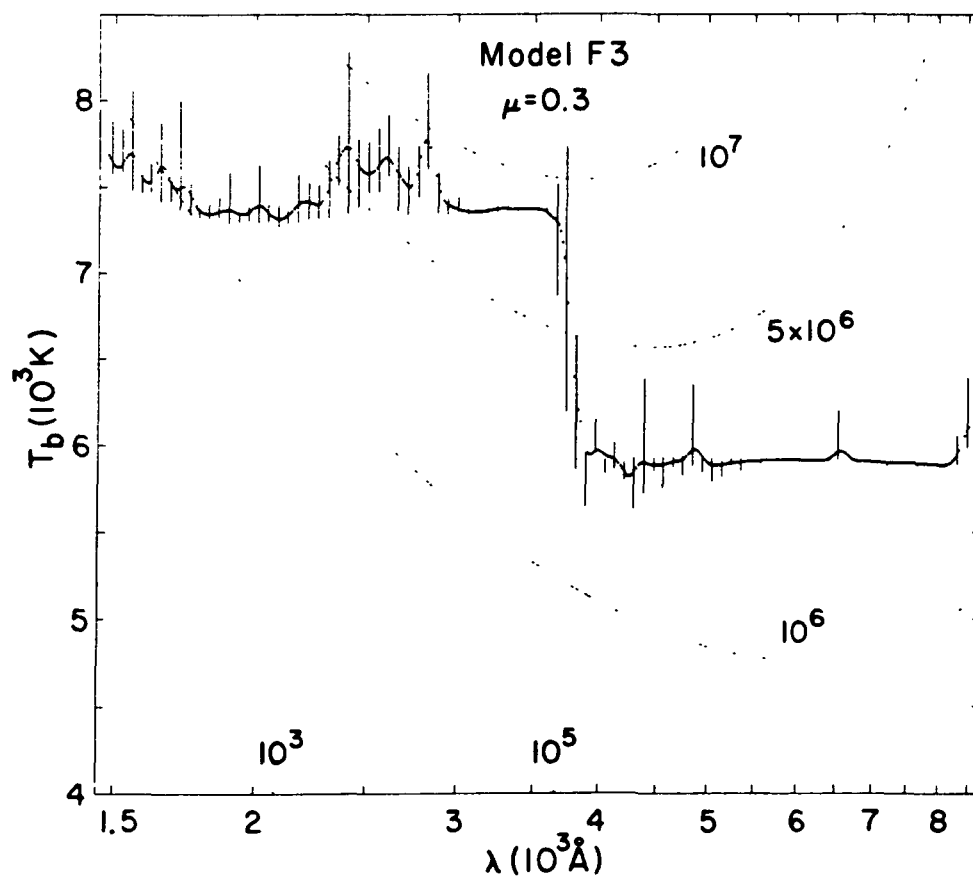
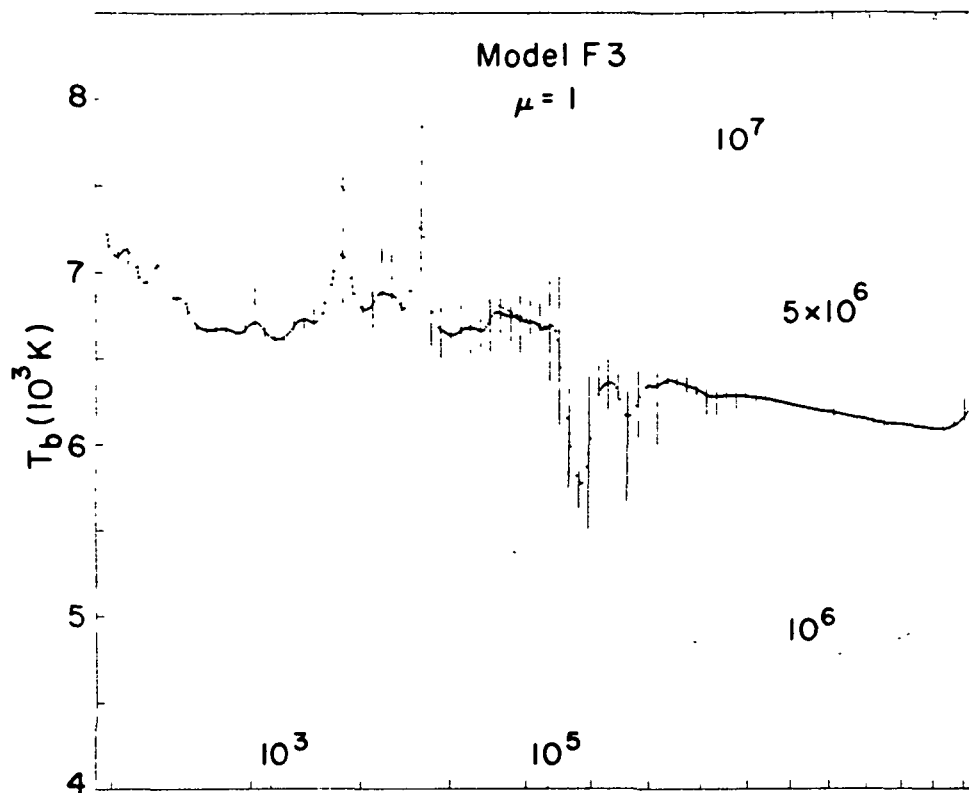


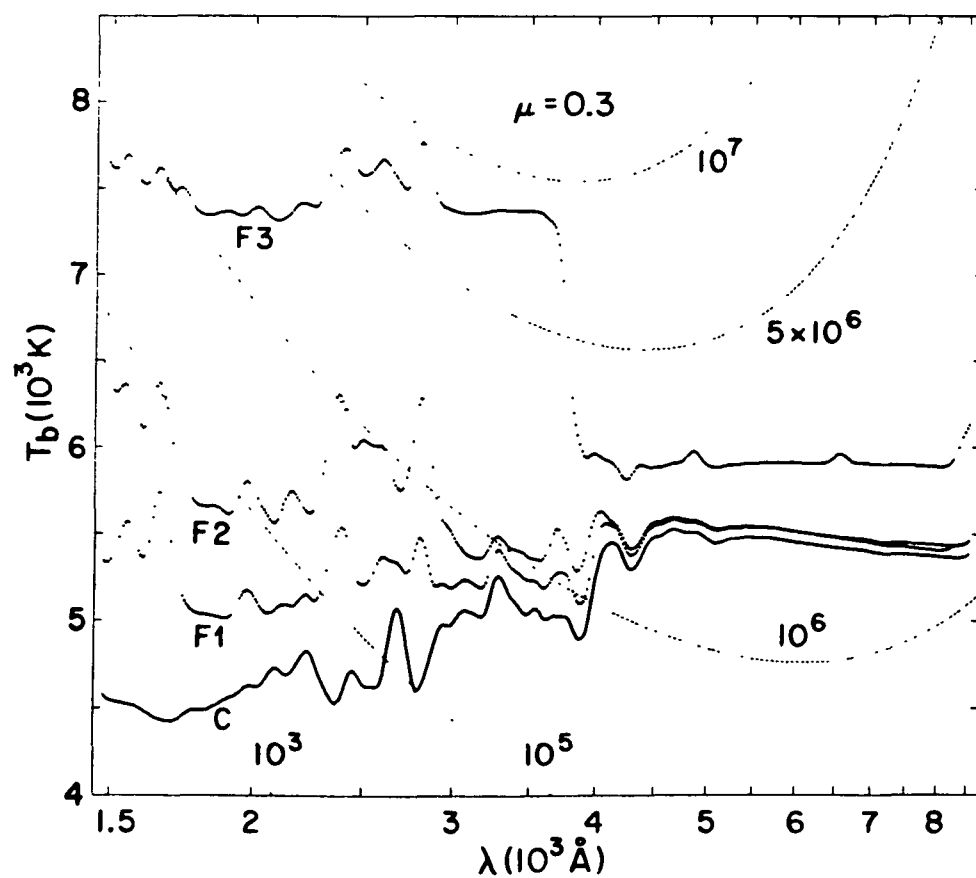
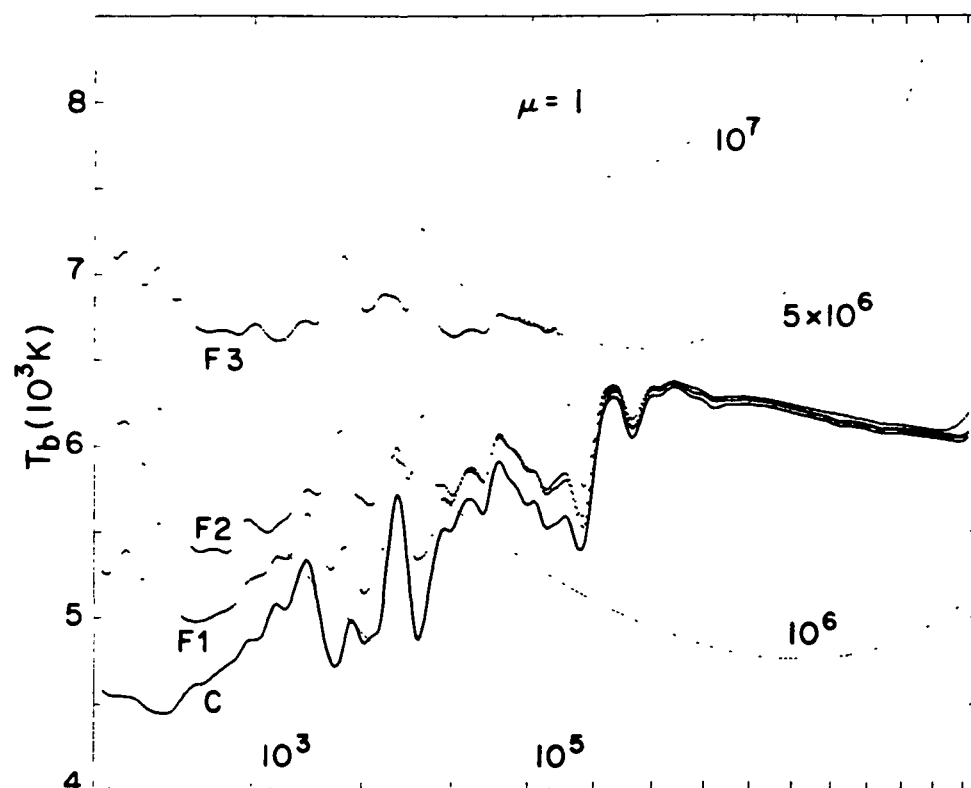


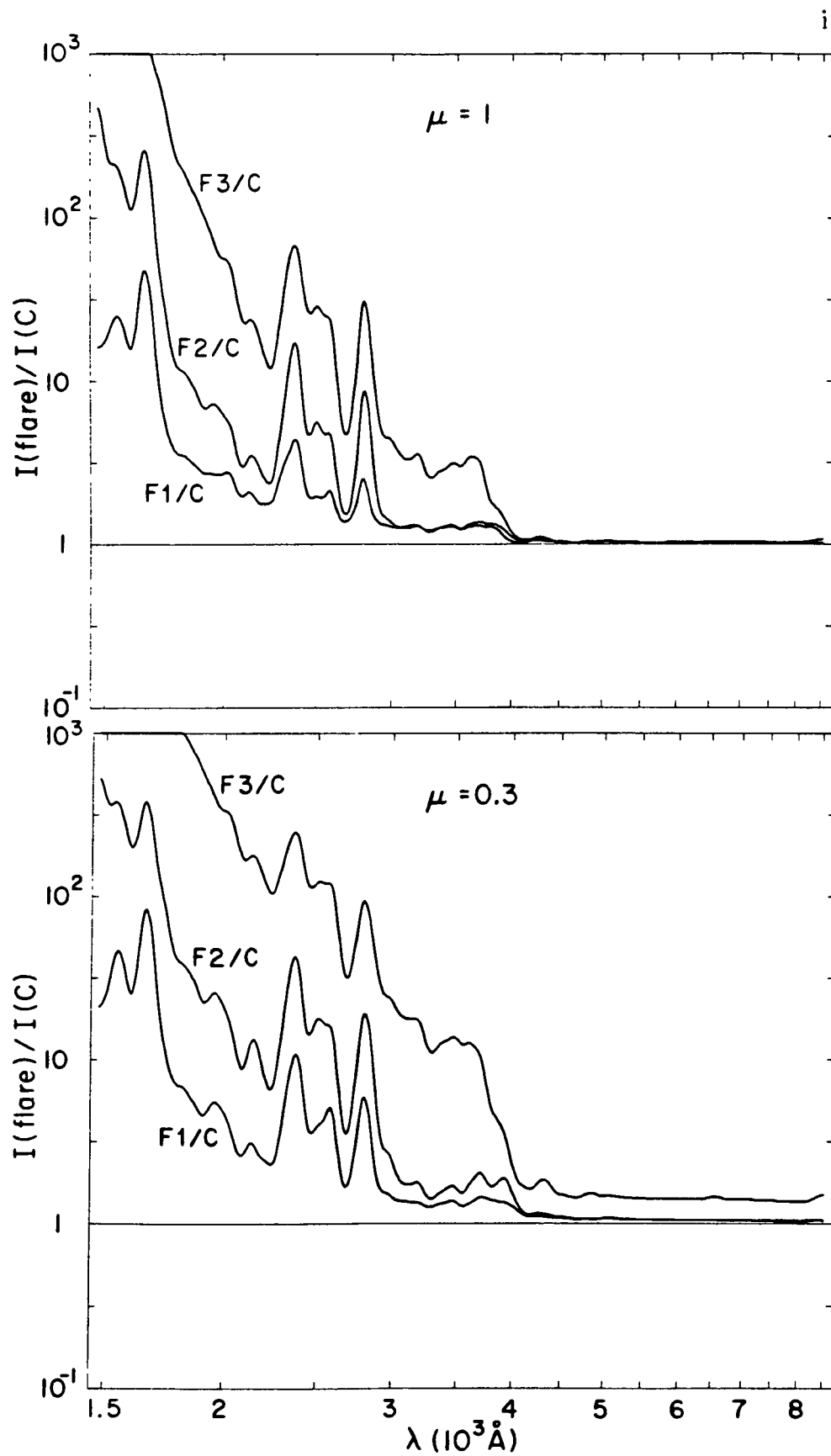


ORIGINAL PAGE IS
OF POOR QUALITY

8







The study of such effects requires detailed calculations of the spectrum. We include such calculations here only for the quiet Sun and model F3, and for three wavelength bands centered at 3610, 3862, and 4275Å. These are three of the bands used by Zirin and Neidig (1981) in their observations of white light flares. Figure 6 shows the computed spectra for the disk center and for $\mu = 0.3$ near the limb.

These results, for model F3 vs. the average quiet Sun, seem generally consistent with the observations by Zirin and Neidig (1981) who reported a Balmer continuum increase in the intensity by a factor of 2.5, and with reports that WLF enhancements are larger at the limb than at disk center. The calculations also show a moderate enhancement of the Paschen continuum (see Neidig and Wiborg 1984).

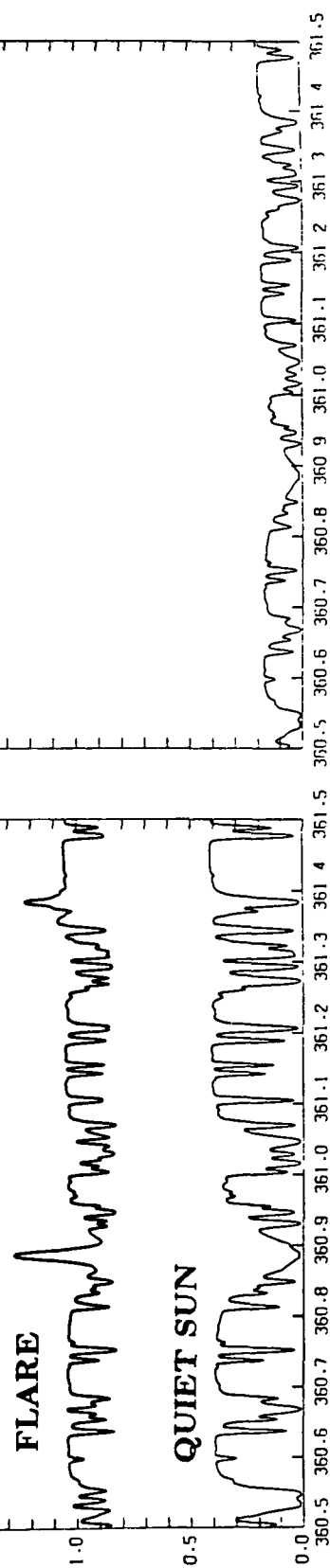
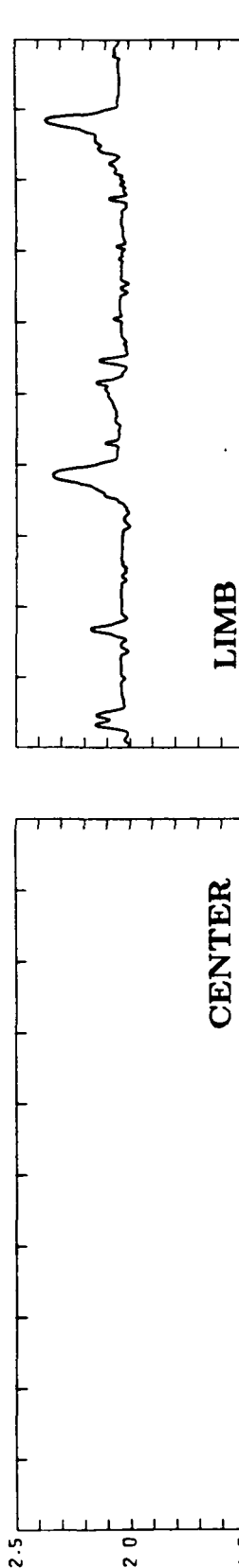
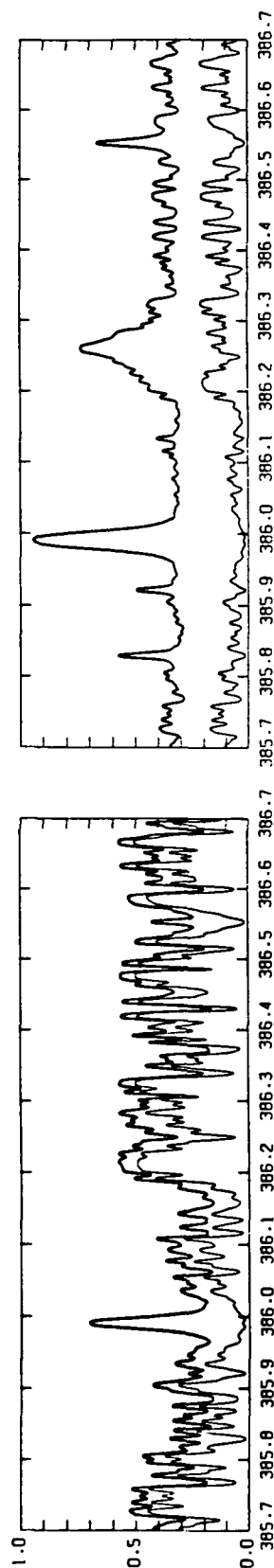
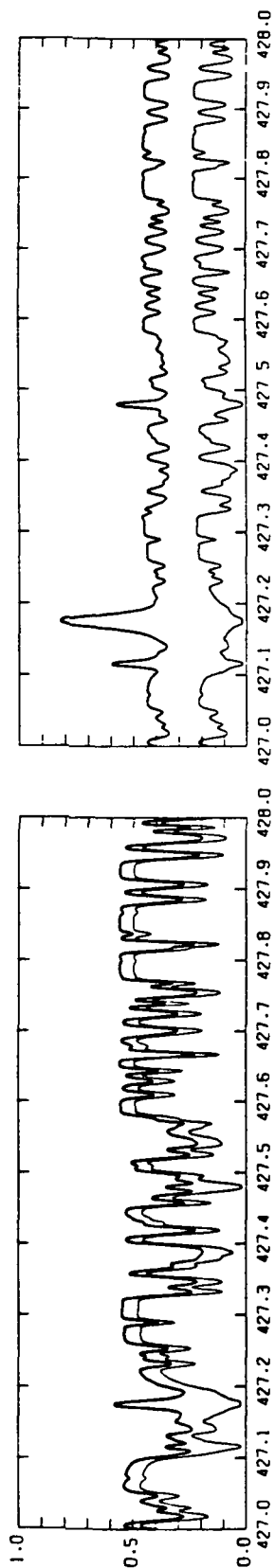
The following table shows the sources of emission in the upper chromosphere (temperatures between 9000 and 10,000 K) responsible for the enhancement in model F3.

TABLE 1

Percent Contributions to the Emission from the
Upper Chromosphere (9000K < T < 10,000K) of Model F3

	$\lambda 3610$		$\lambda 3862$	$\lambda 4275$	$\lambda 8200$		$\lambda 8300$
H _{bf}	99		77	86	88		38
H _{ff}			8	9	11		20
H ⁻	1		5	4	1		2
lines			10	1			40
		Balmer limit				Paschen limit	

Fig. 6 (next page) - Sample theoretical spectra in 1nm wavelength bands centered at 361, 386.2, and 427.5nm. The intensity in units of $10^8 \text{ ergs cm}^{-2} \text{ s}^{-1} \text{ sr}^{-1} \text{ nm}^{-1}$ is shown as a function of wavelength in nm, at the disk center and at $\mu = 0.3$ near the limb, for the quiet Sun and for flare model F3. These spectra were computed using the synthesis programs described by Kurucz and Avrett (1981). The line data were selected from the compilation of 1.7×10^7 atomic and molecular lines described by Kurucz (1985).



It should be noted that all of our flare models predict some enhancement of the Balmer continuum. However, some WLF events show essentially no such enhancement (see, for example, Boyer *et al.* 1985). Ordinary flares that are not seen in white light also do not have Balmer continuum enhancements. This is a modeling problem that was recognized in the earlier, simpler calculations of Svestka (1965) and deFeiter (1966). We show later that the conditions giving rise to an enhancement of the Balmer continuum can lead to radiative heating deep in the flare atmosphere, but our models do not suggest how the deep layers might be heated without the occurrence of a Balmer continuum enhancement.

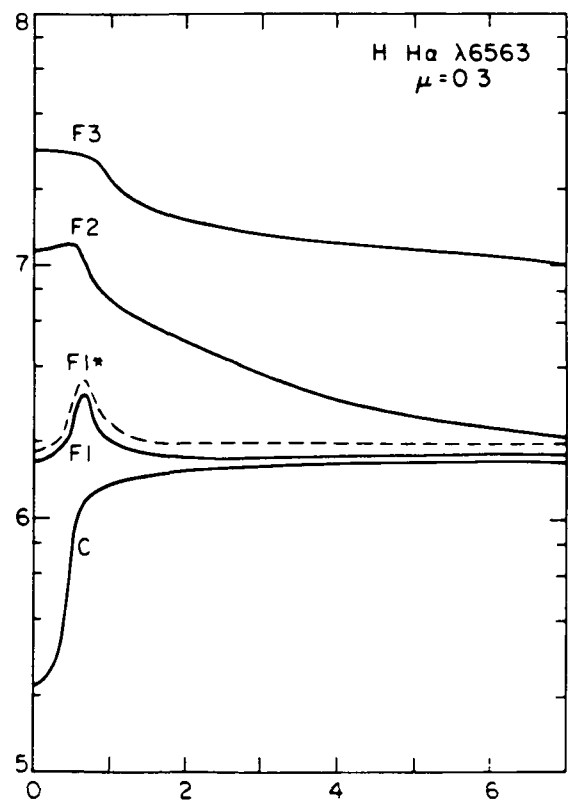
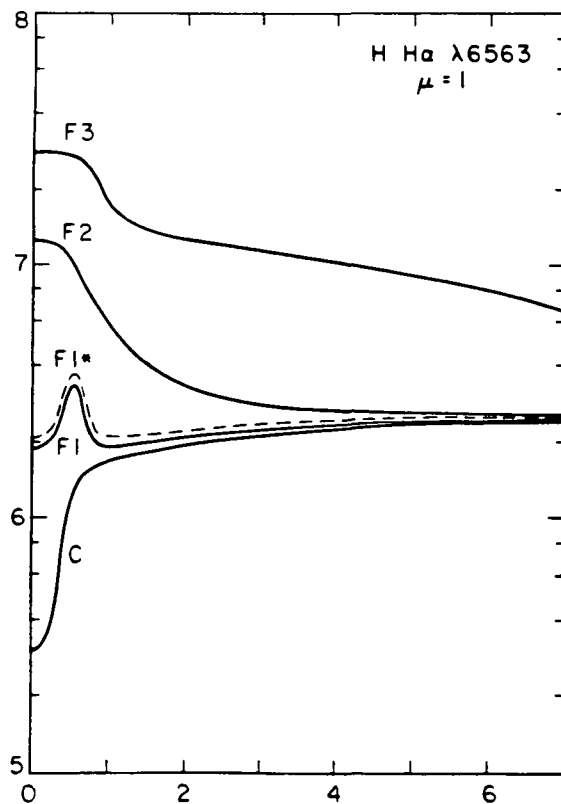
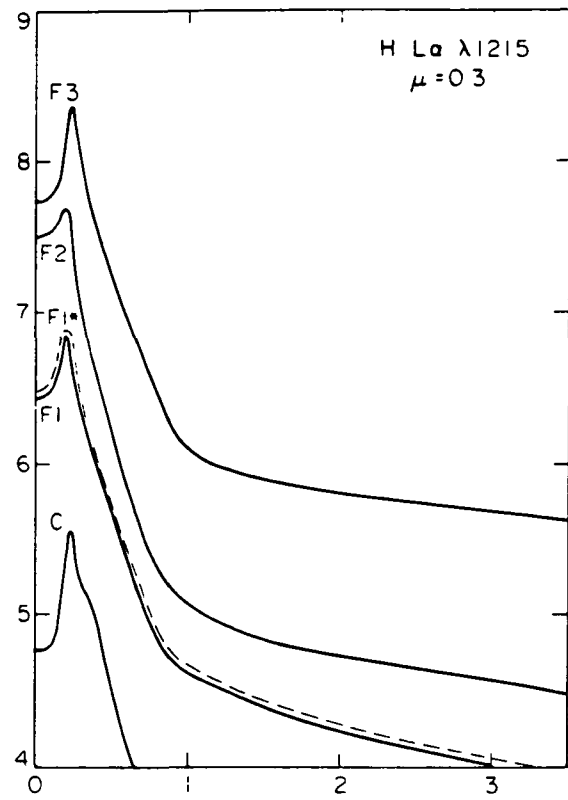
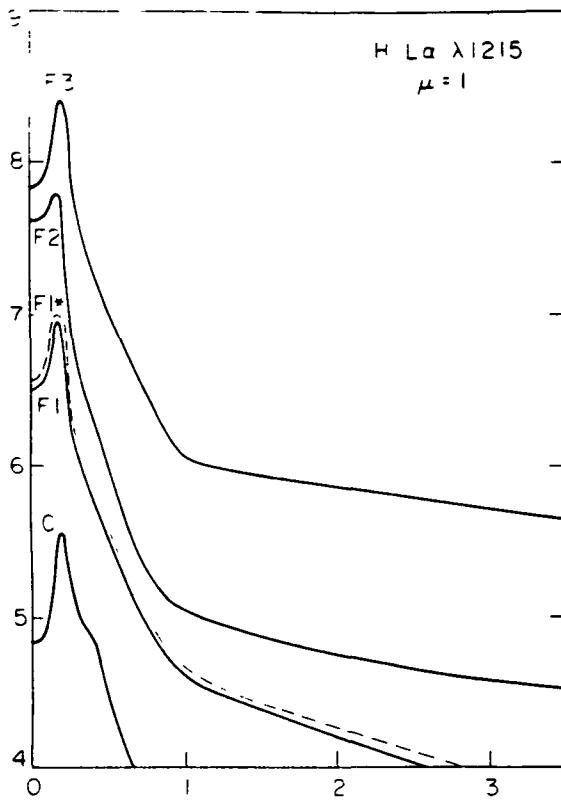
We now turn to the calculation of individual line profiles.

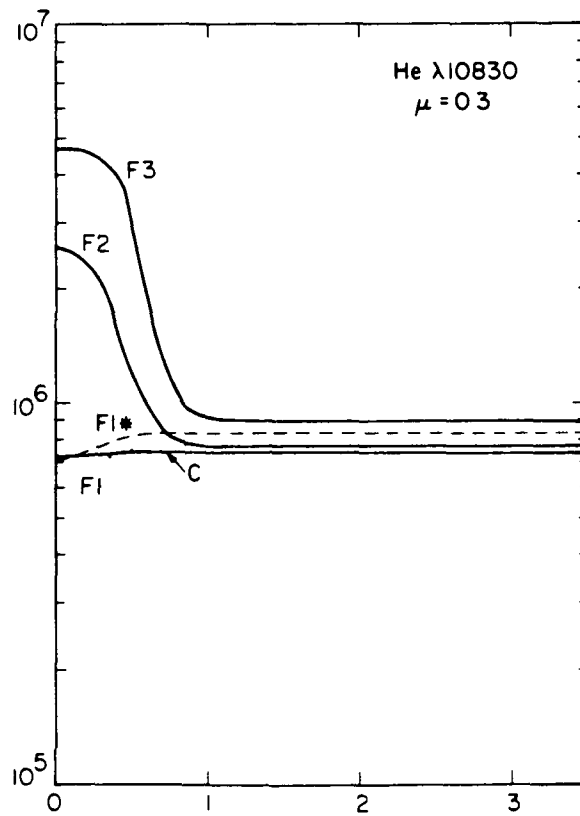
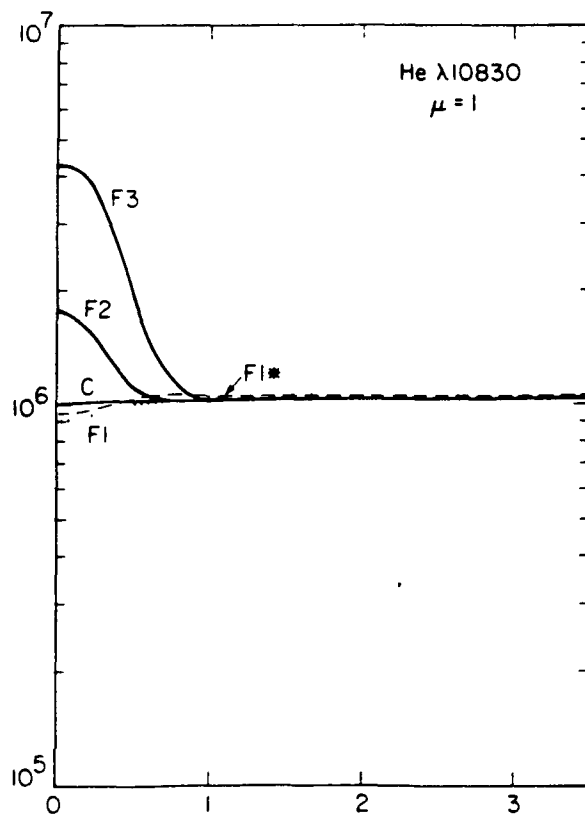
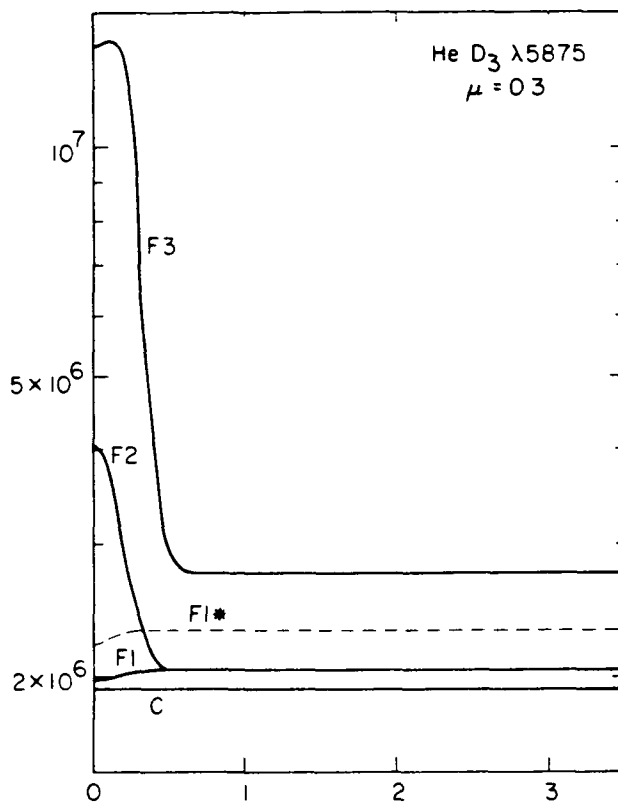
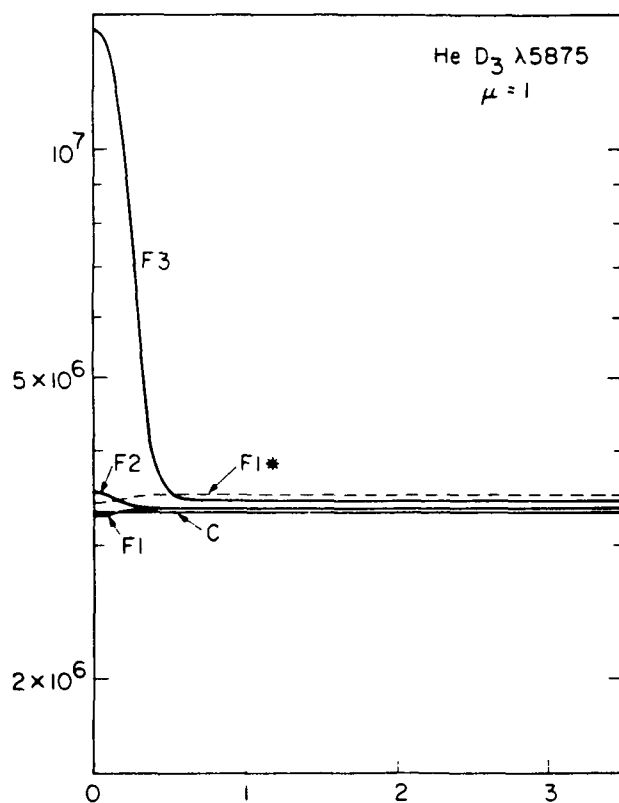
For each of the models, we have solved the statistical equilibrium and radiative transfer equations for a group of atoms and ions including H, He I-II, Na, Mg I-II, Ca II, Si I-II, Fe, C I-IV, and O I-II. Figures 7a through 7m show the profiles of 26 selected lines from the atoms and ions listed above. Observations of some of these lines (integrated intensities and line profiles in some cases), usually in weak flares, are given by Canfield *et al.* (1980a,b; H α , L α , He II, C I-II, O I, Si II.

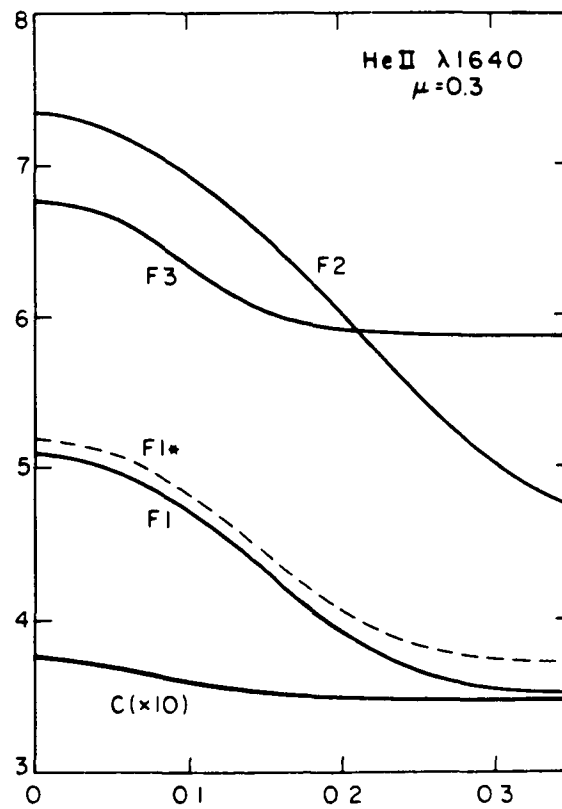
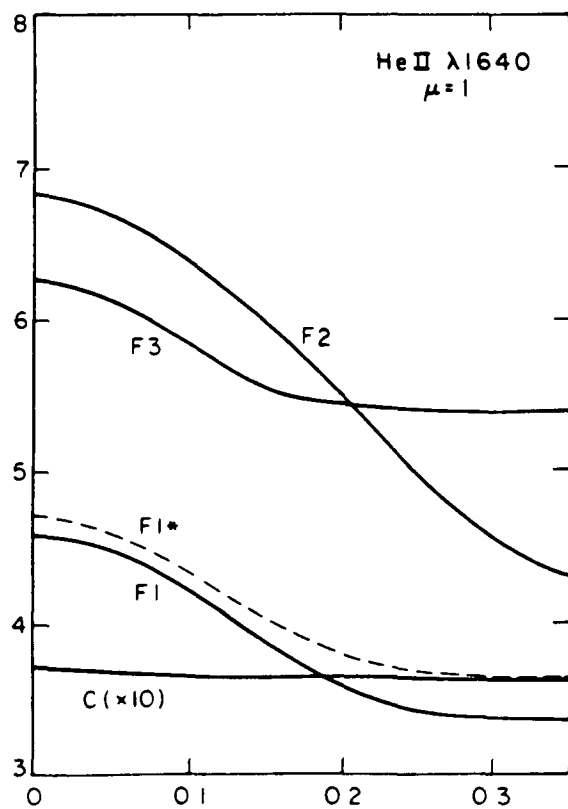
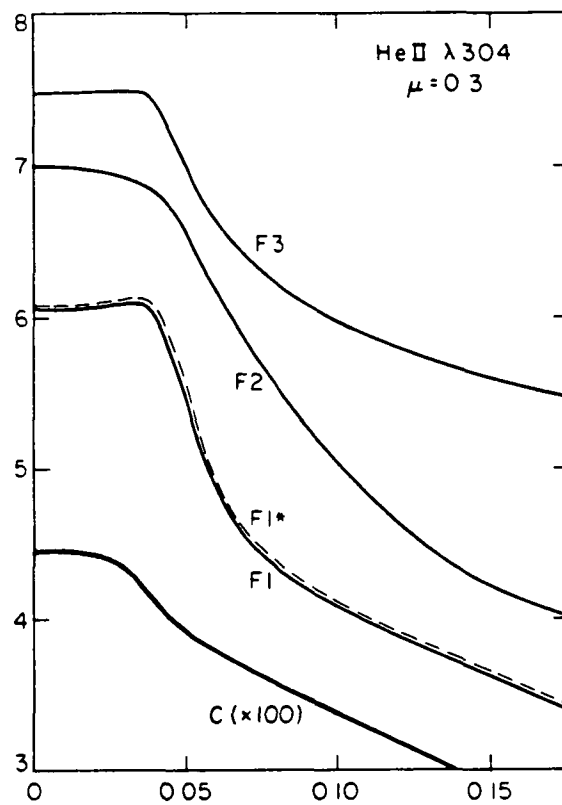
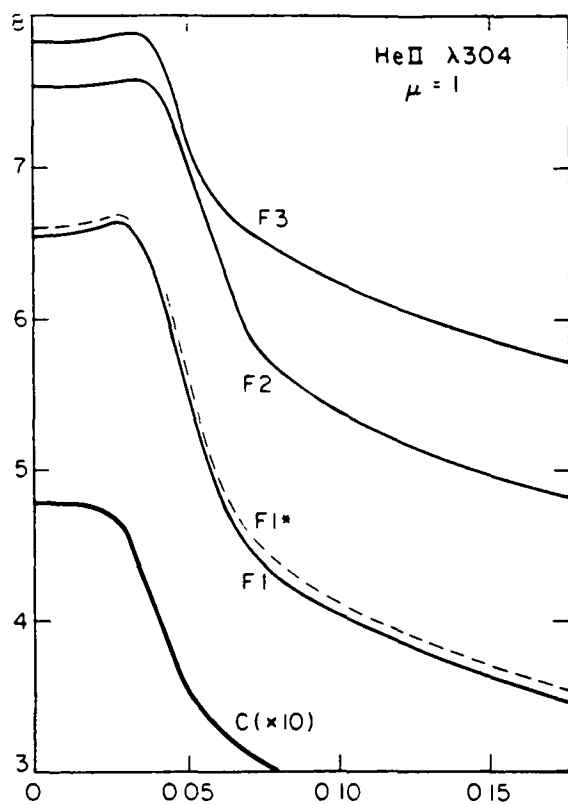
Fig. 7 (next 13 pages) - Theoretical center and limb profiles for 26 selected lines from the atoms and ions, and at the central wavelengths (in Å), listed below. Intensities in $\text{ergs cm}^{-2} \text{s}^{-1} \text{sr}^{-1} \text{Å}$ are shown as functions of $\Delta\lambda$ in Å.

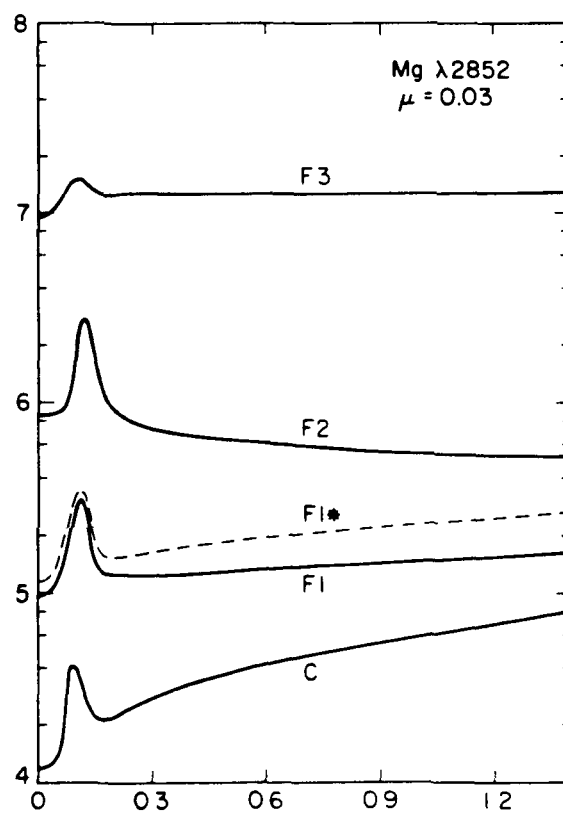
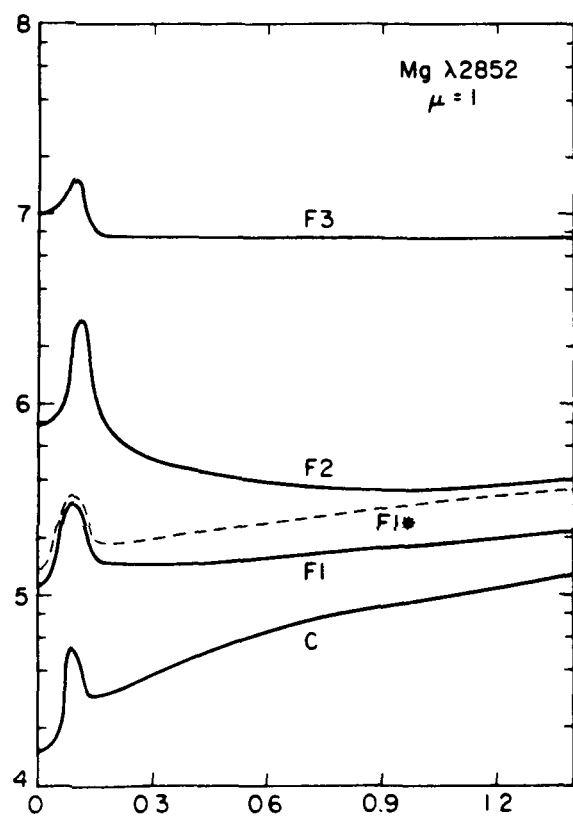
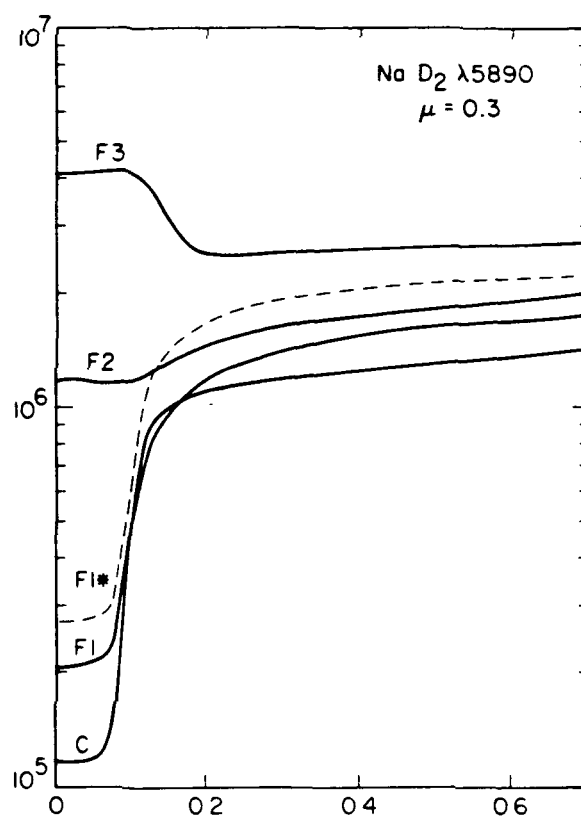
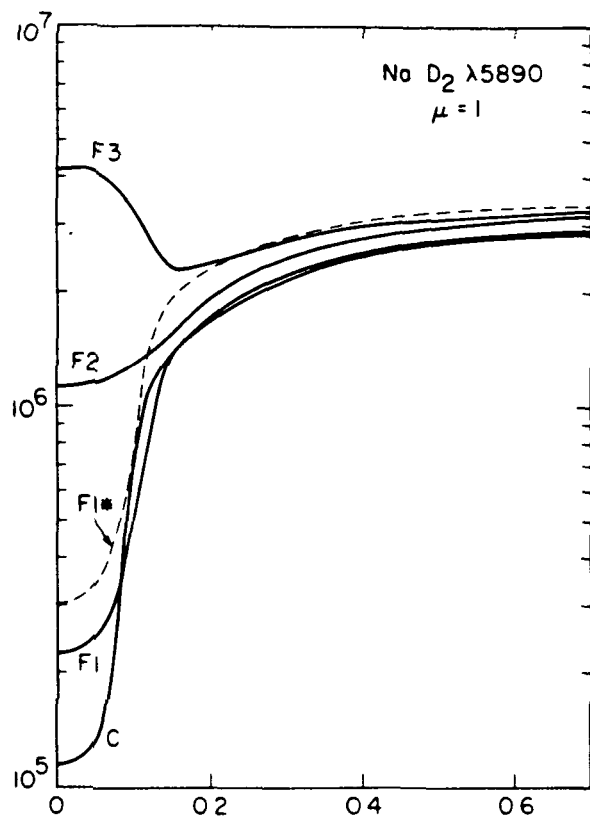
H	1215	L α	Si II	1533
H	6563	H α	Si II	1816
He	5875	D3	Fe	3719
He	10830		Fe	5012
He II	304		Fe	8688
He II	1640		C	1561
Na	5890	D ₂	C II	1335
Mg	2852		C III	977
Mg	5180	b	C III	1175
Mg II	2795	k	C IV	1547
Ca II	3933	K	O	1302
Ca II	8498		O	7771
Si	2516		O II	834

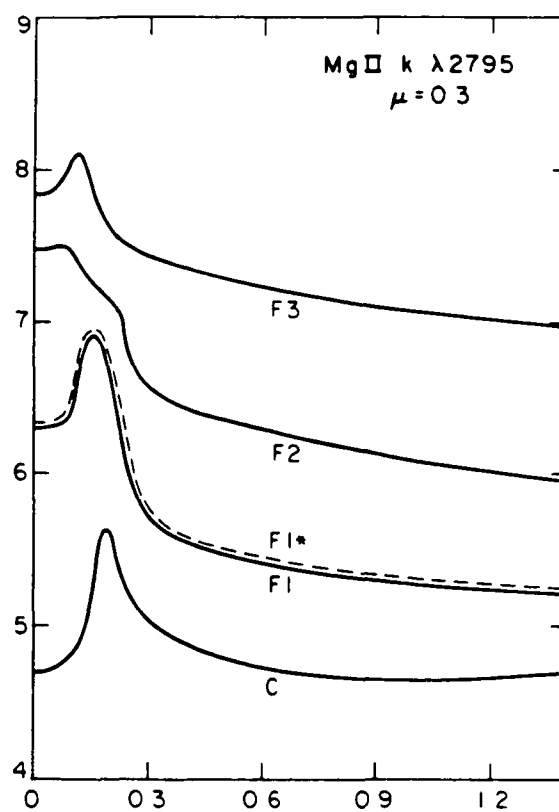
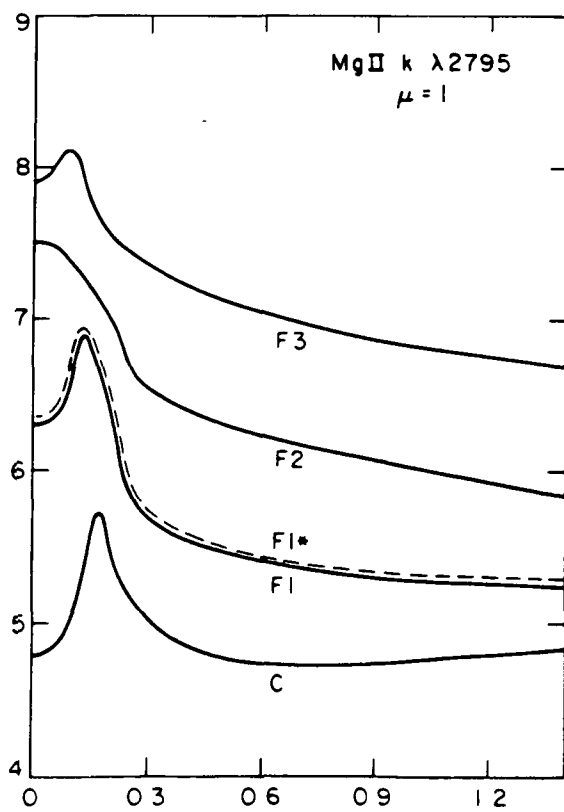
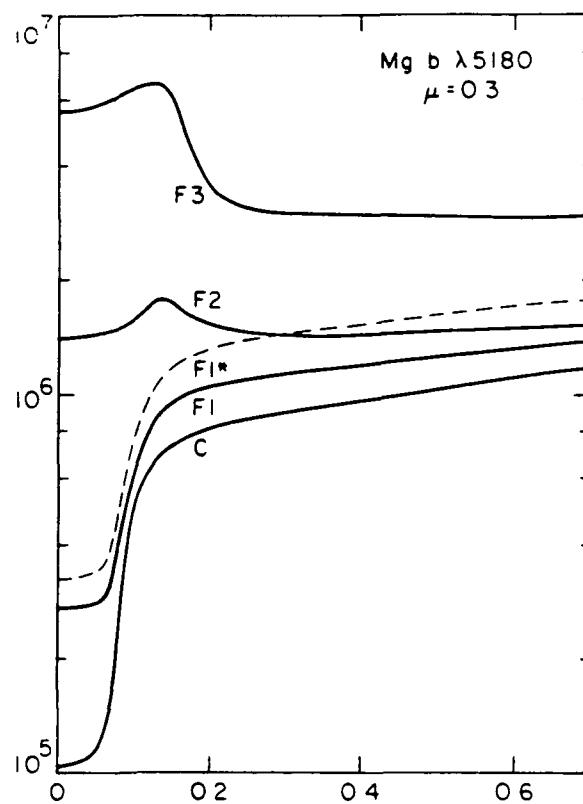
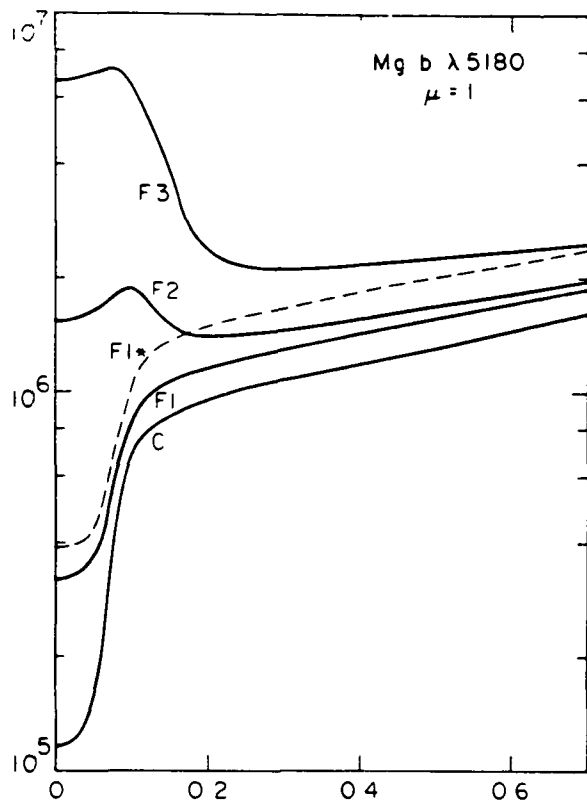
ORIGINAL PAGE IS
OF POOR QUALITY

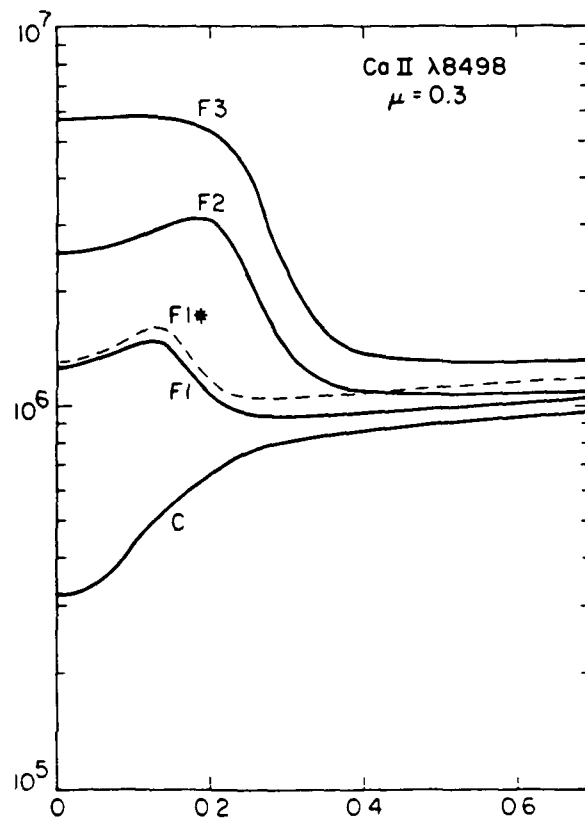
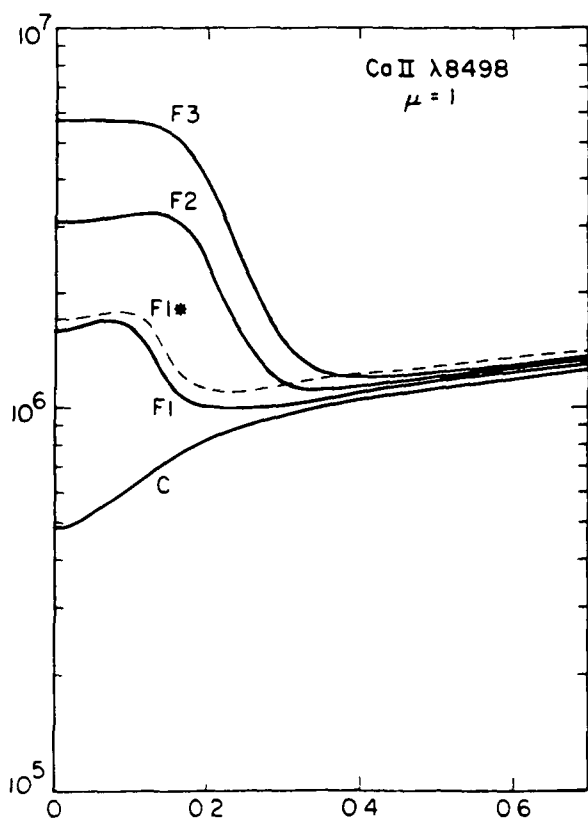
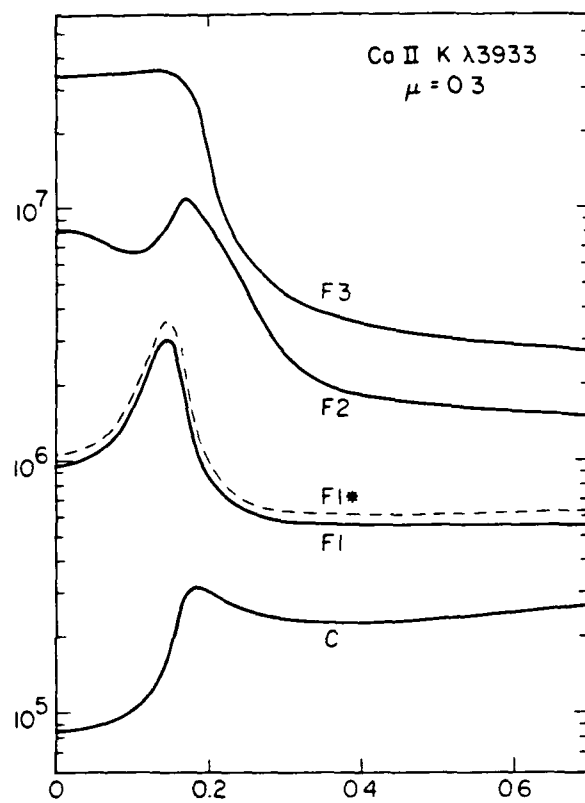
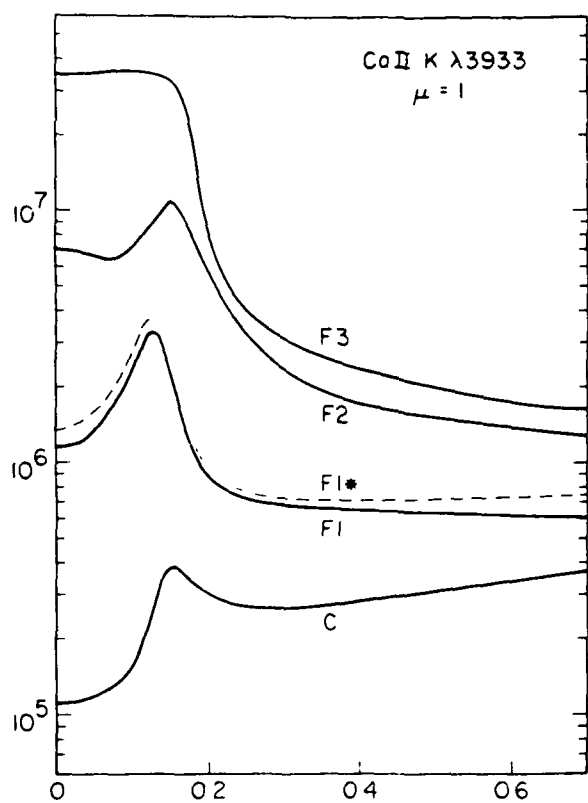


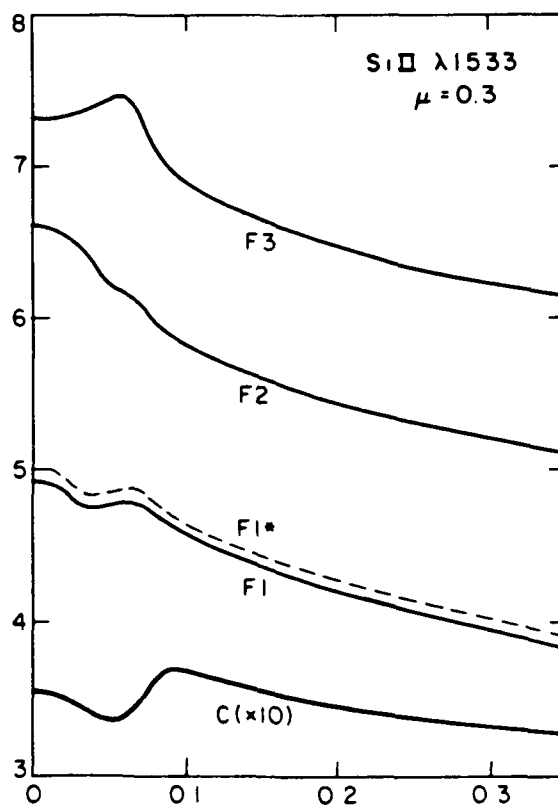
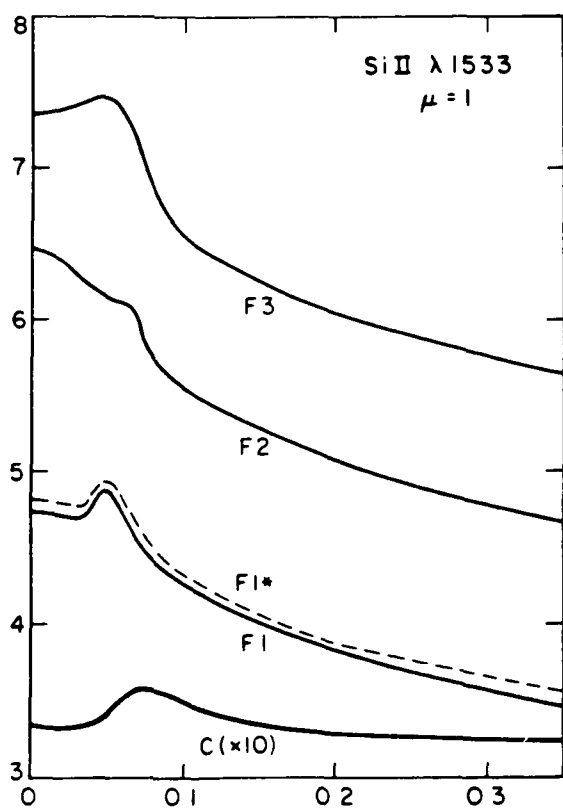
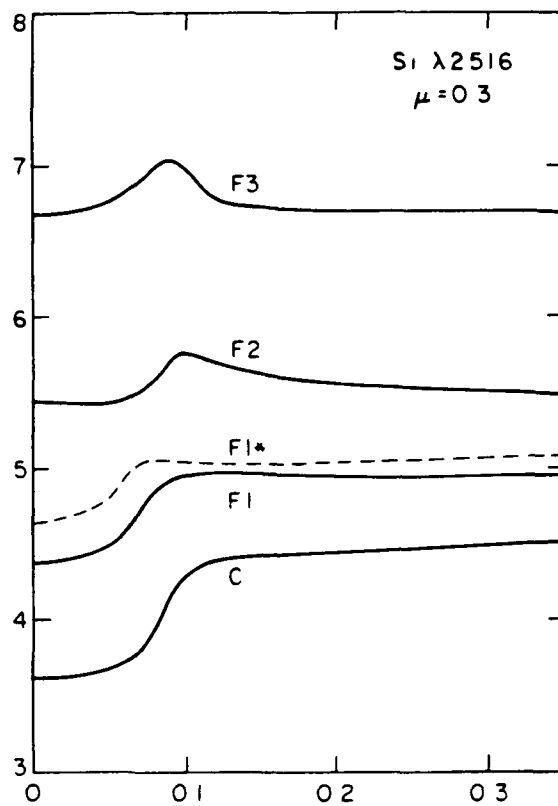
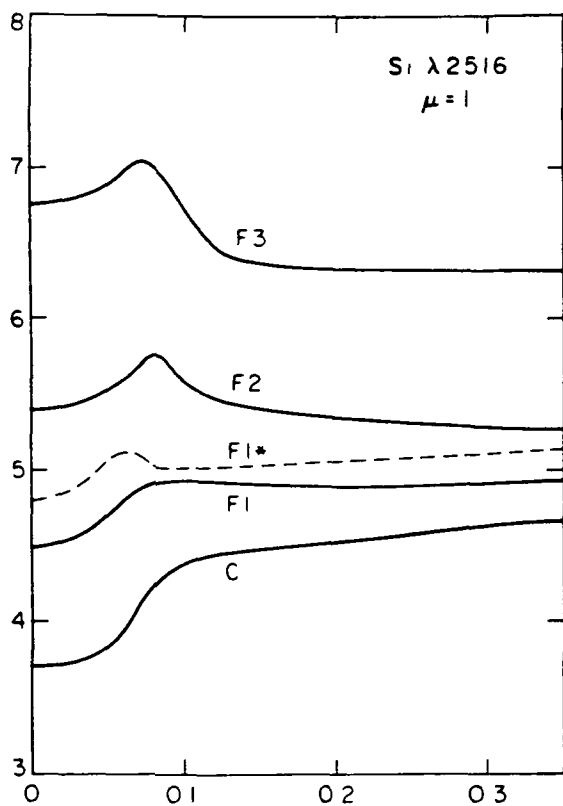


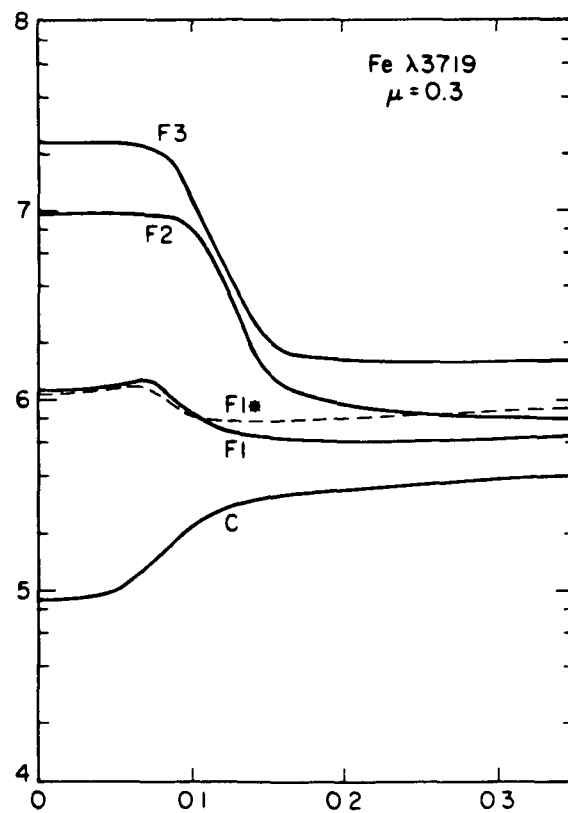
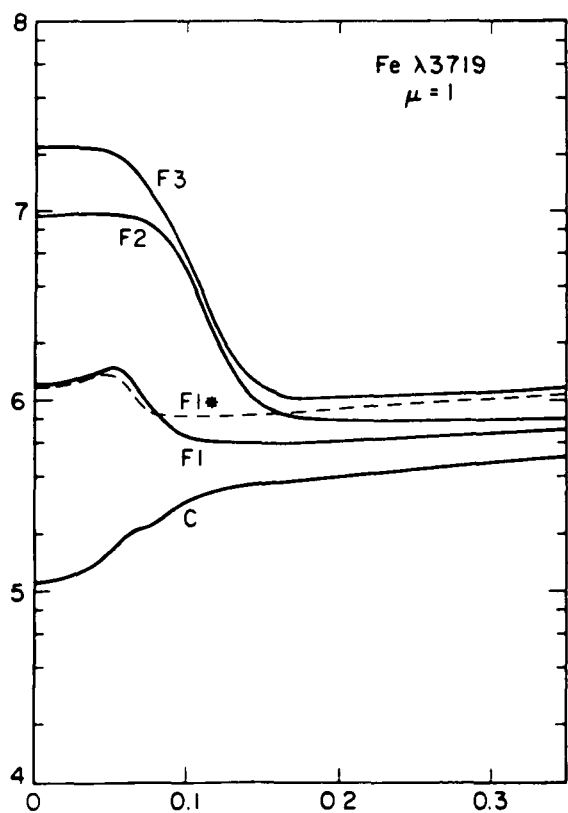
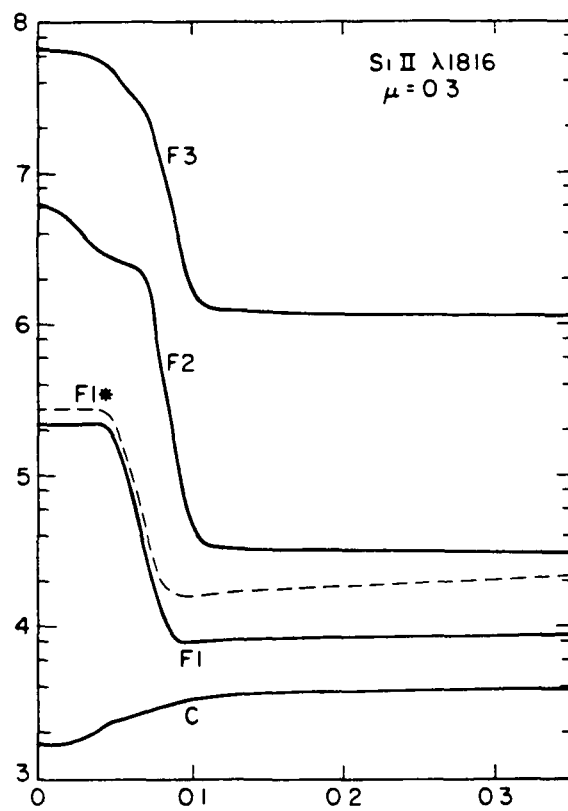
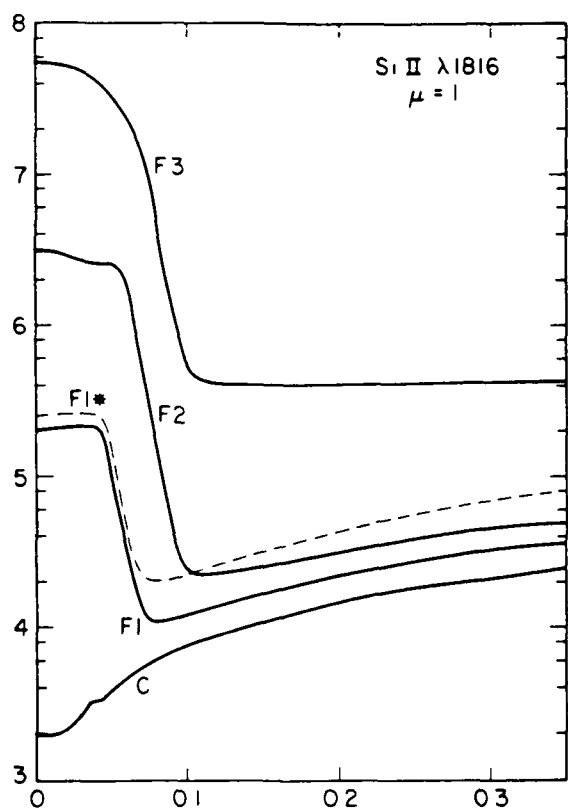


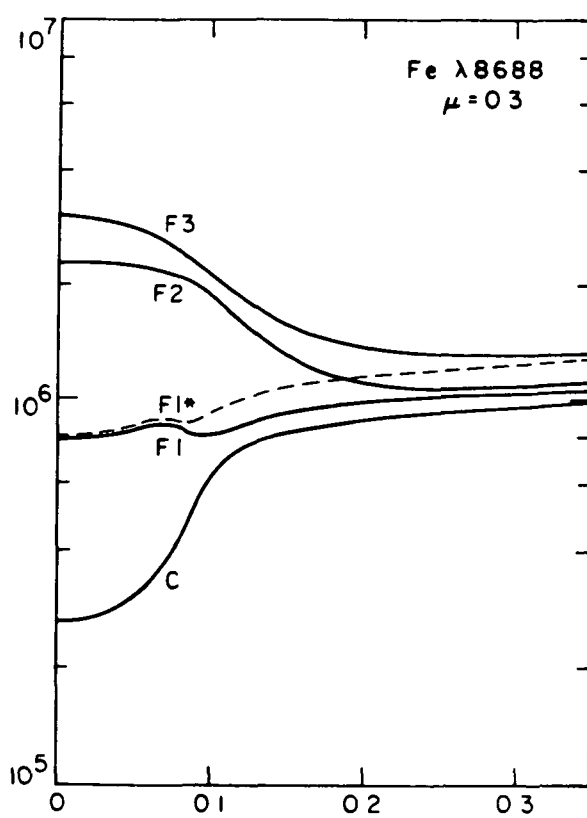
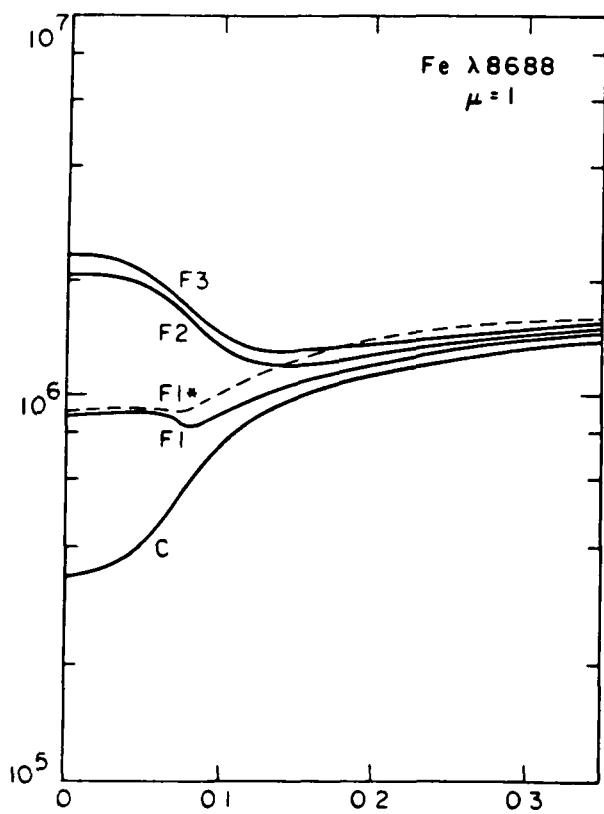
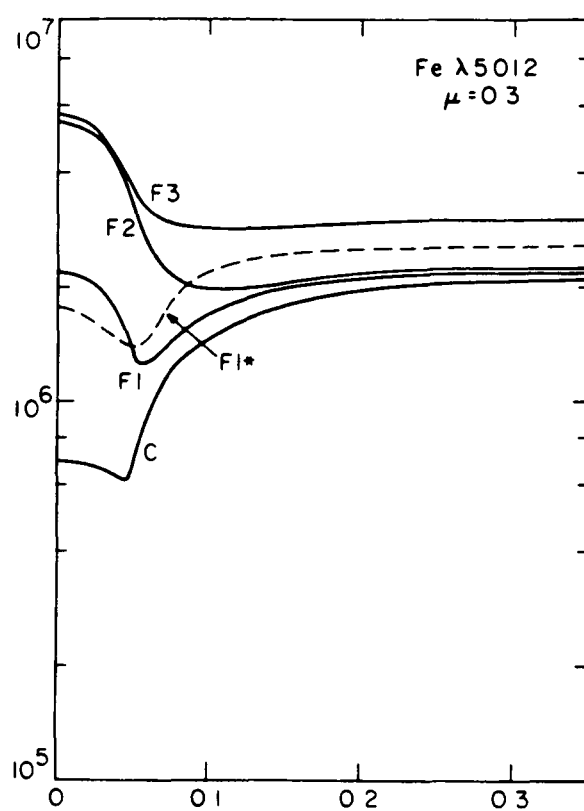
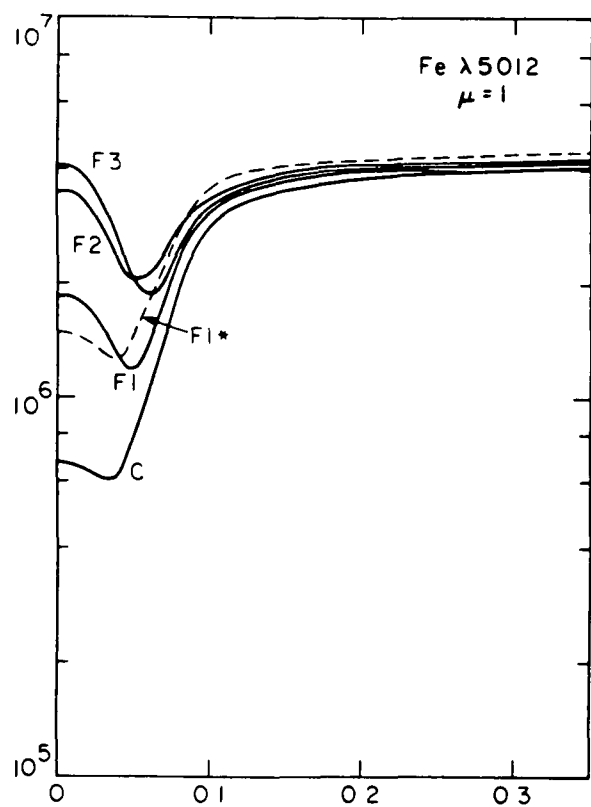


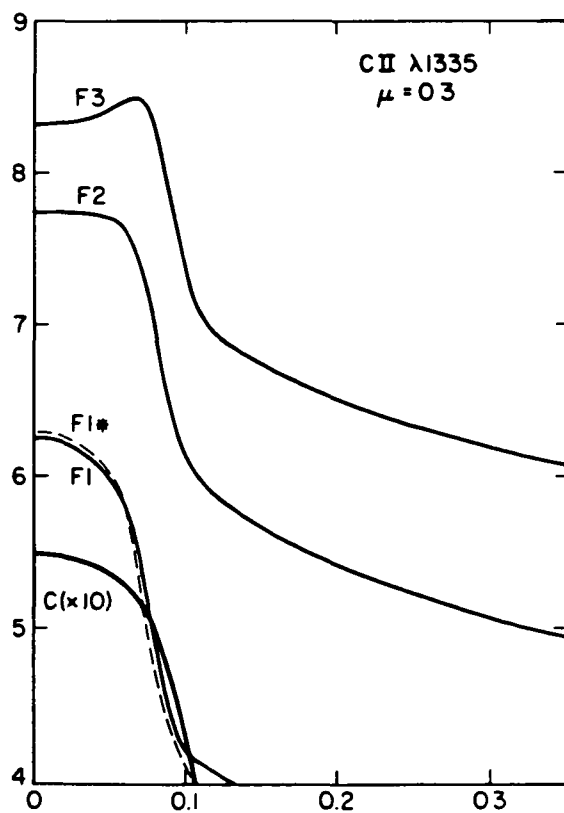
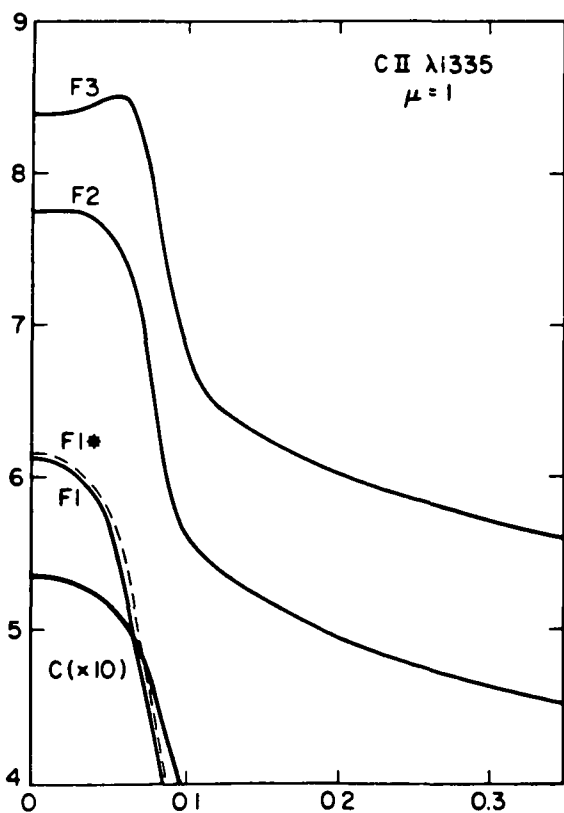
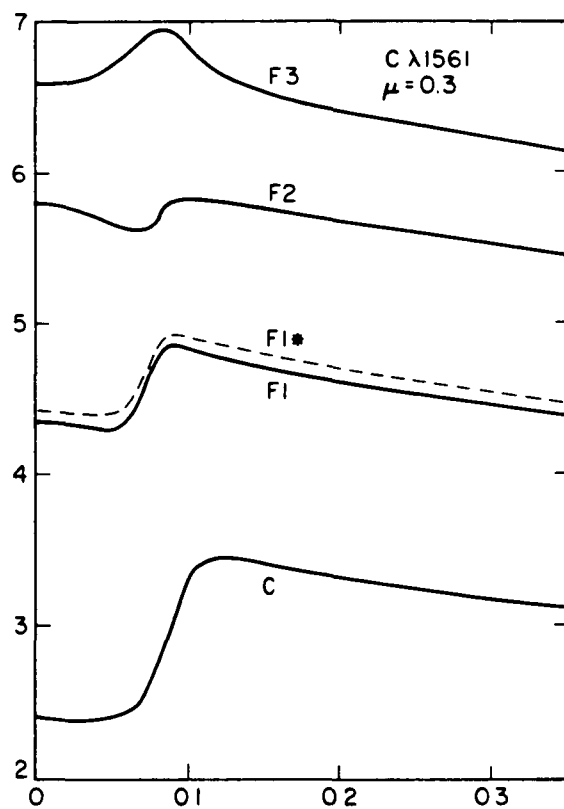
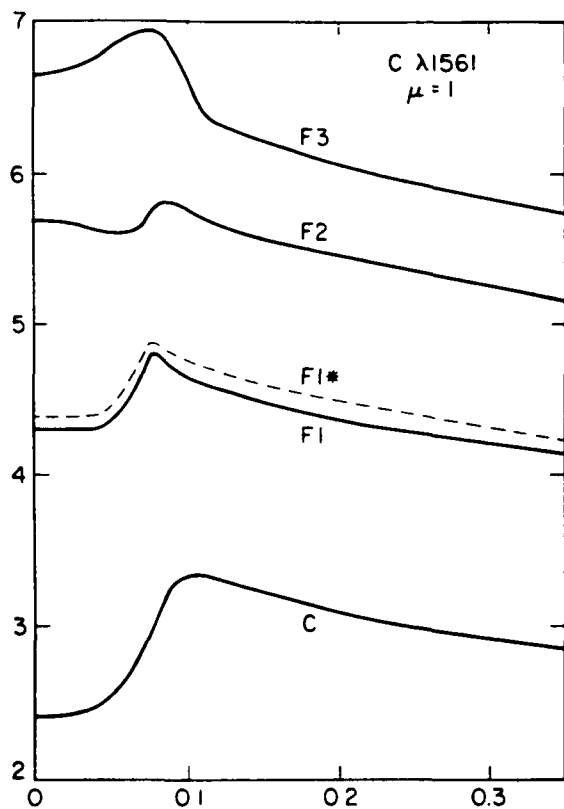


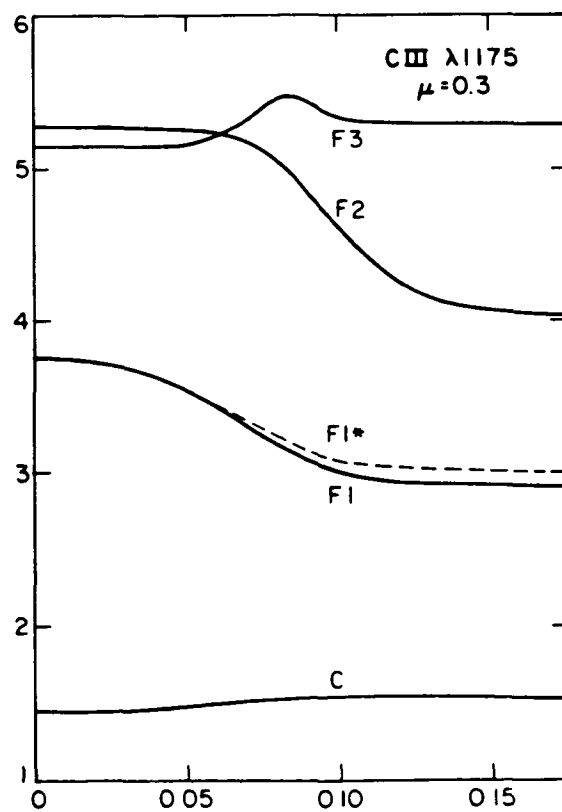
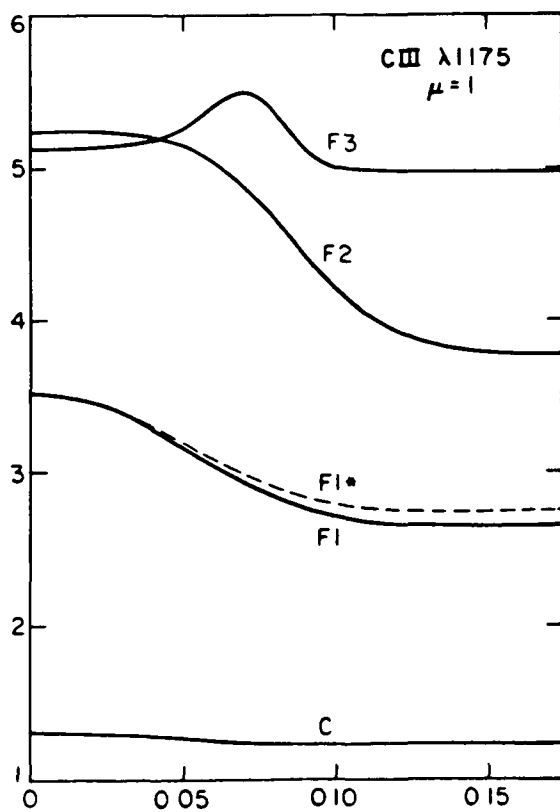
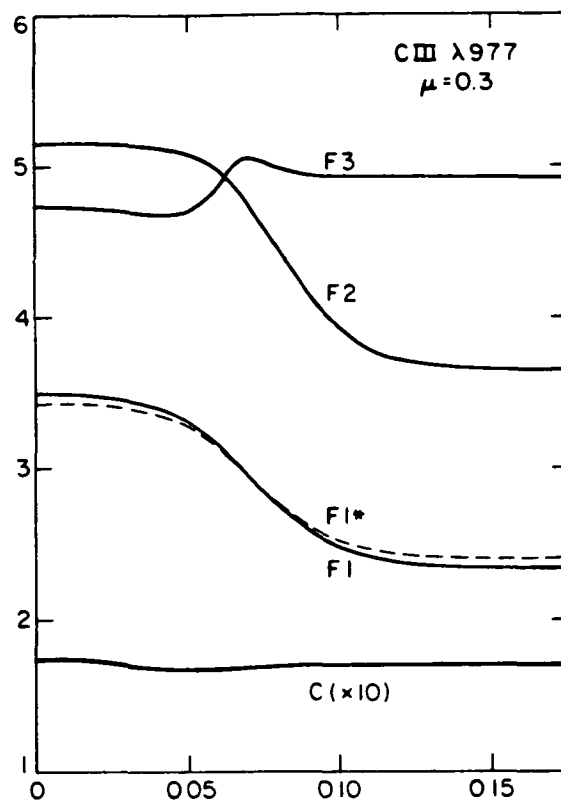
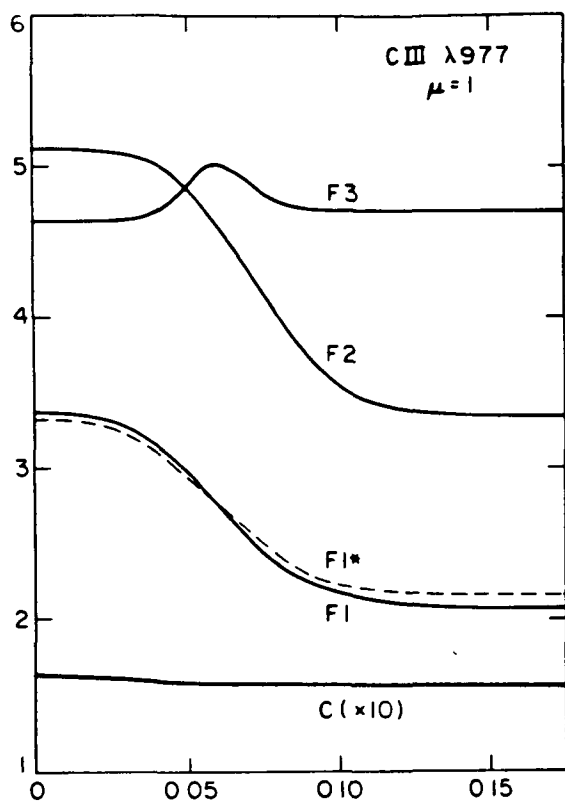


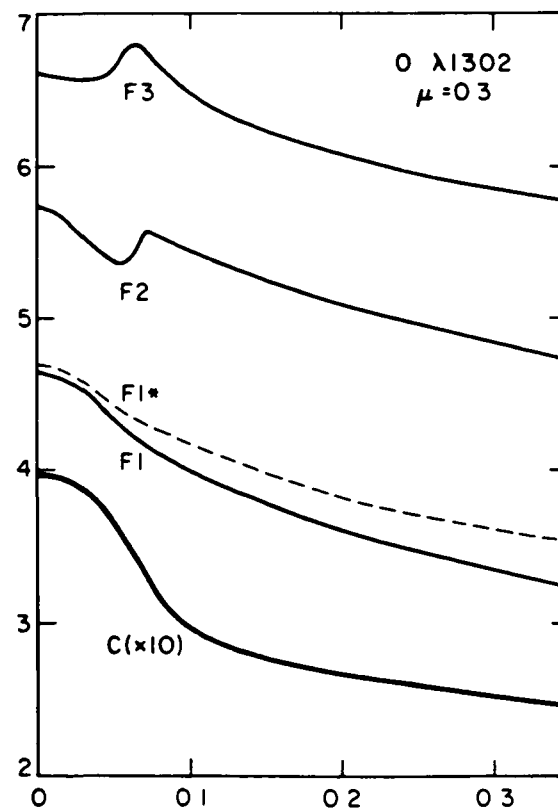
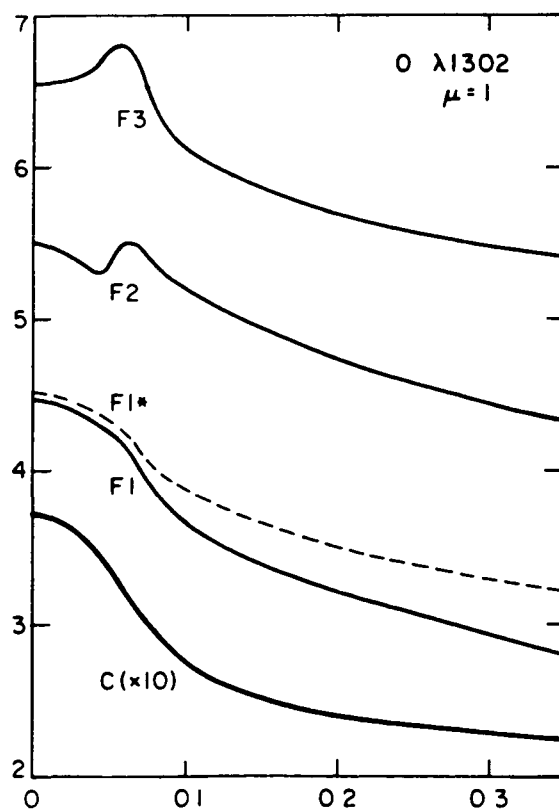
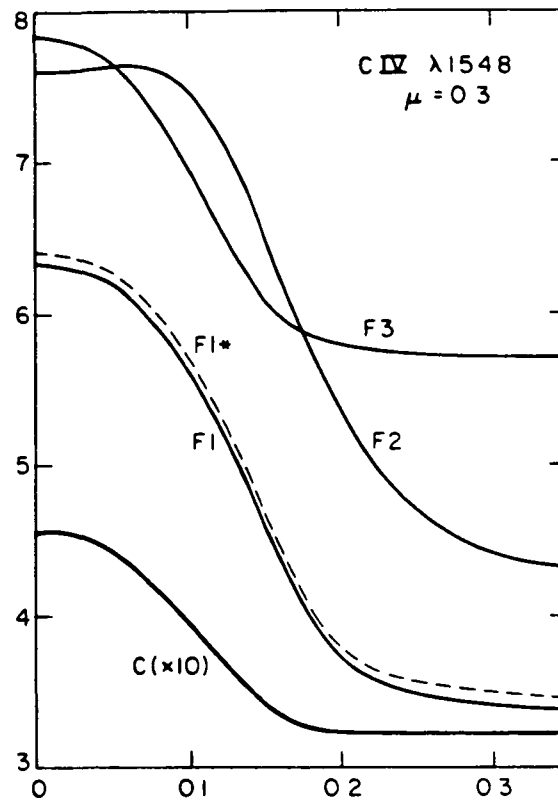
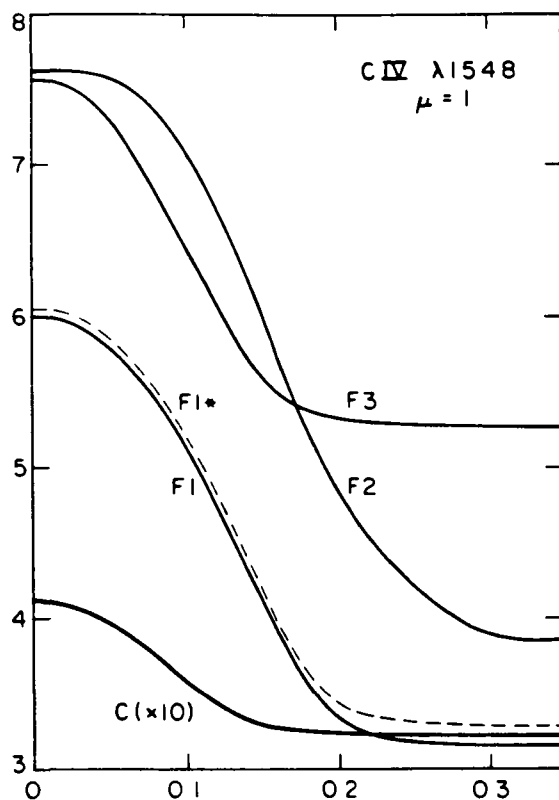


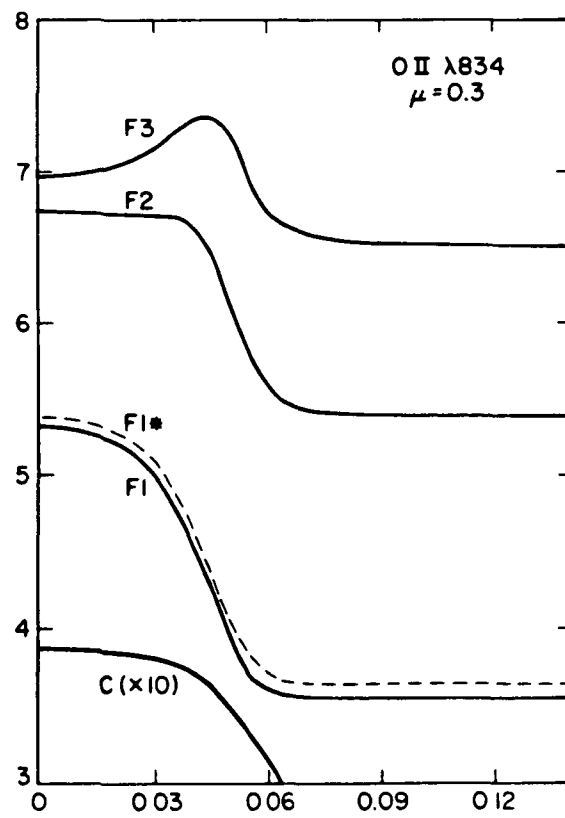
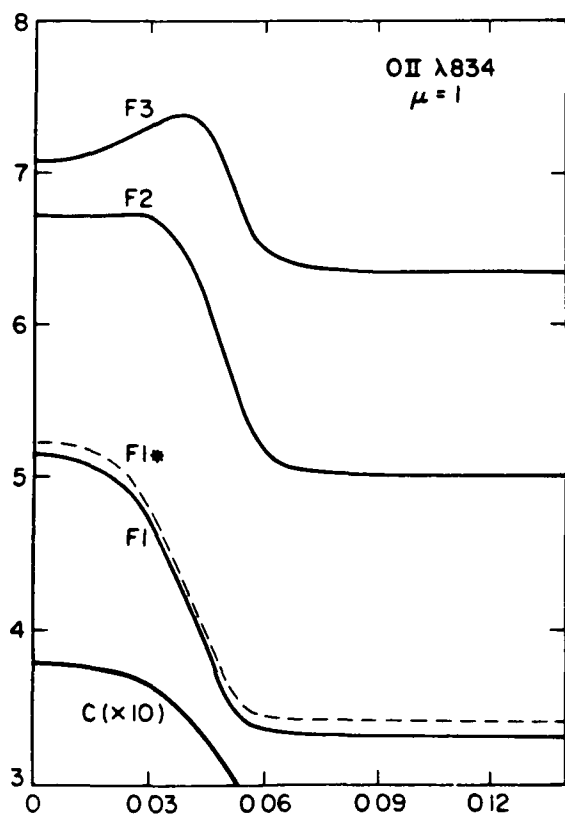
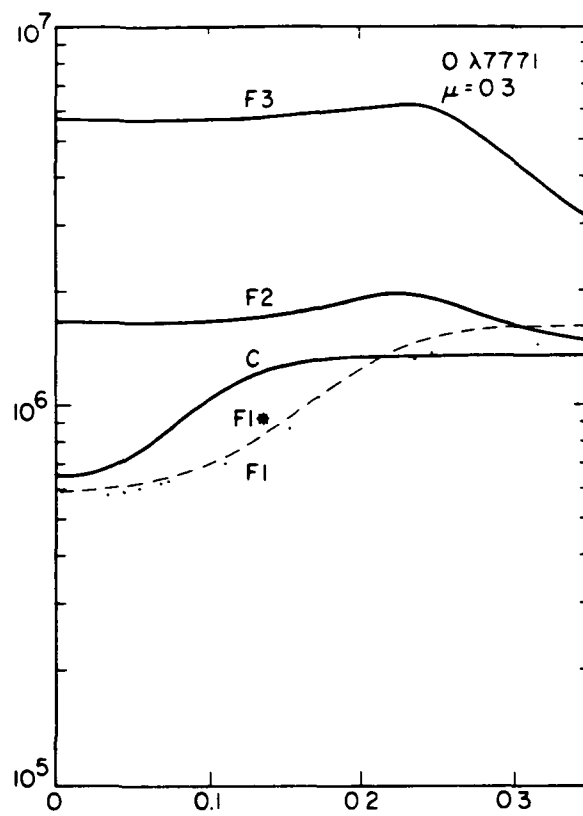
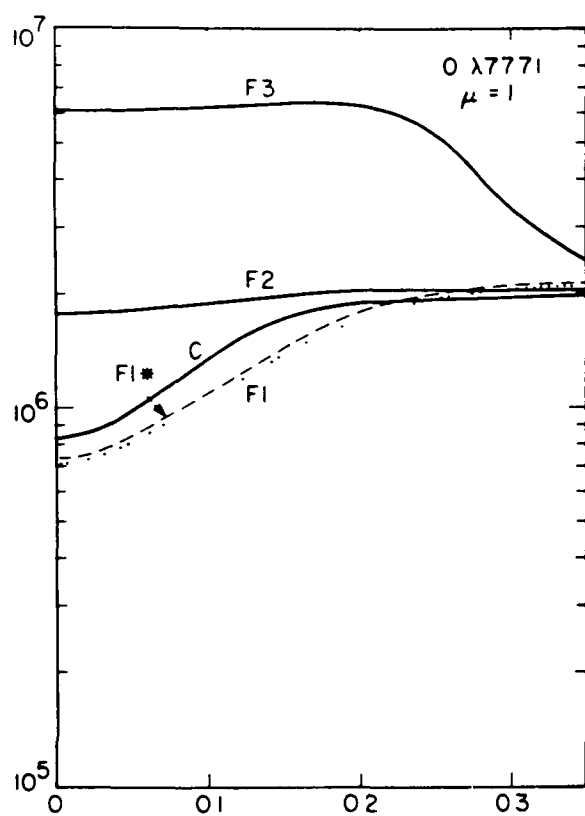












Ca II, Fe), Machado and Linsky (1975; Ca II), Machado and Emslie (1979; C II, $L\alpha$), MAVN ($L\alpha$, LyC), Cohen *et al.* (1978; CIV), Porter *et al.* (this volume; He I-II), Zirin and Hirayama (1985; He I-II), Lites and Cook (1978; $L\alpha$), Lemaire *et al.* (1984; Ca II, Mg II, $L\alpha$), and Canfield and van Hoosier (1980, $L\alpha$). This list of references is by no means complete. Further information on the qualitative behavior of most of the visible lines we compute is given by Machado and Rust (1974) and Svestka (1976), who gives complete references up to 1975.

The computed profiles in Figure 7 are symmetric because the models are static. We have used the same nonthermal broadening velocity as in the VAL (1981) calculations. The profiles have not been convolved with any macroturbulent velocity distribution or any instrumental profile. Doing so would broaden the central core of the profiles, giving better agreement with observations; see, for example, Fang *et al.* in this volume. Thus we should not expect close agreement between these computed profiles and observed ones.

We now proceed to note particular features of the calculated results.

$L\alpha$ and $H\alpha$ lines These, together with Ca II H and K, are the best observed lines in the flare spectrum. The $H\alpha$ line is particularly well observed. (It should be noted that the $H\alpha$ profiles we now compute for models F1 and F2 are somewhat broader than those shown by MAVN, for the reason that the adopted resonance broadening coefficient was too small by the factor 2 in the earlier calculation.) The high densities in the F3 model give an $H\alpha$ profile with very broad wings, as is observed in many chromospheric flare kernels (see Svestka 1976 and references therein). However, the absolute intensity at the center of the F3 profile is too large compared with observations, suggesting that a model having a chromospheric temperature rise between the F2 and F3 distributions would be in better agreement with the brightest flares seen in $H\alpha$. Similar conclusions apply to the $L\alpha$ line, except that even the F1 profile has a larger central intensity than reported by Canfield and van Hoosier (1980). Additional details for comparison with observed $L\alpha$ wing profiles are given by MAVN.

Helium lines These lines are discussed by Lites *et al.*, Porter *et al.* and Zirin elsewhere in this volume. Our results are incomplete because we have not introduced large values of the incident coronal XUV flux in the flare models. For simplicity we continued to use the model C values. Even so, the qualitative behavior of the calculated D3 line is in agreement with flare observations, showing absorption in the weak flare models, changing to emission in models F2 and F3. (The F3 profile again seems too large, as compared with the observations by Donati-

Falchi *et al.* 1984.) It is well known (see Svestka 1976 and references therein) that D3 shows both emission and absorption components at different spatial locations associated with bright and faint H α regions. The computed profiles show these properties. We also note that the overall behavior of the He I and He II lines shows the increasing importance of collisional effects as we proceed from model C through F3, in agreement with the results of Porter *et al.* for chromospheric flare ribbons. Note that while the wings of the $\lambda 1640$ He II line are higher for the F3 model than for F2, the central intensity that we compute is lower. A possible cause of this result is explained in the discussion of the higher-temperature lines below.

Na and Fe lines The qualitative behavior of the Na D₂ line is in good agreement with observations. This line is known to show a filling-in of the absorption core in most flares, going into emission only in the brightest events. The same applies to the behavior of the Fe lines. Observations indicate that the Fe line at 3719Å is extremely sensitive to flare conditions while the 5012Å line shows emission-core brightenings only in the largest events (Svestka 1966; Machado and Rust 1974). Our calculated profiles show the same properties.

Ca II and Mg II lines These collisionally dominated lines are extremely useful in determining the structure of flaring atmospheres from the upper photosphere to the base of the transition zone. The wavelength shift of the minimum intensity in the wing of the K line corresponds to the changing mass column density of the minimum temperature in the sequence of models. The progressive increase of the pressure at the top of the chromosphere from F1 to F3 causes a filling-in of the central reversal. The F1* wing profile shows the effect of the hotter upper photosphere, which also clearly affects the $\lambda 8498$ infrared profile. Similar results are obtained for the Mg II k line, which has been analyzed in detail by Lemaire *et al.* (1984). These authors also analyzed Mg II h, Ca II H and K, and L α , noting that the F1 model of MAVN underestimated the observed Mg II emission, while F2 overestimated the intensities in the other lines.

Higher-temperature lines It should be emphasized here that the flare-model transition regions ($T \gtrsim 10^4$ K) have been defined rather arbitrarily. MAVN found that the computed L α /L β ratio is very sensitive to the amount of material between 10^4 and 3×10^4 K, and the transition-regions of models F1 and F2 were adjusted to fit observed values of this ratio. In a subsequent unpublished study, the two models were found to have too much mass in the upper part of the transition regions, compared with results from energy balance calculations. For the F3 model we have attempted to estimate an energy-balance model, following

Machado and Emslie (1979), assuming for simplicity that the divergence of the conductive flux equals the radiation loss from the transition region. The result is preliminary, however, and needs further study. We have not attempted to modify the upper transition-region structure of models F1 and F2. (Note that the F1* transition region is identical to F1.) As a consequence, we sometimes obtain higher central intensities from model F2 than from F3. This is apparent in the calculated profiles of the $\lambda 1547$ line of C IV, the $\lambda 977$ and $\lambda 1175$ lines of C III, and the $\lambda 1640$ line of He II (as noted above). In the near future we hope to improve the physical modeling of the flare transition regions. Note that for models F2 and F3 at least, lines such as $\lambda 977$ and 1175 of C III, which are formed high in the transition region, show the effects of large opacities. Such effects need to be taken into account in the calculation of energy balance models; i.e., the radiative cooling calculations should include radiative transfer effects.

To conclude this section, the calculated net radiative cooling rates are given for models F1, F1*, F2, and F3, due to H, H⁻, Ca II, Mg II, and the group of contributors Fe, Na, Mg, Si, C, and He I-II. These atoms and ions include many lines, but we have not included a contribution due to all the other lines throughout the spectrum, i.e., due to the sampled or representative line opacities considered earlier. For model C the effect of this omission can be estimated by comparing Figures 23a and 24 shown by Avrett (1985).

Figure 23a of that paper gives the total net radiative cooling rate without the effect of the additional lines, while Figure 24 shows the corresponding result obtained by integrating over the spectrum in detail, thus including the additional lines. (The two results differ substantially in the upper chromosphere because the integration does not include the central portions of strong lines.) In the temperature minimum region and low chromosphere, the additional lines have an effect but do not qualitatively change the result. In particular, the total rate remains negative in the temperature minimum region.

The additional lines are more important in the flare models than in model C, and thus may make a greater contribution to the flare cooling rates than to the model C cooling rates. At a later time we will attempt to calculate the total cooling rate including the effect of the additional lines. The other contributions to the net radiative cooling rates are given below.

Figure 8 shows the calculated cooling rate in $\text{ergs cm}^{-3} \text{s}^{-1}$ as a function of height in km for models F1, F1*, F2, and F3. In each case we show 1) the total.

and the individual contributions from H, H⁻, Ca II, Mg II, and "others", 2) the H total with contributions from L α , H α , and the Balmer continuum, 3) the H⁻ total with bound-free and free-free contributions, 4) the Ca II total with contributions from the H, K, and infrared triplet lines, 5) the Mg II total with h and k contribution, and 6) the total and individual contributions from Fe, Na, Mg, Si, C, and He I-II.

Several interesting features of these results should be noted:

1) The F1 minimum temperature is high enough (in relation to the temperature values at other heights) to keep the total cooling rate positive in the minimum region, in contrast to the negative total rates for the three quiet-Sun models discussed by Avrett (1985, Figure 23).

2) The H⁻ bound-free cooling rate is negative in the minimum region for model F1 even though the total is positive.

3) The higher minimum temperature values in the F1* model cause the H⁻ bound-free rate to be positive instead of negative.

4) This H⁻ rate is again negative in model F2.

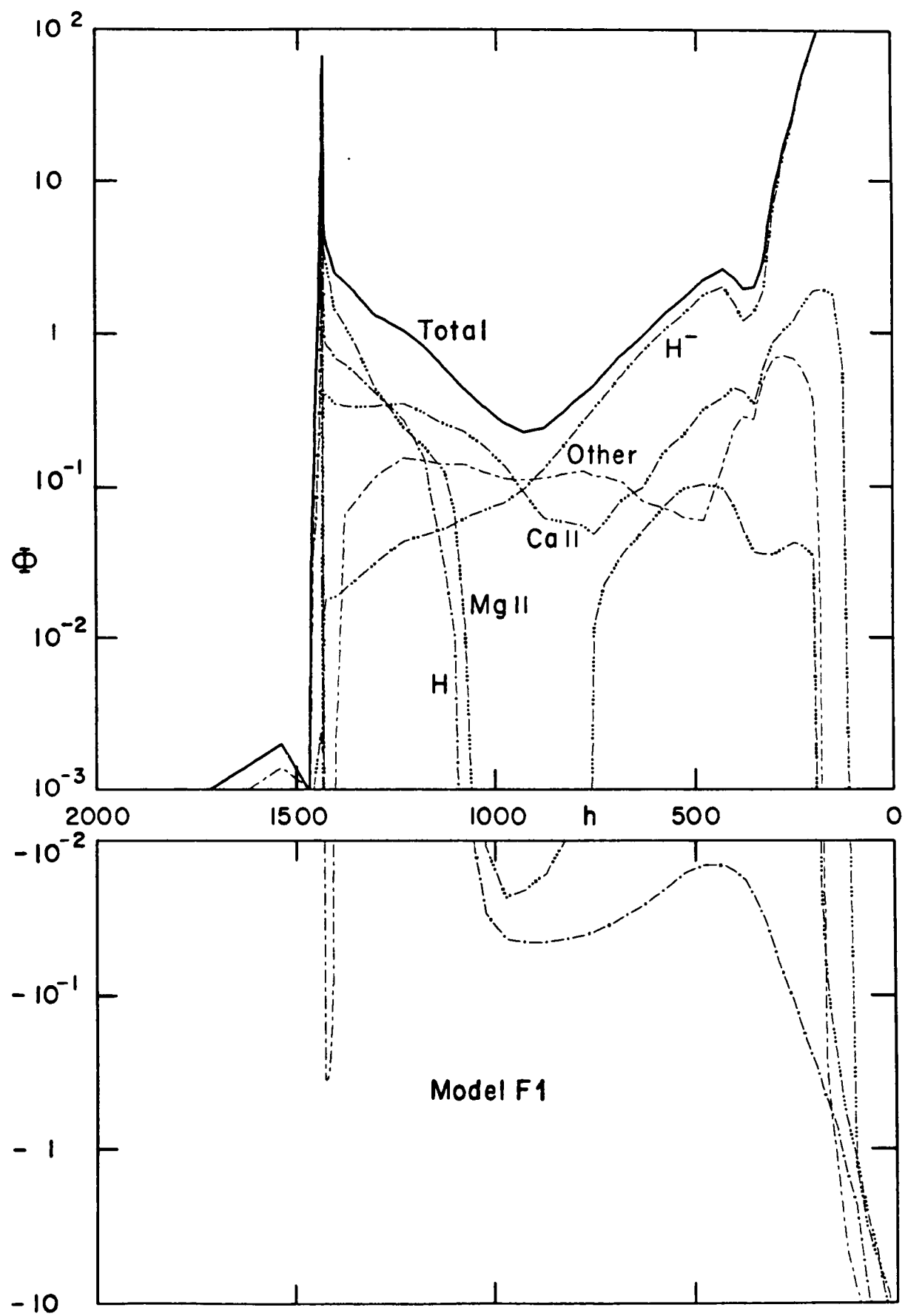
5) In model F3, all of the principal contributions are negative in the minimum region.

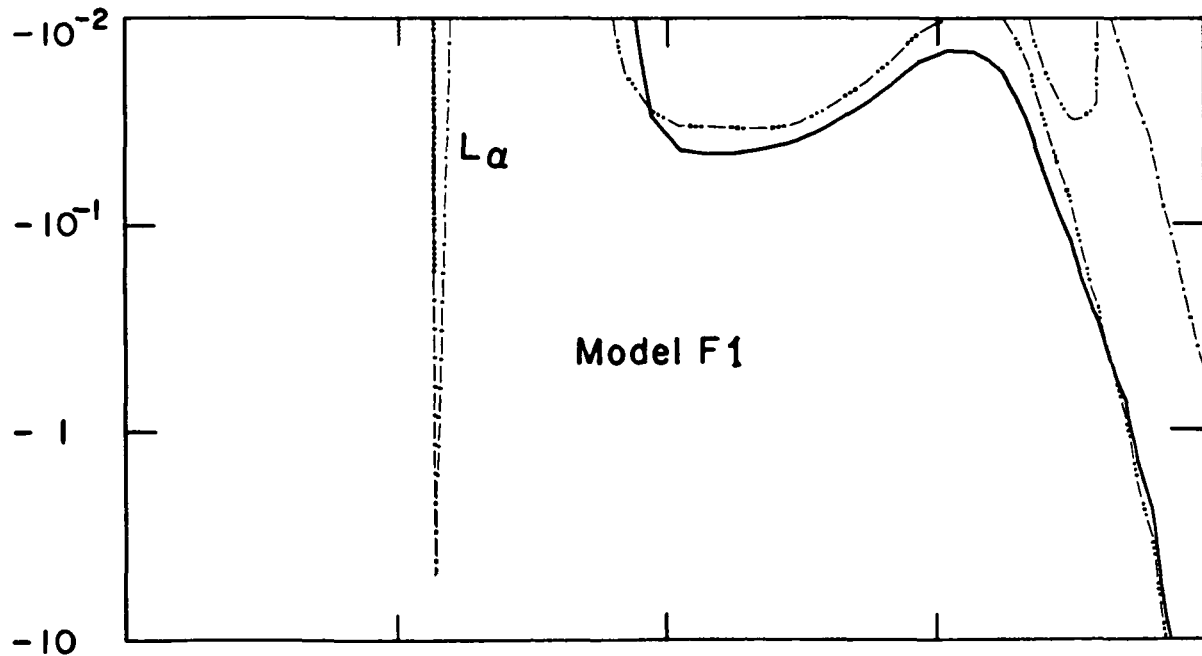
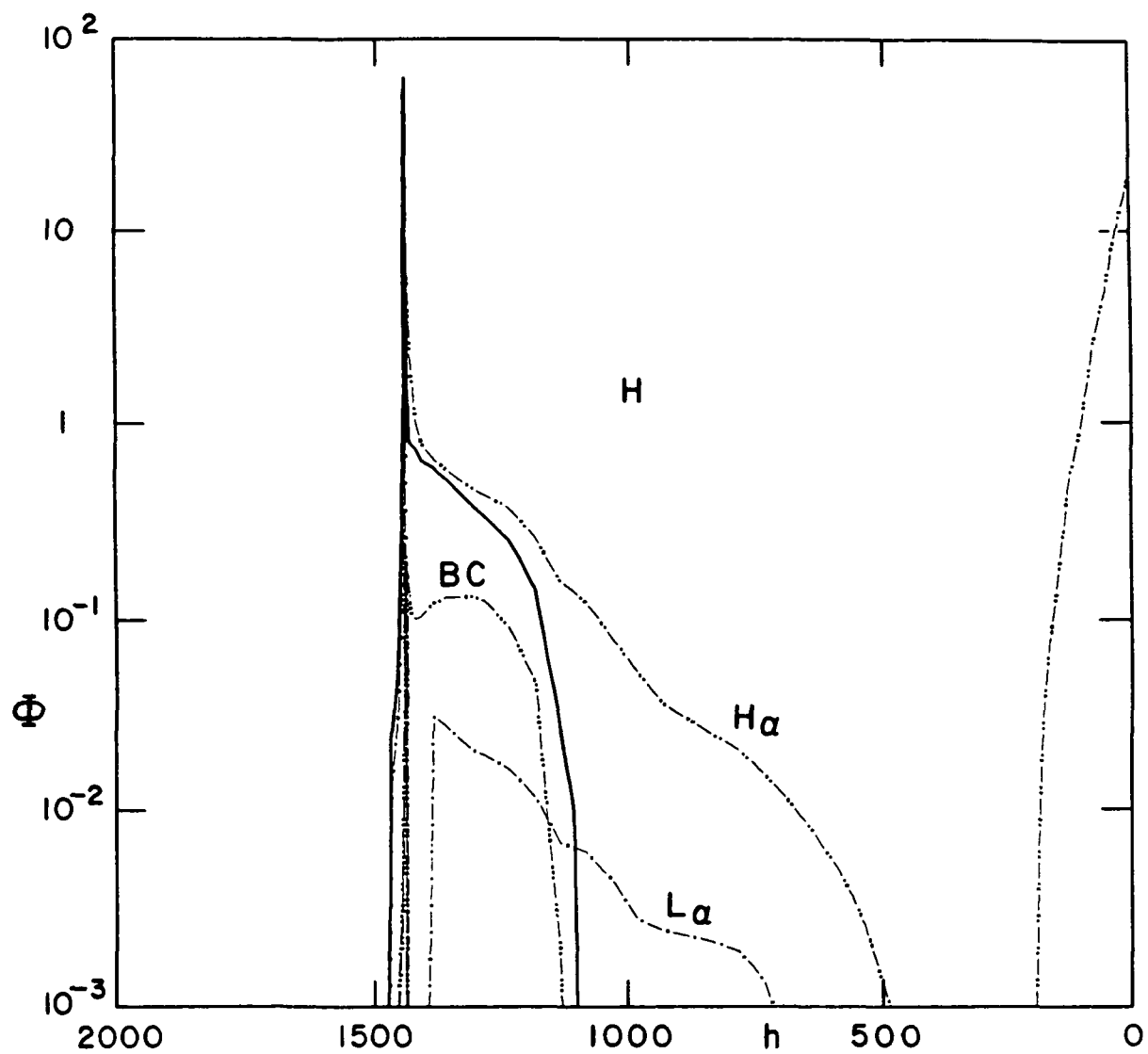
The net radiative cooling rate Φ plotted in these figures is given by

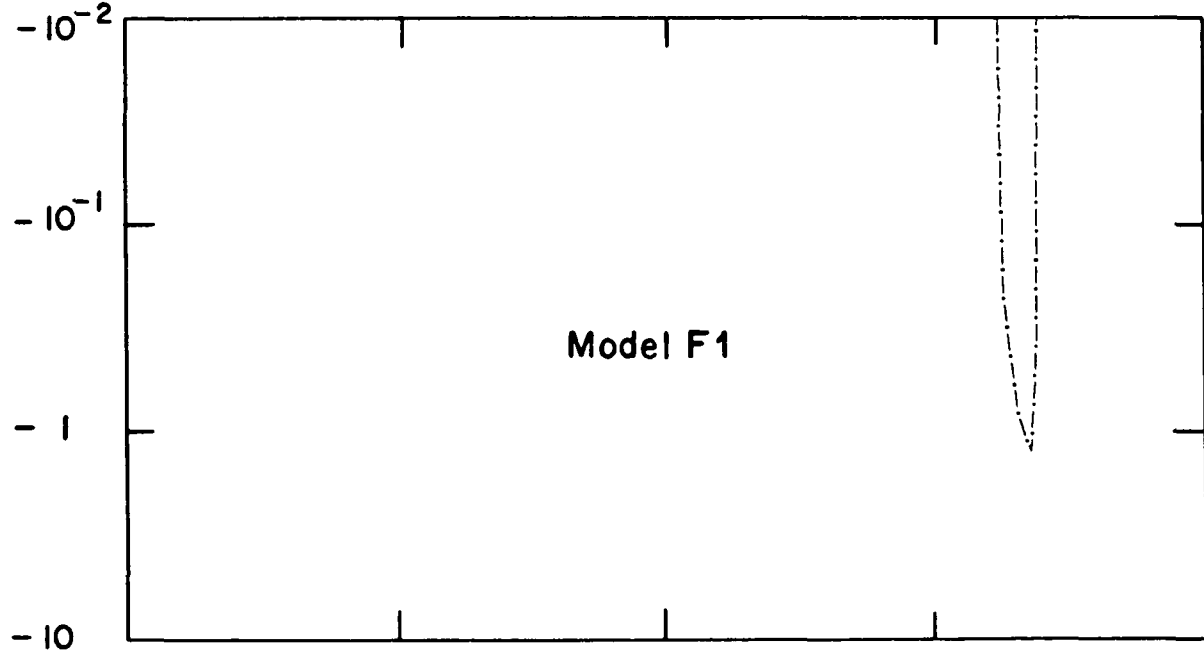
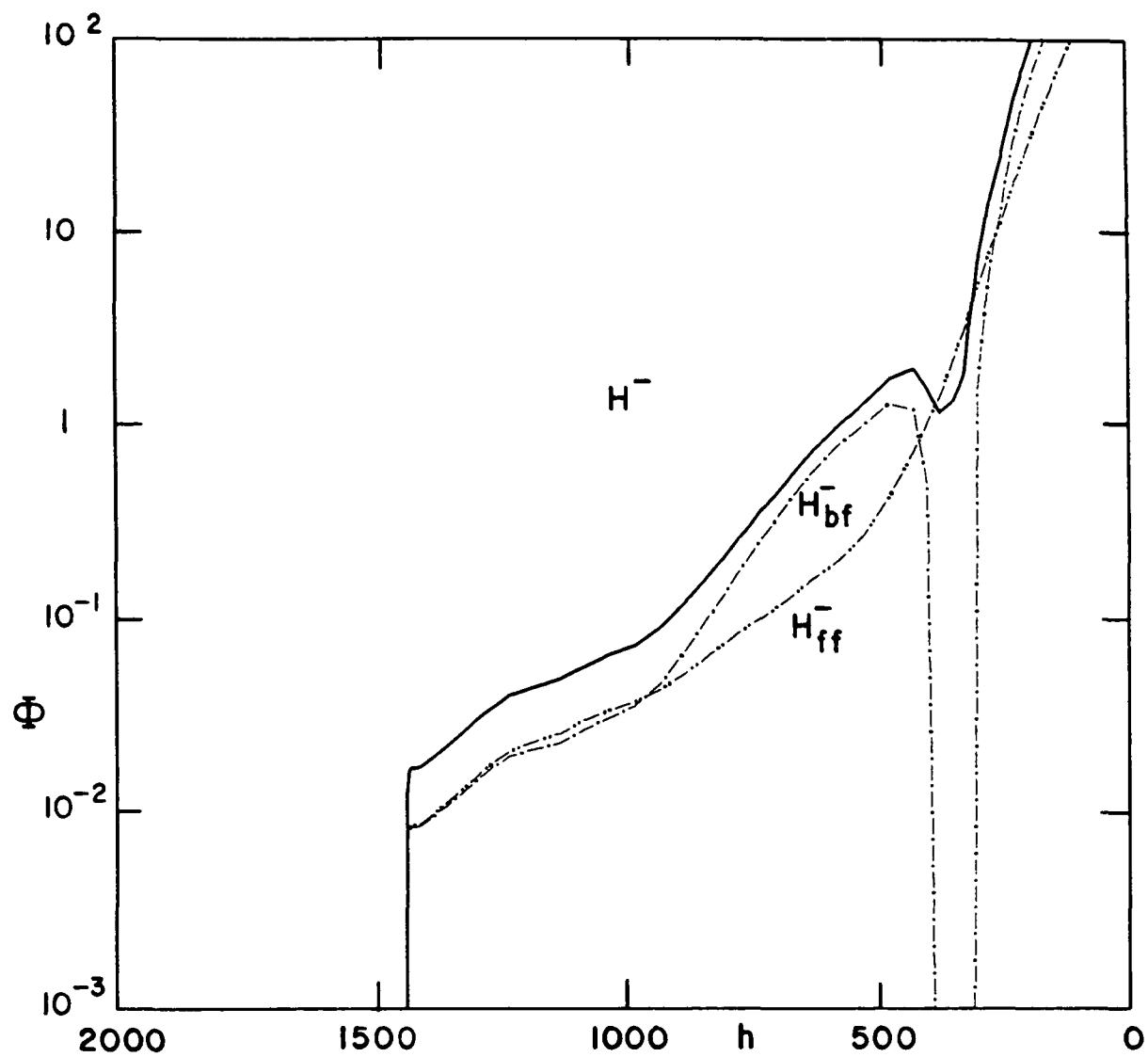
$$\Phi = 4\pi \int \kappa_{\nu} (S_{\nu} - J_{\nu}) d\nu$$

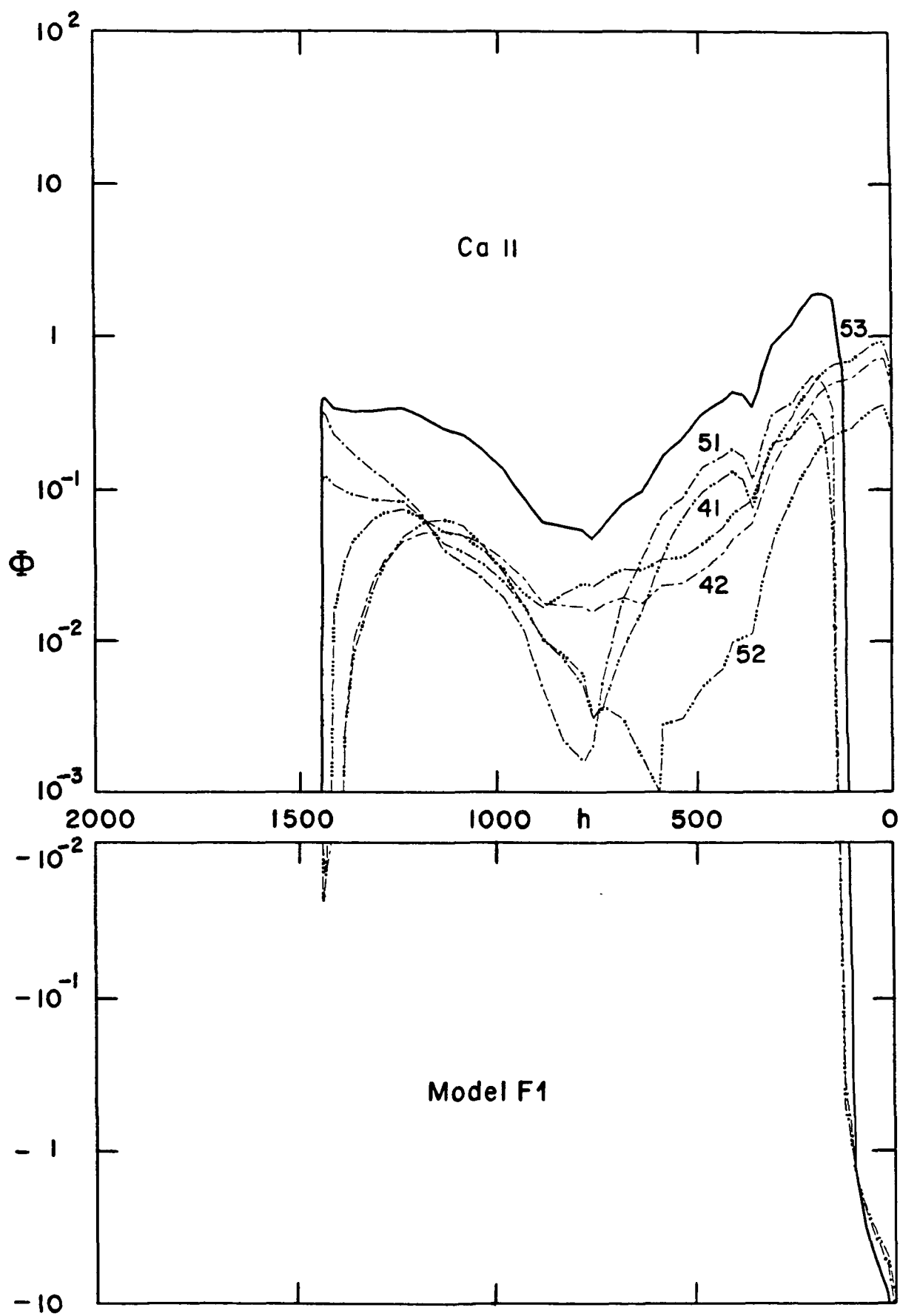
where κ_{ν} is the opacity (in cm⁻¹), S_{ν} is the source function, J_{ν} is the mean intensity, and the integral extends over the entire spectrum. Φ is negative at depths where $S_{\nu} < J_{\nu}$ over a sufficient spectral range. We can change Φ from negative to positive by increasing the temperature at the depths where Φ is negative, or

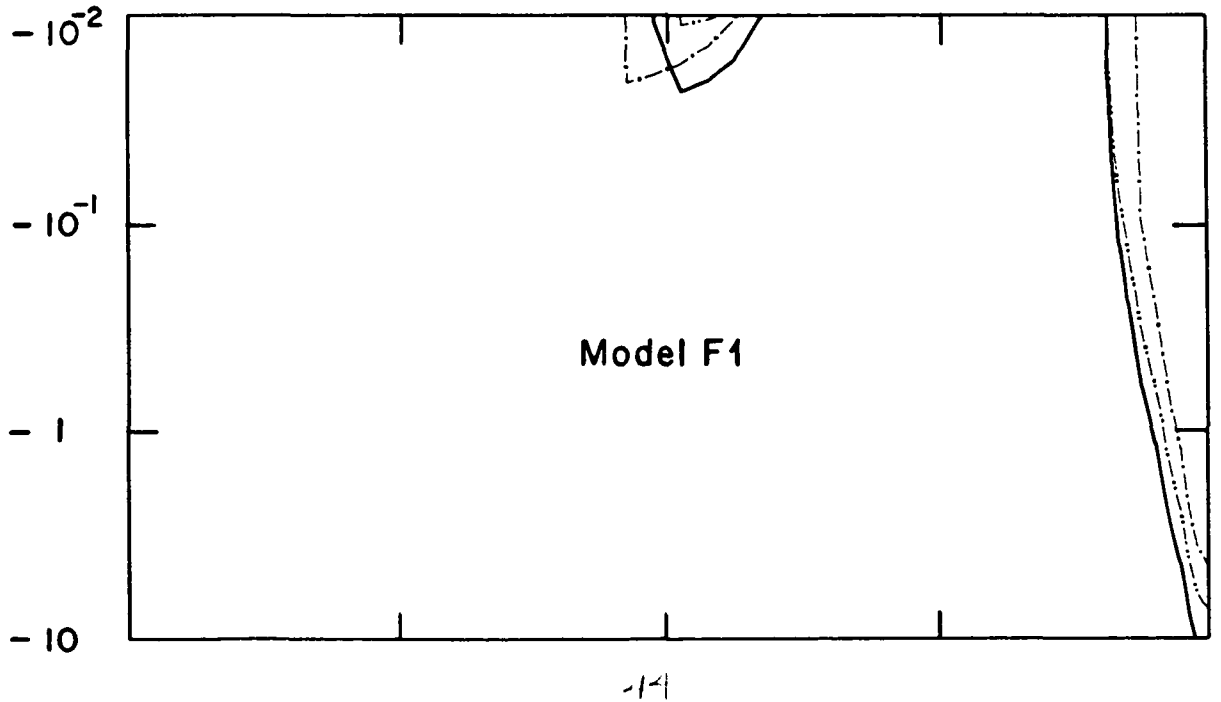
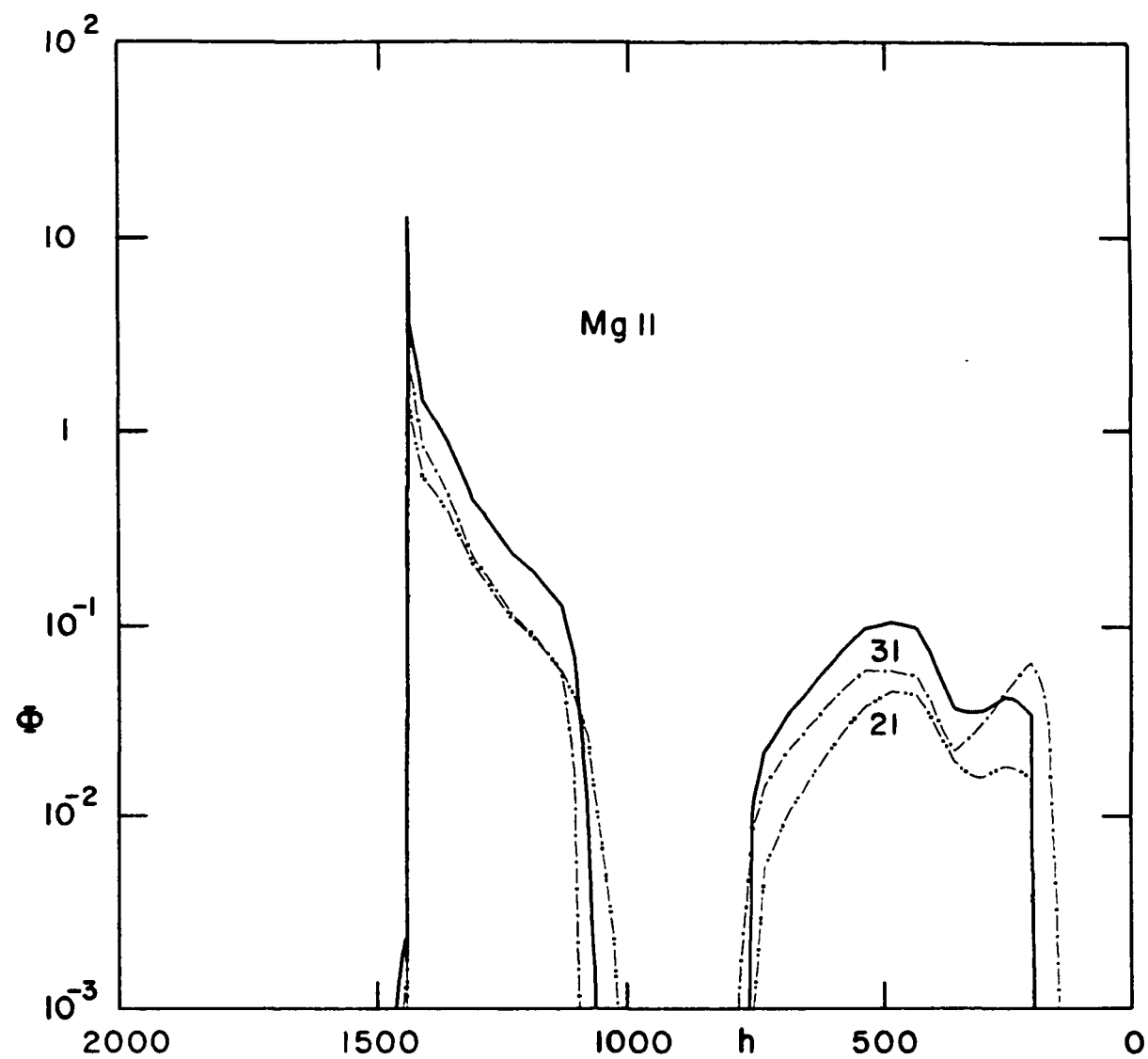
Fig. 8 (next 24 pages) - Calculated net radiative cooling rate Φ in ergs cm⁻³ s⁻¹ as a function of height in km for models F1, F1*, F2, and F3. Six pages are shown for each model as explained in the text.

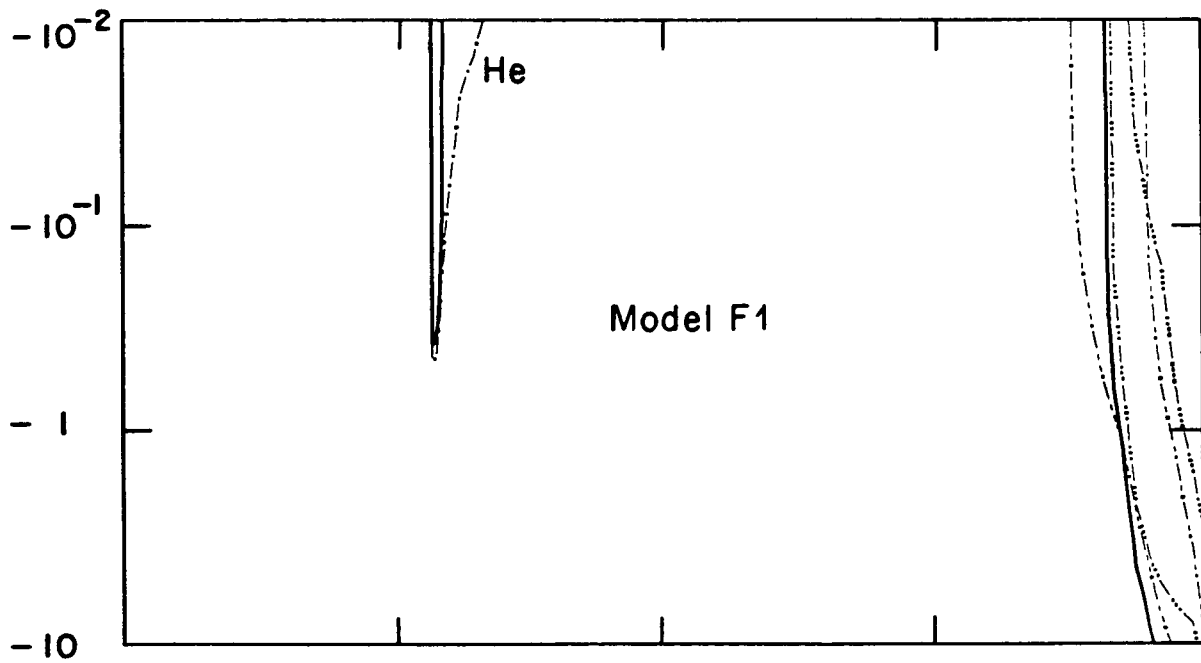
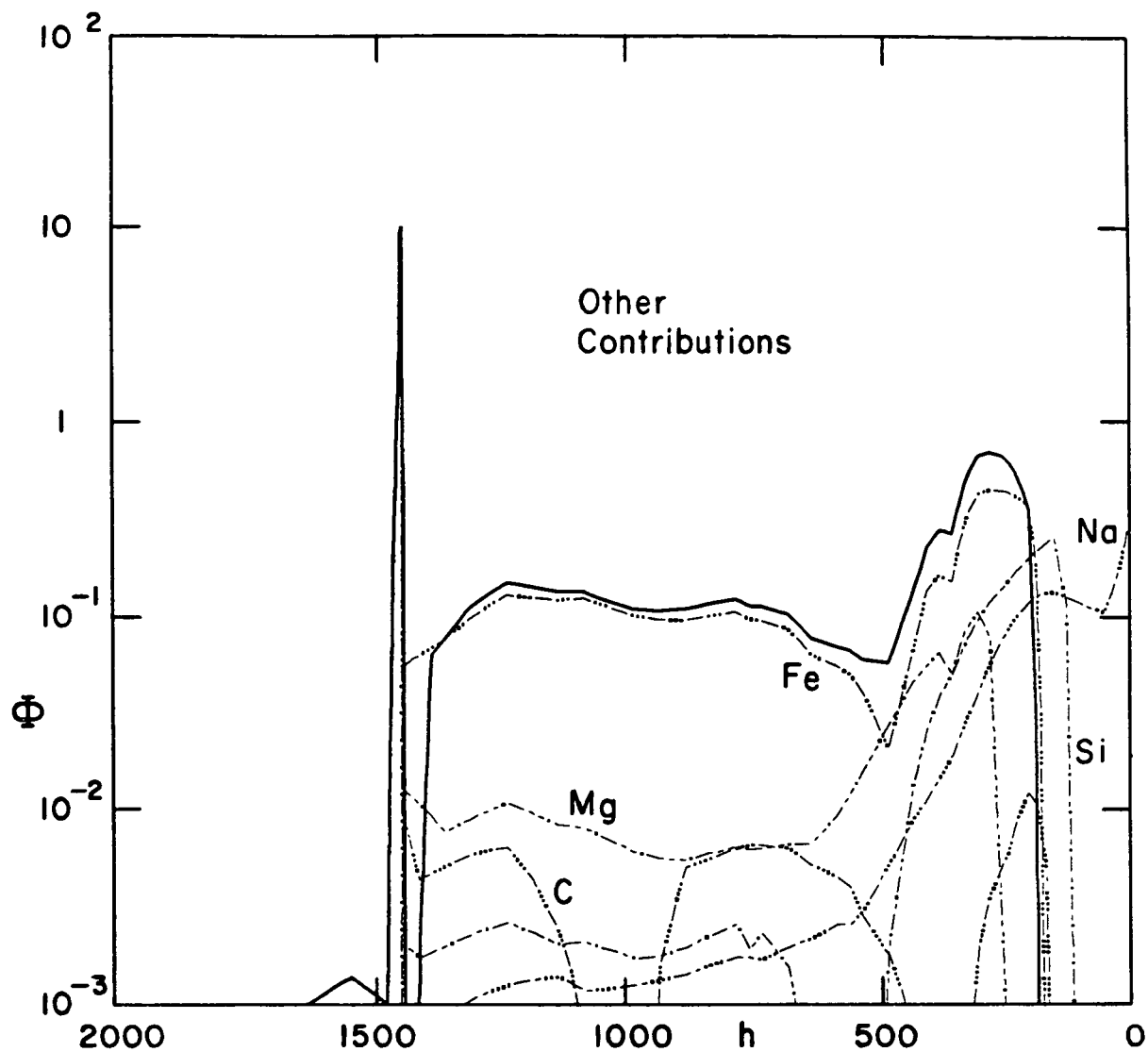


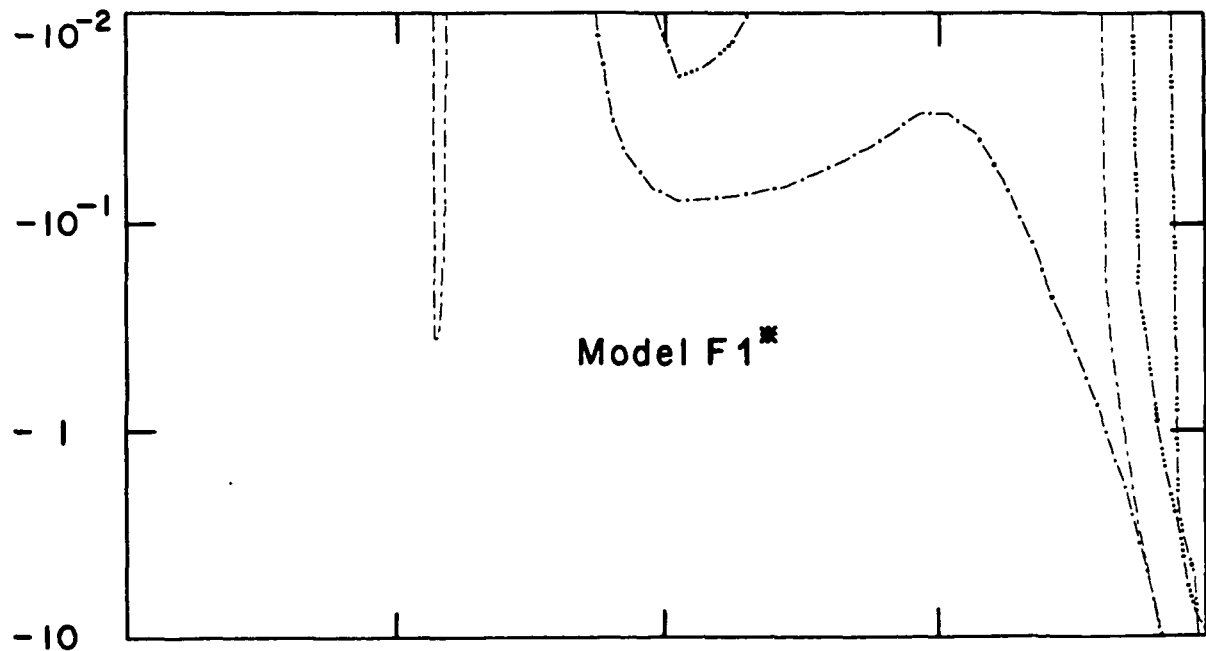
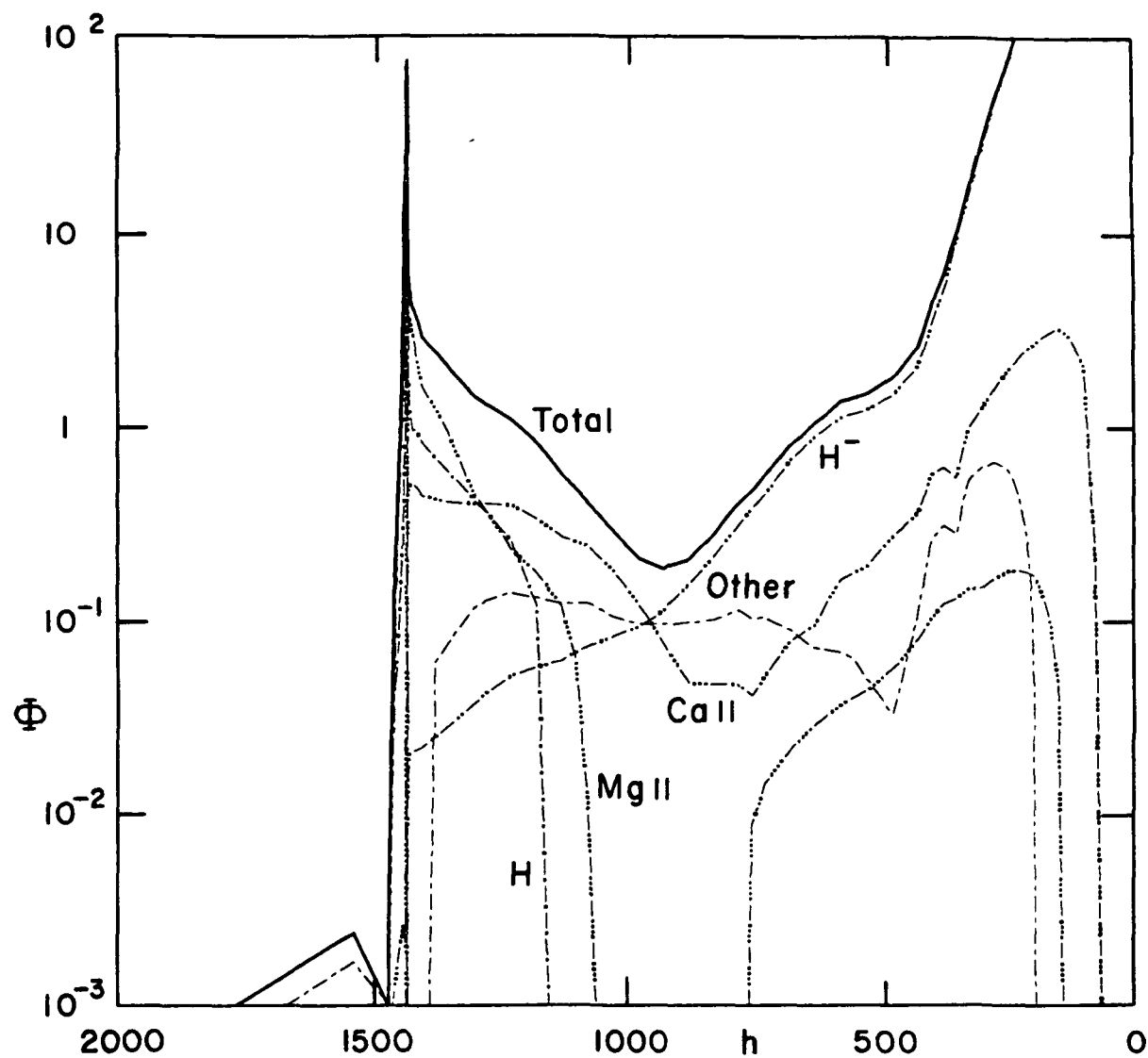


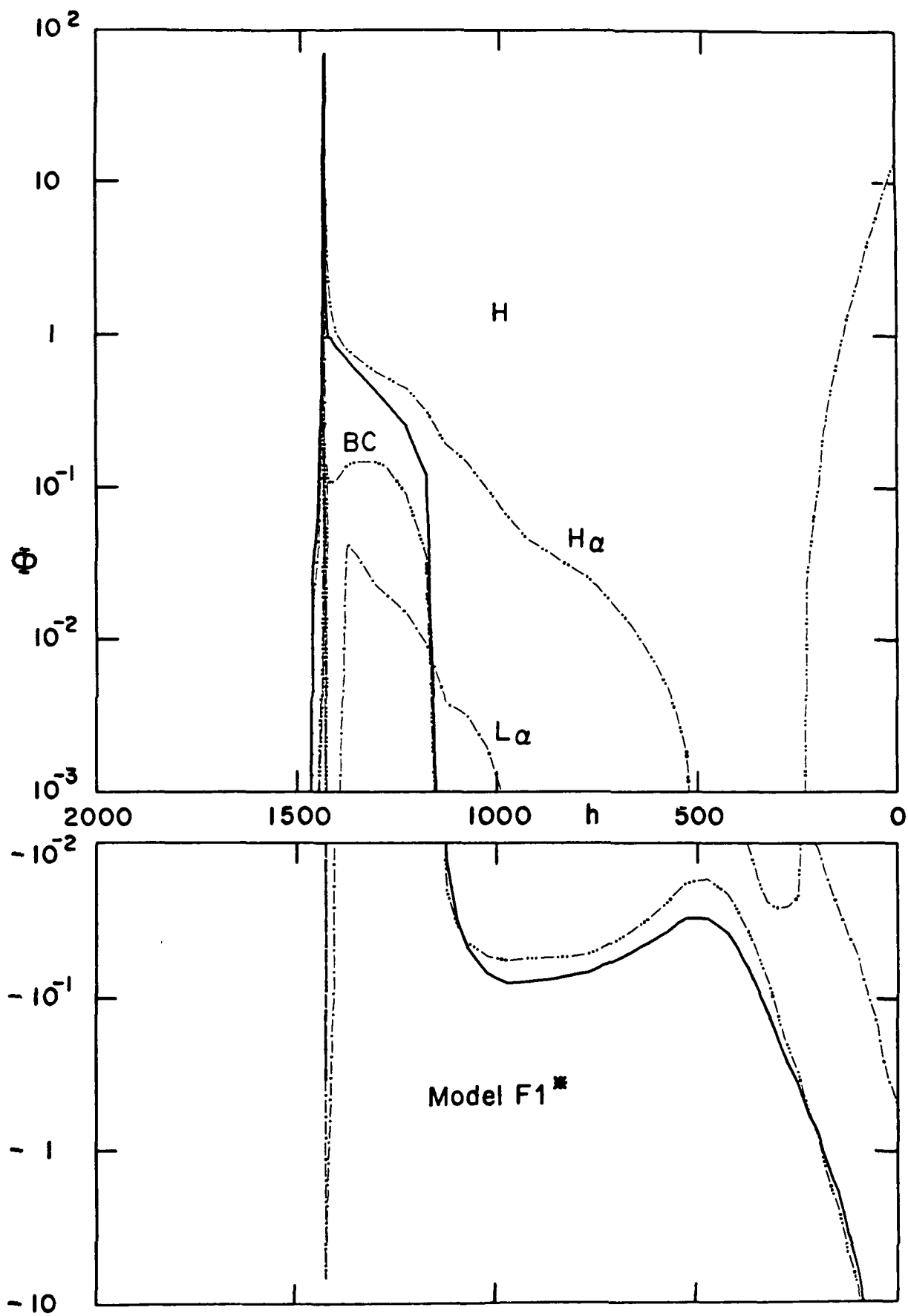


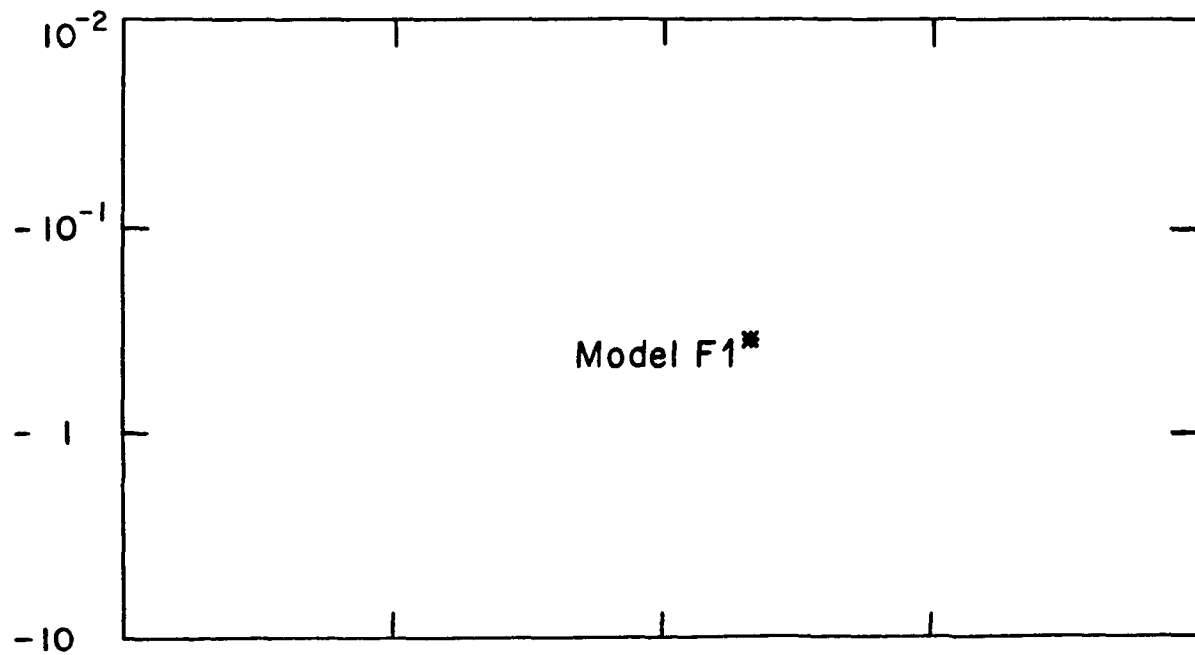
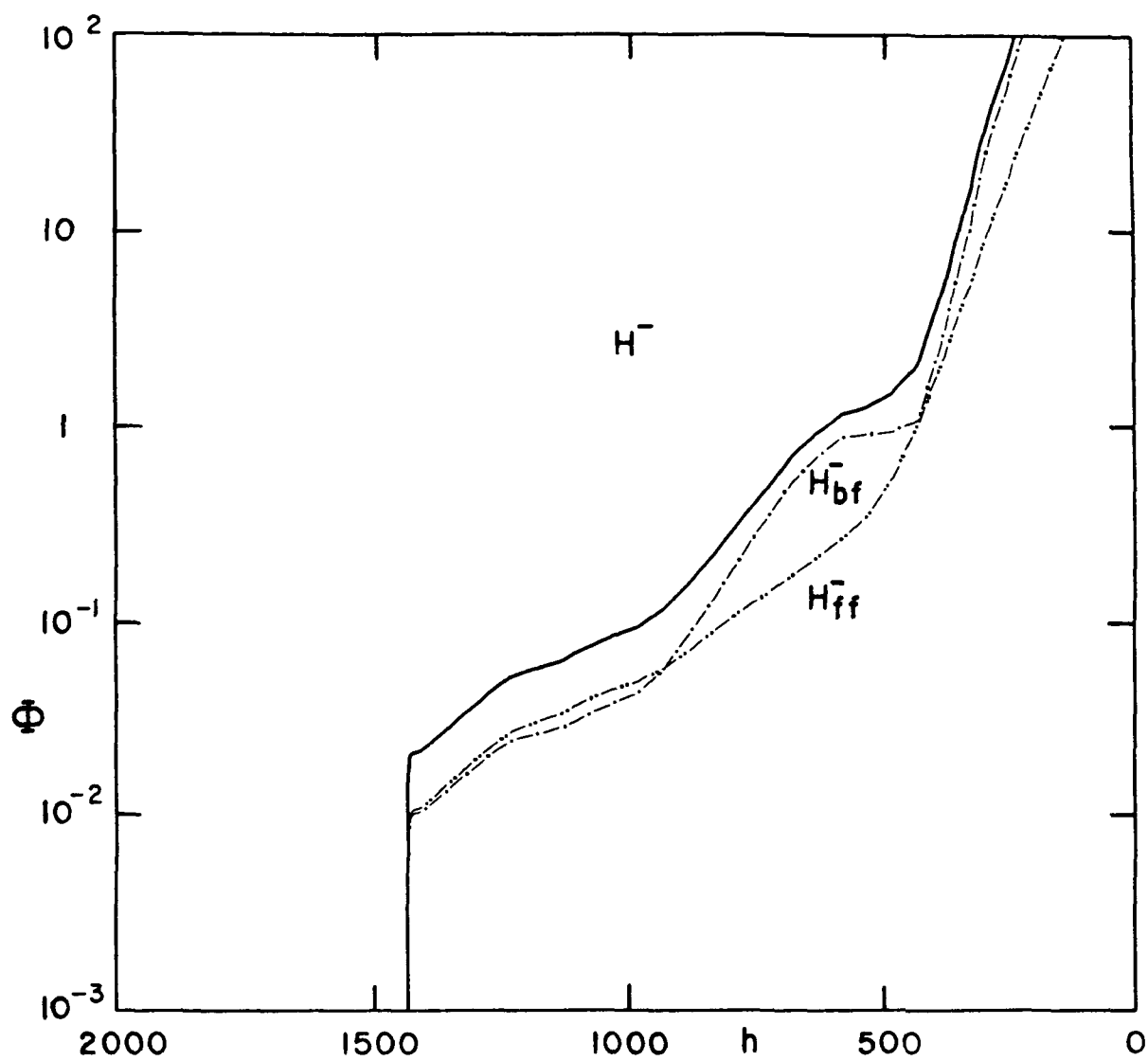


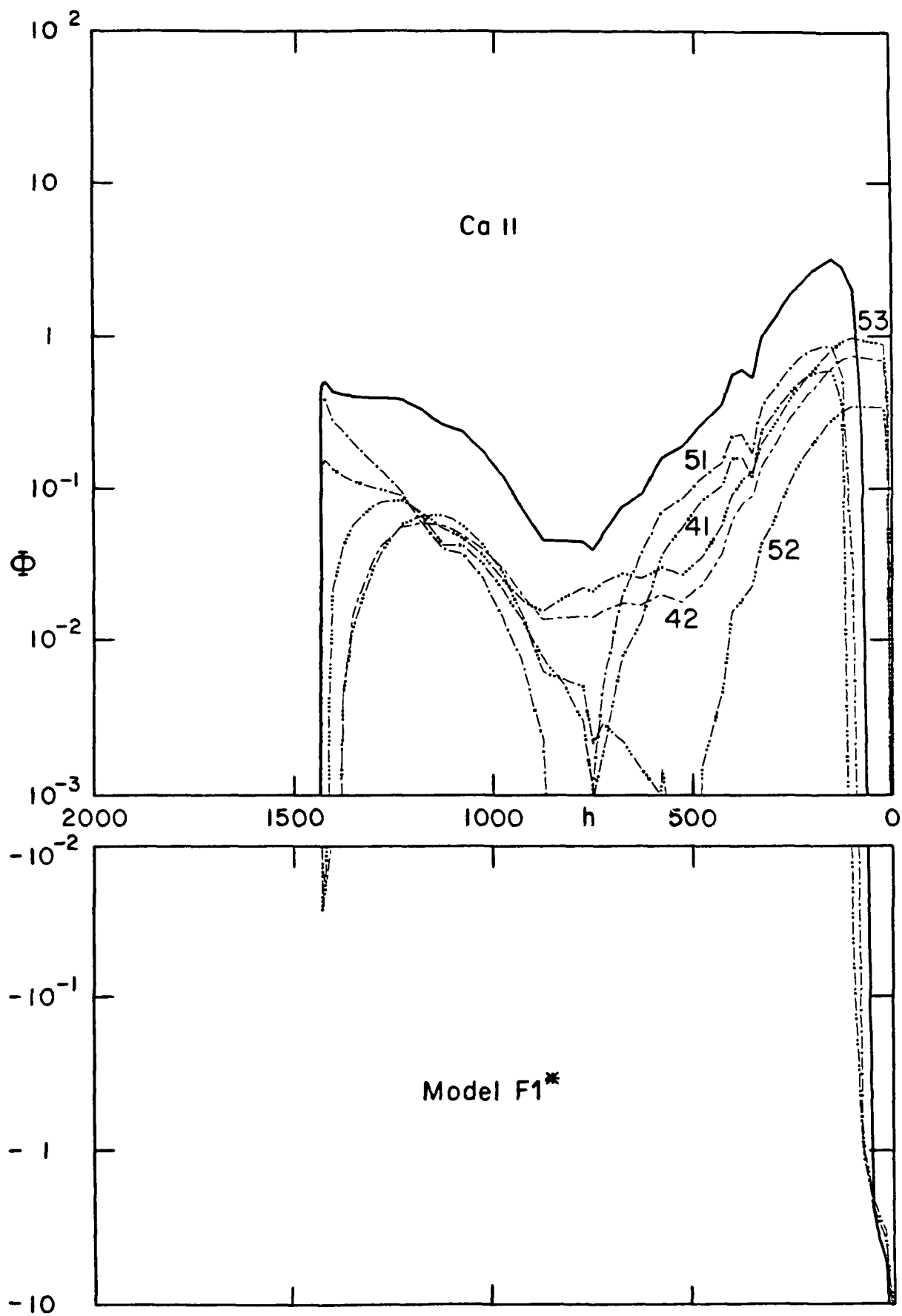


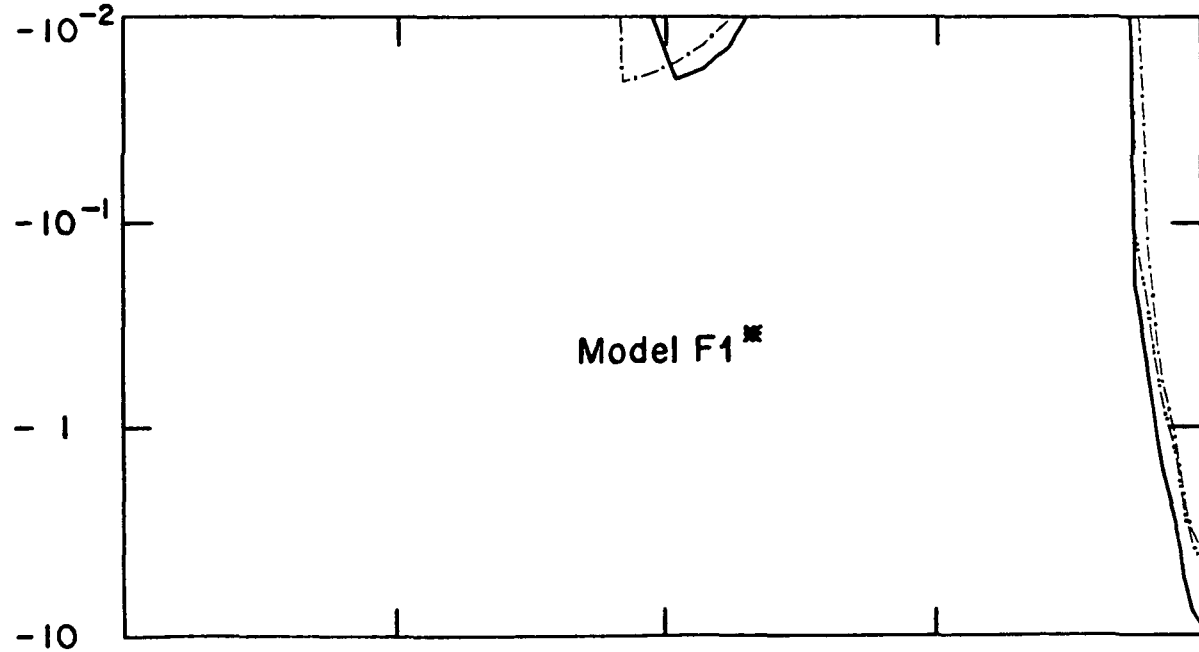
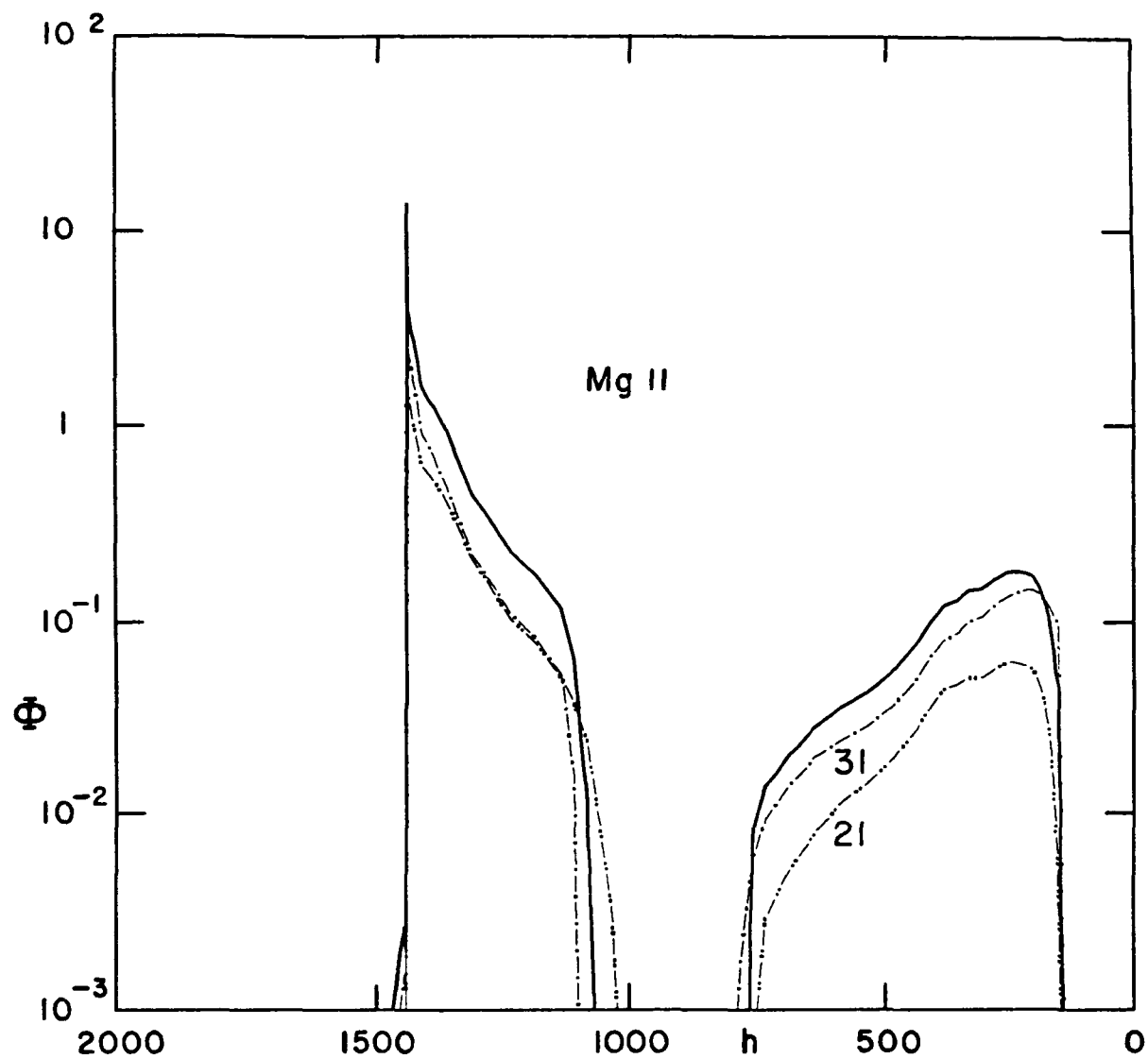


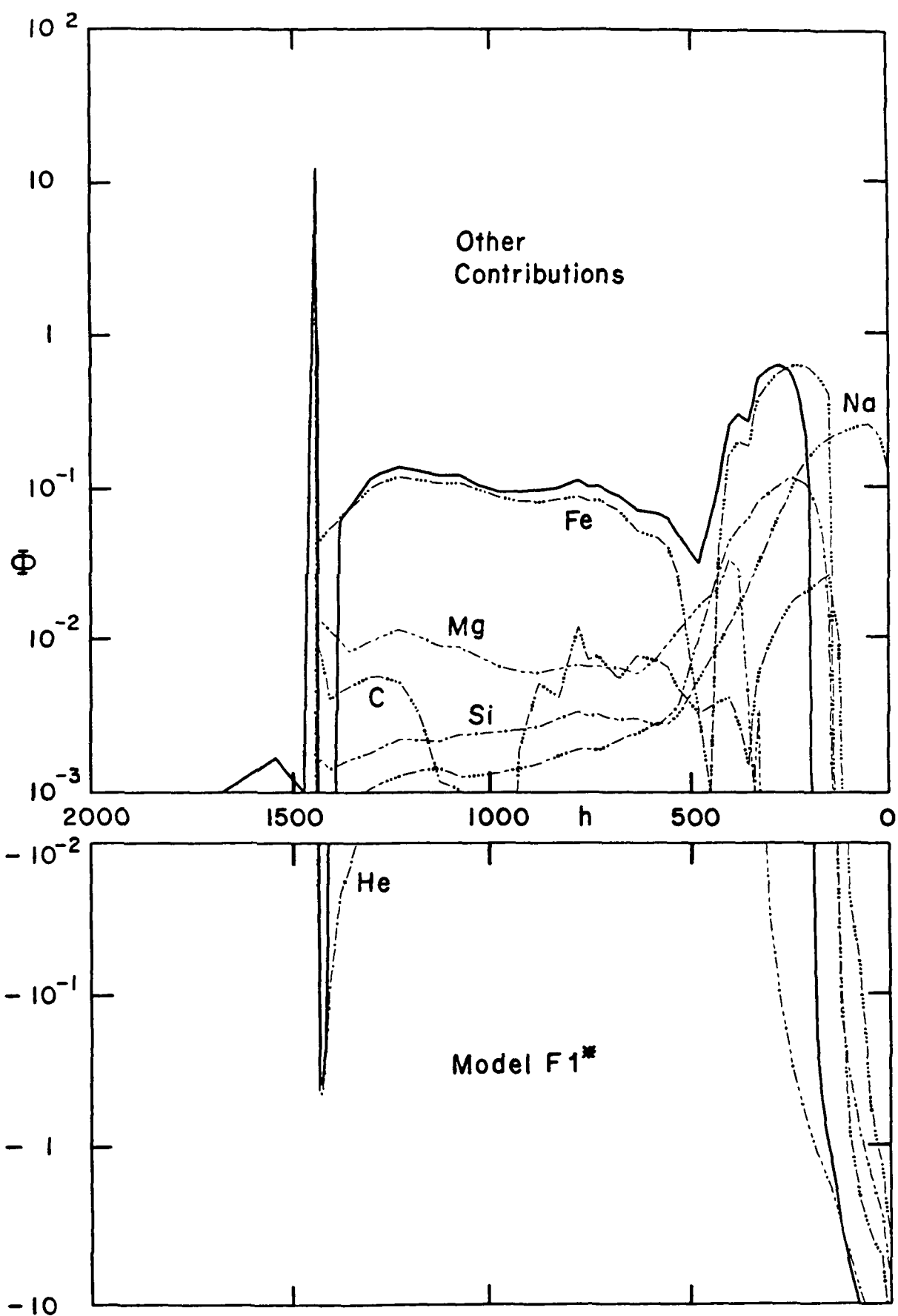


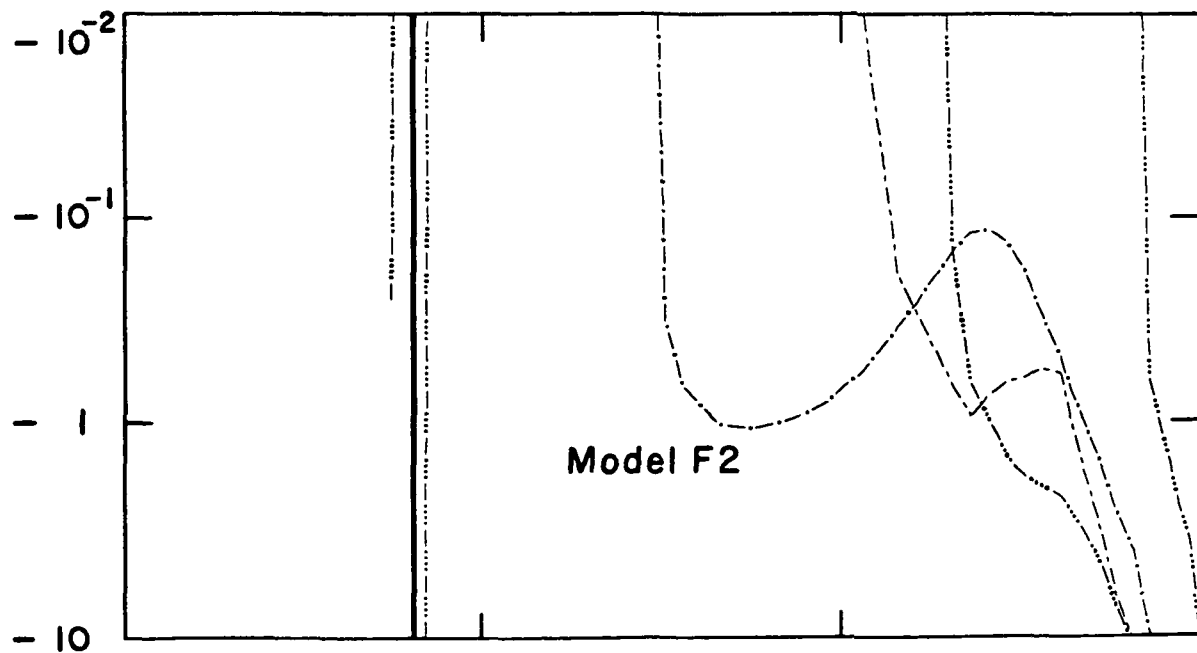
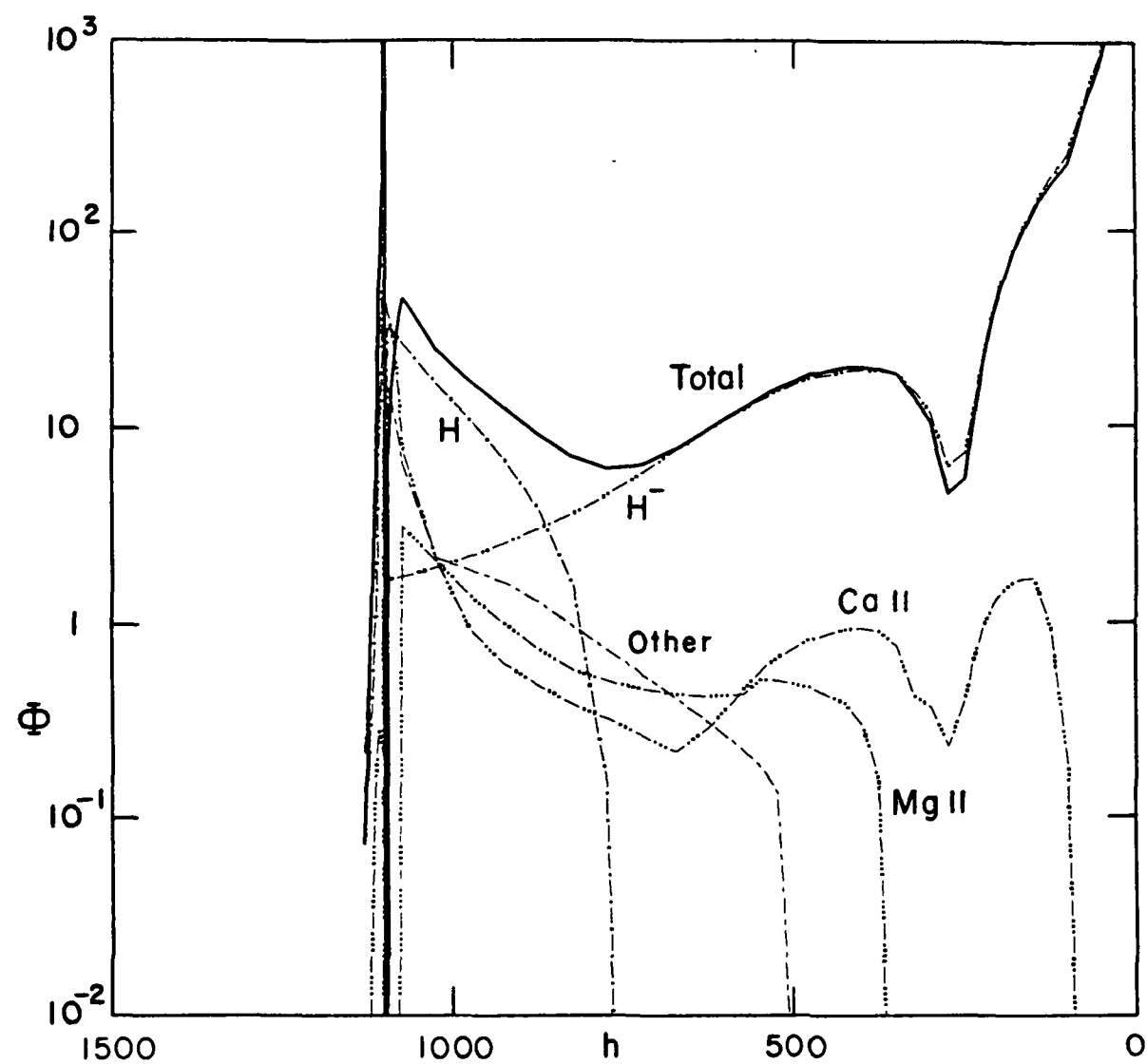


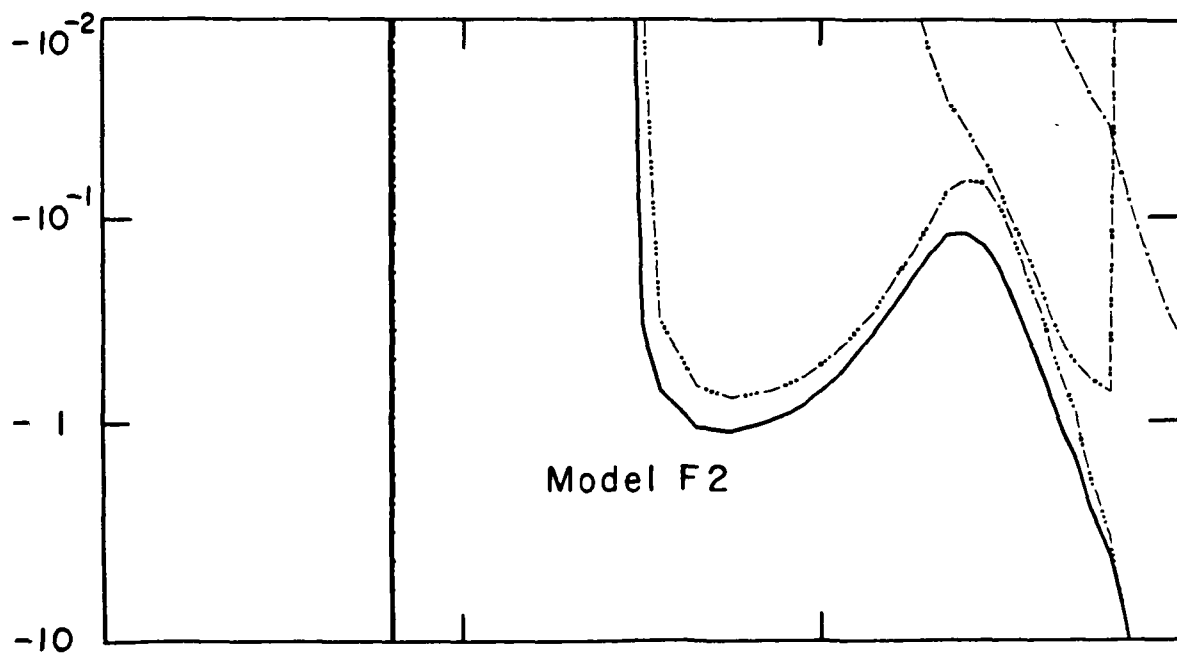
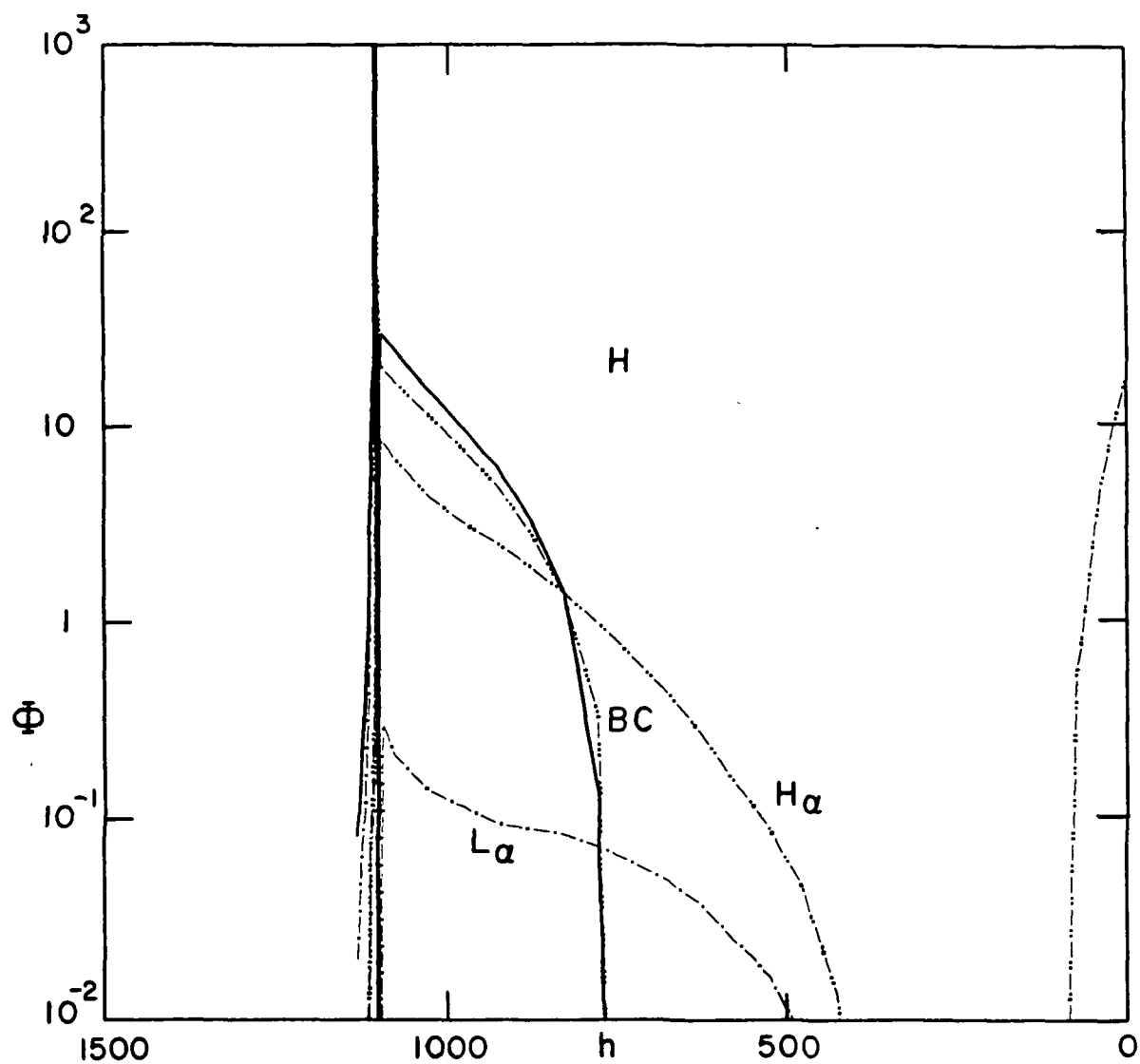


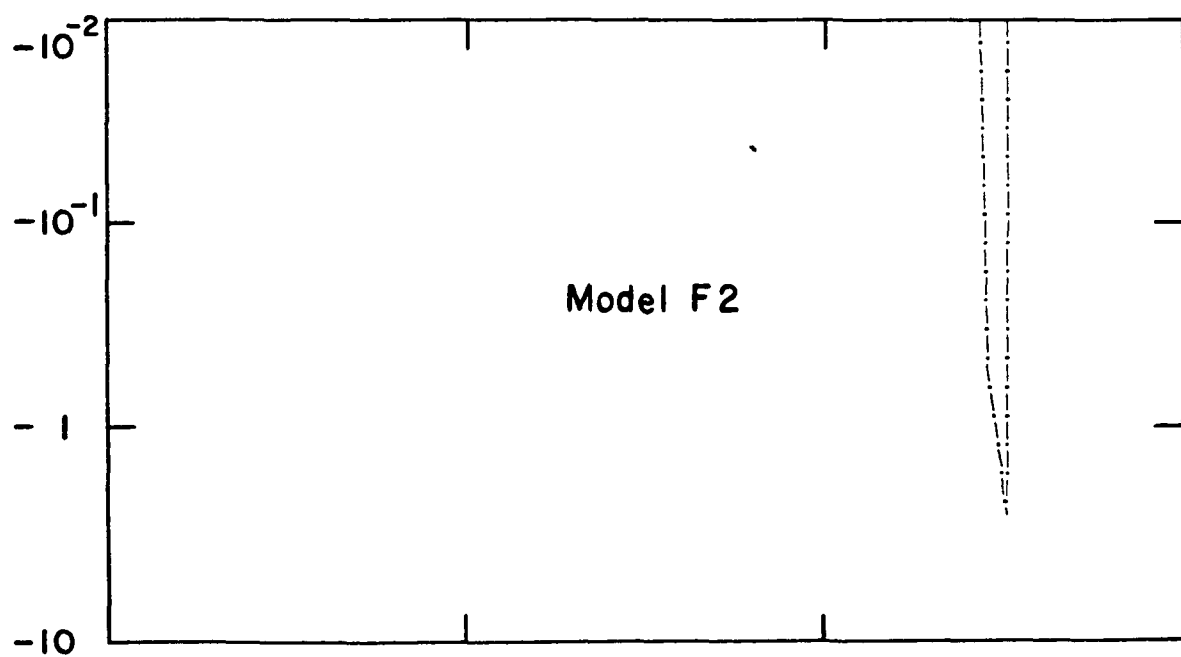
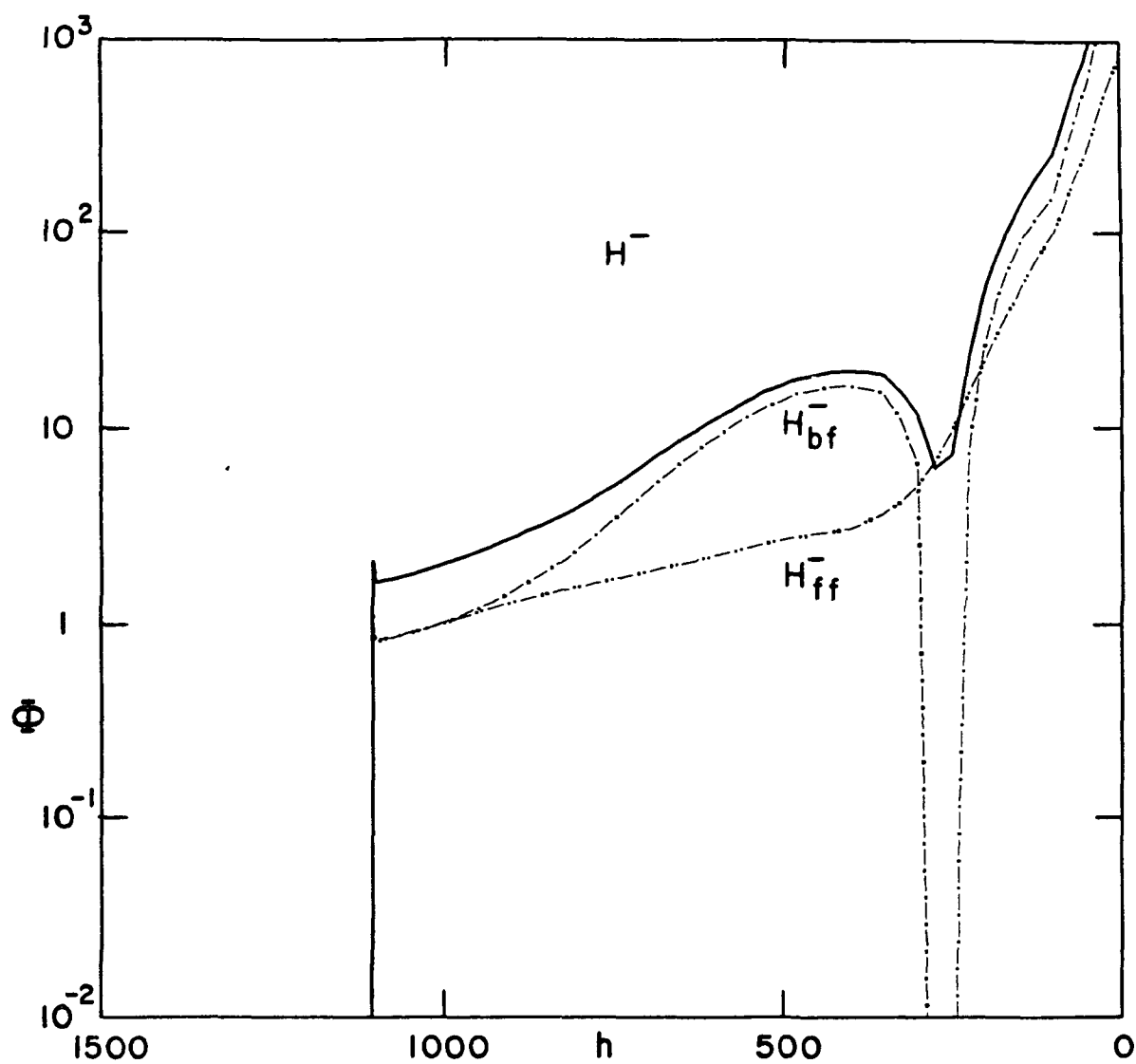


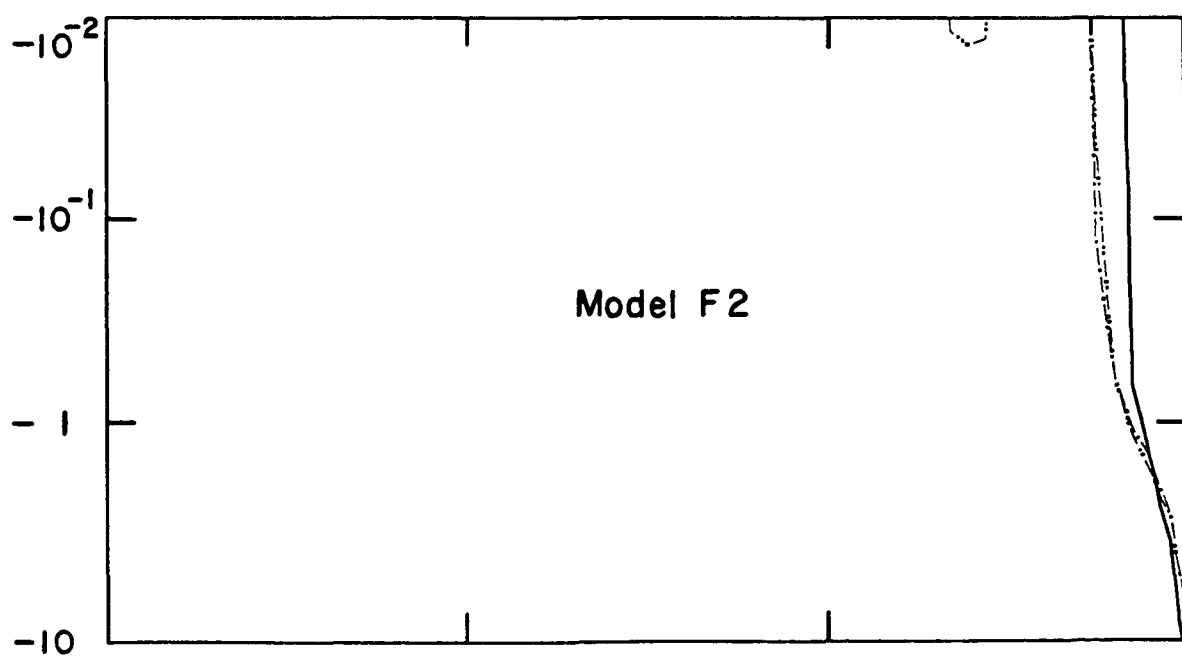
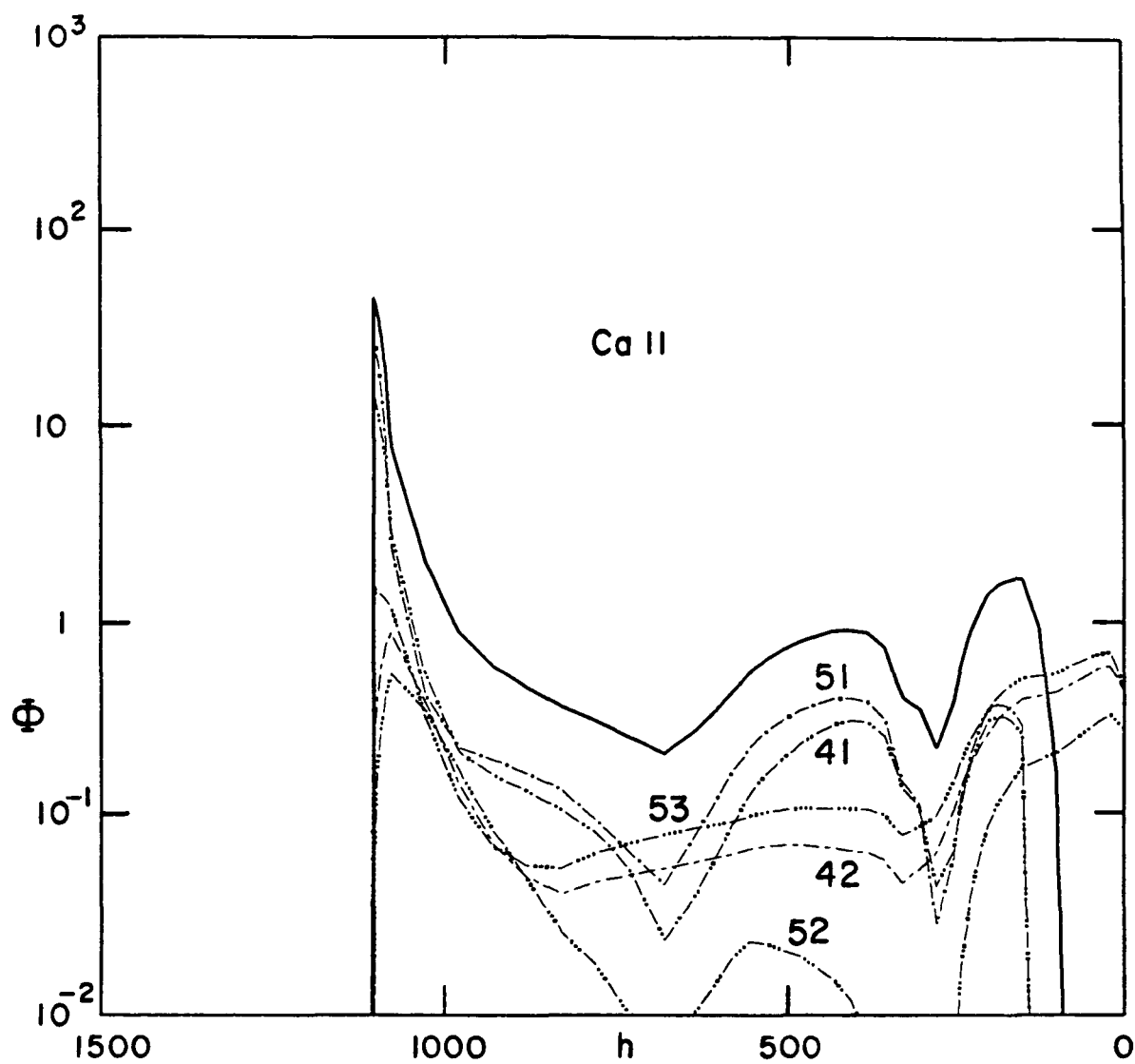


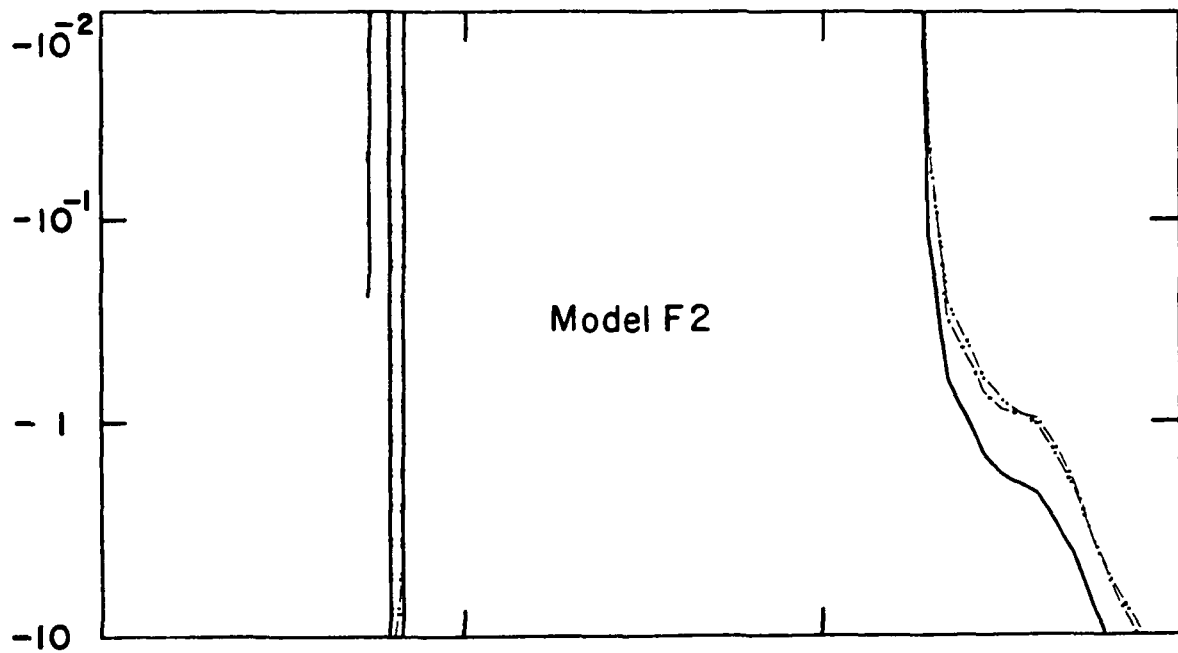
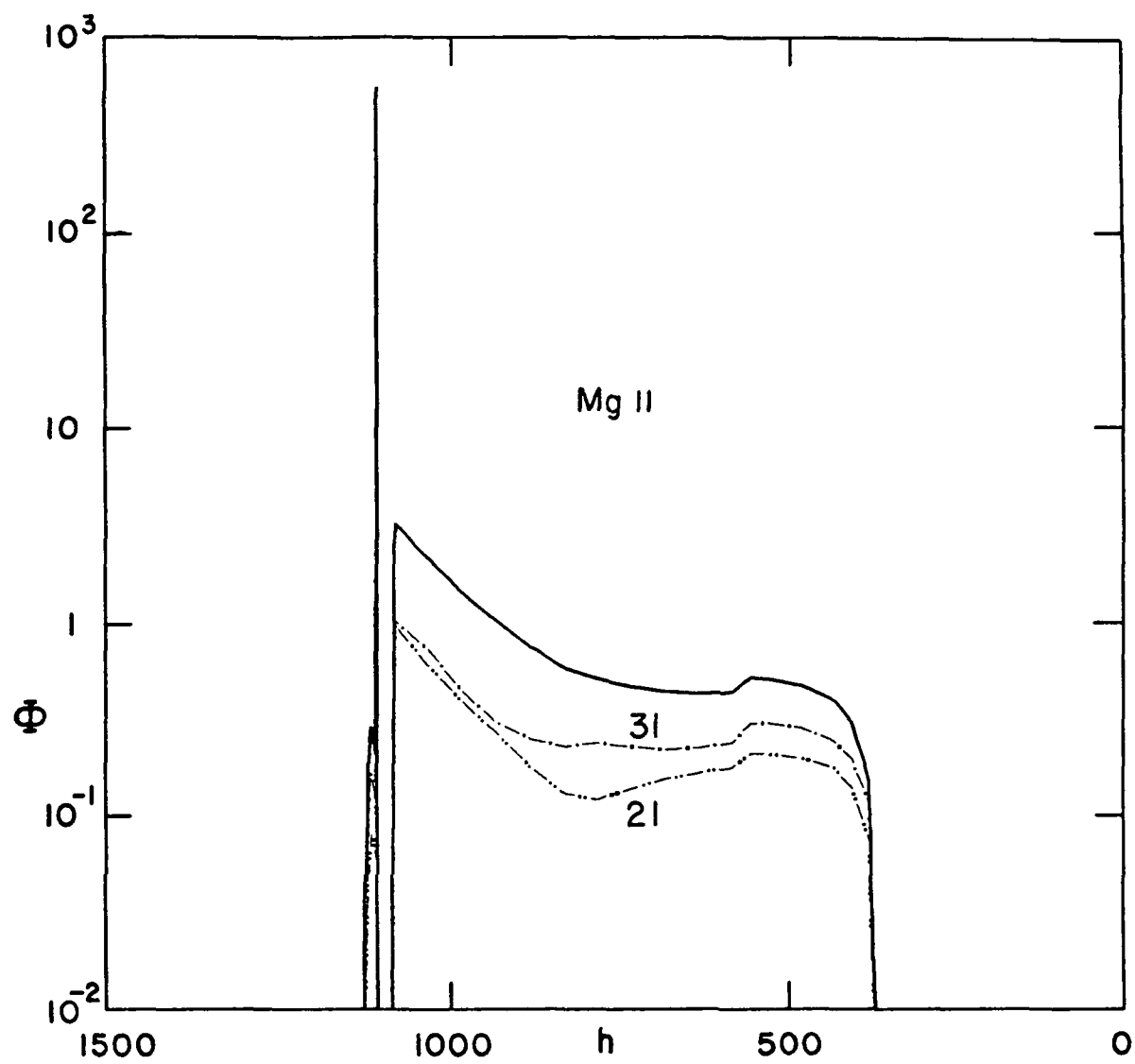


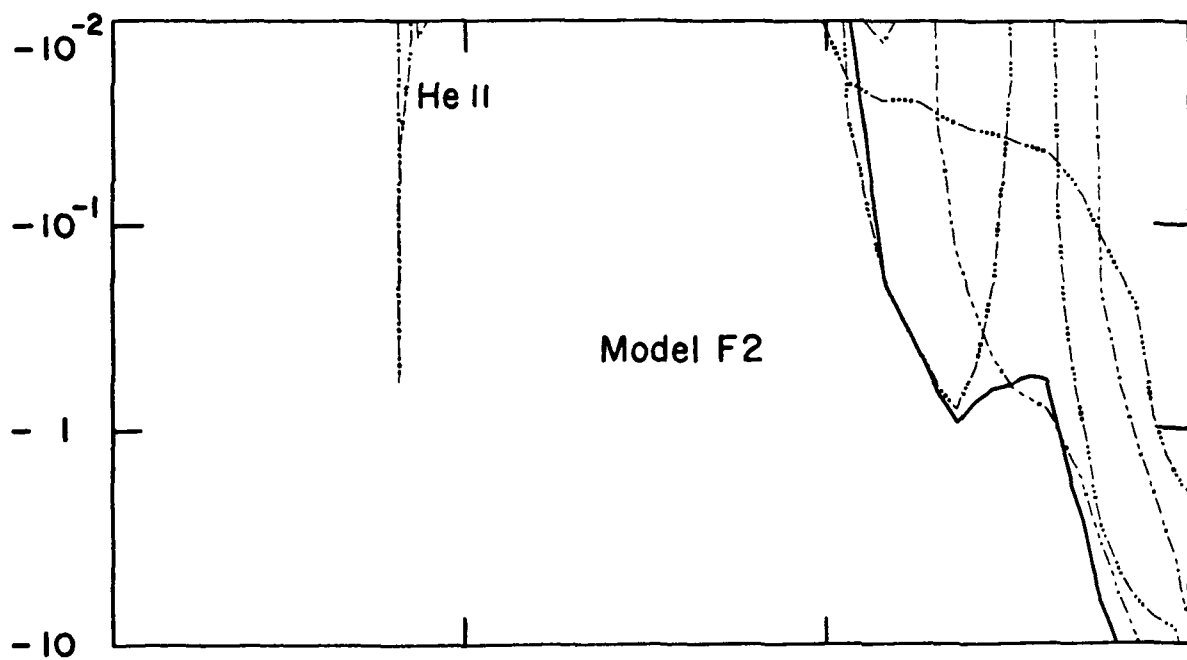
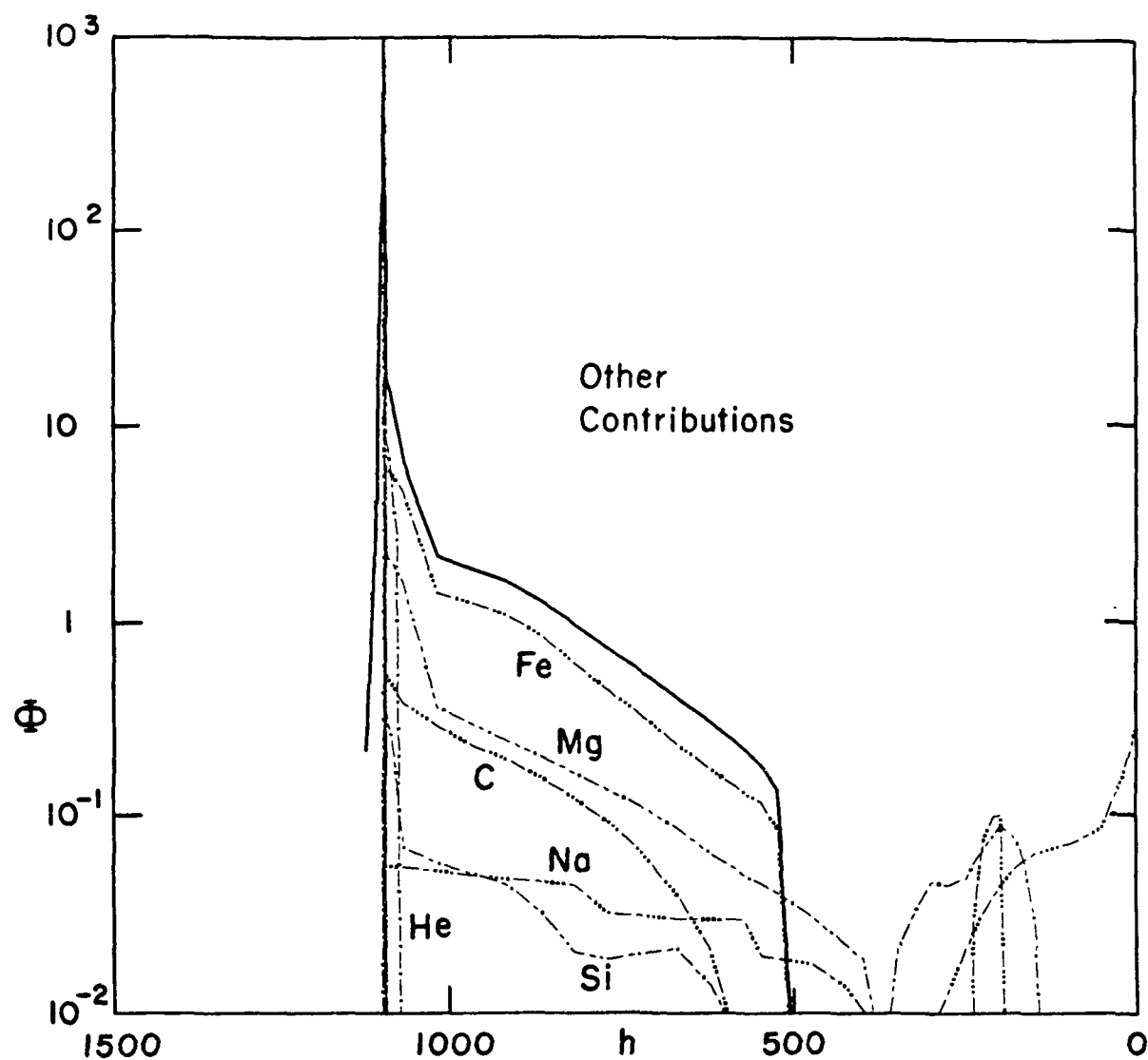


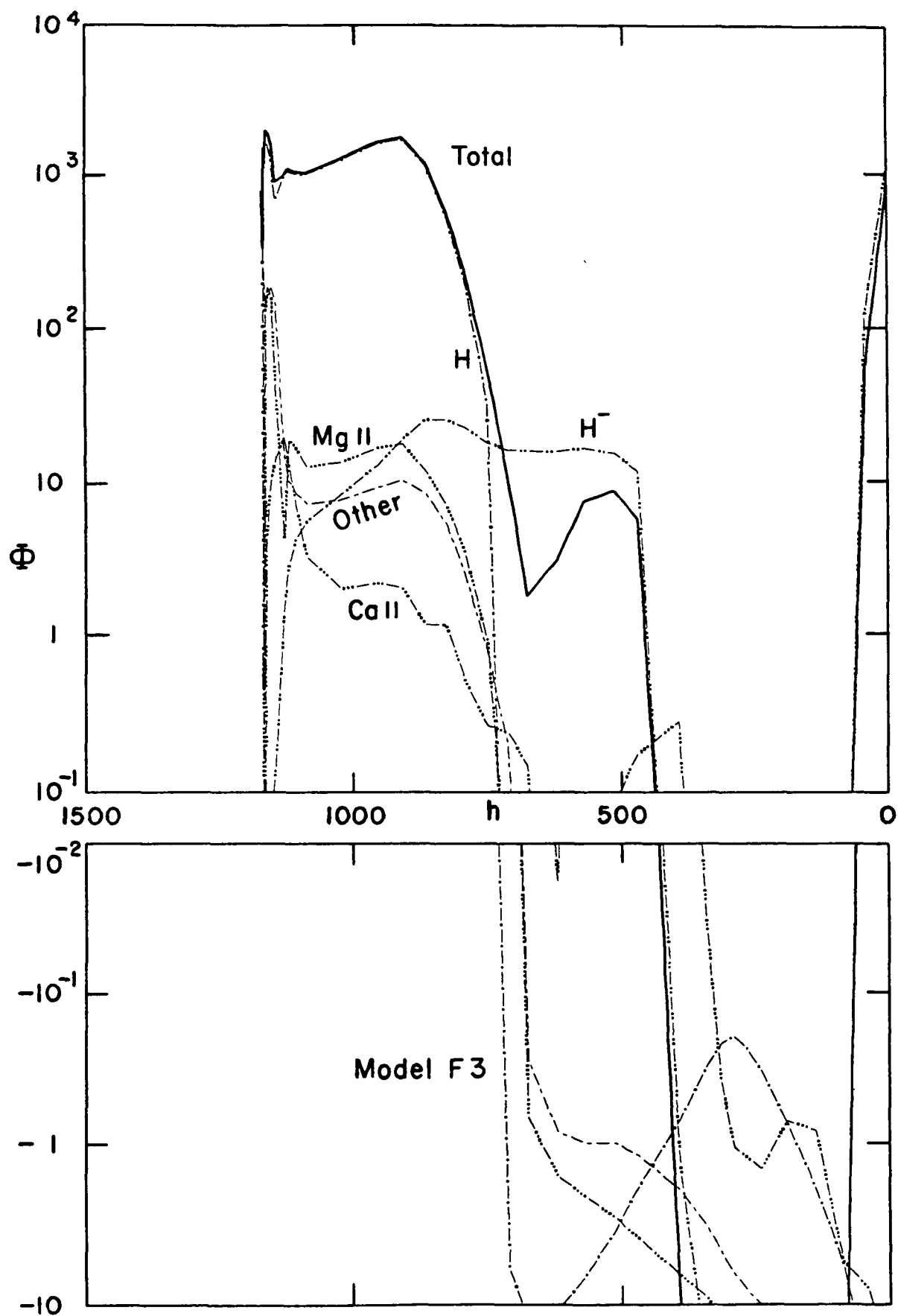


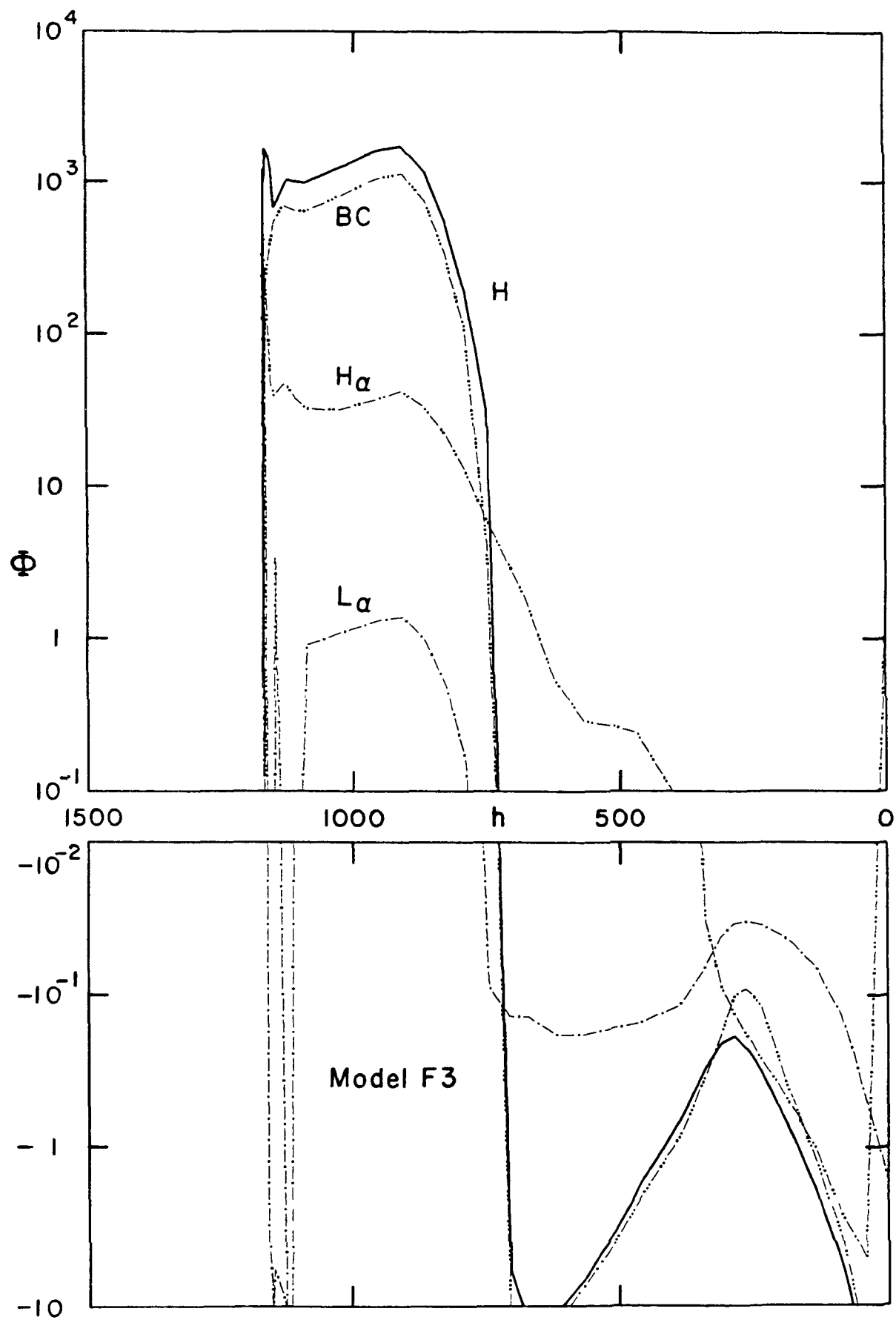


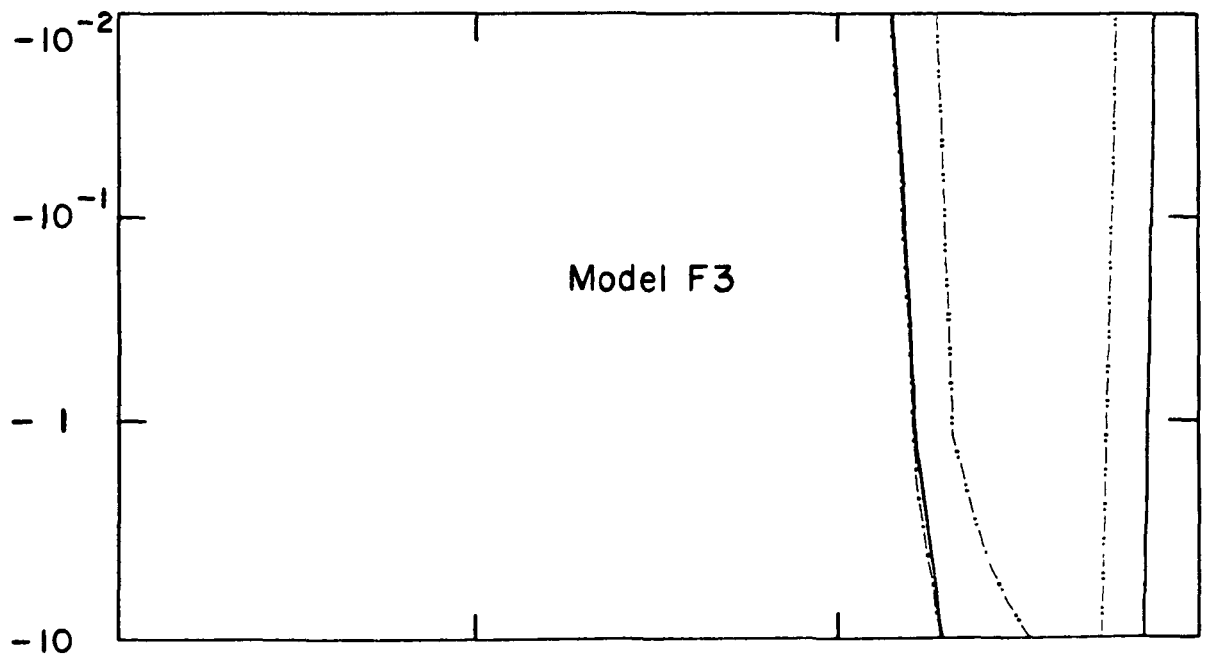
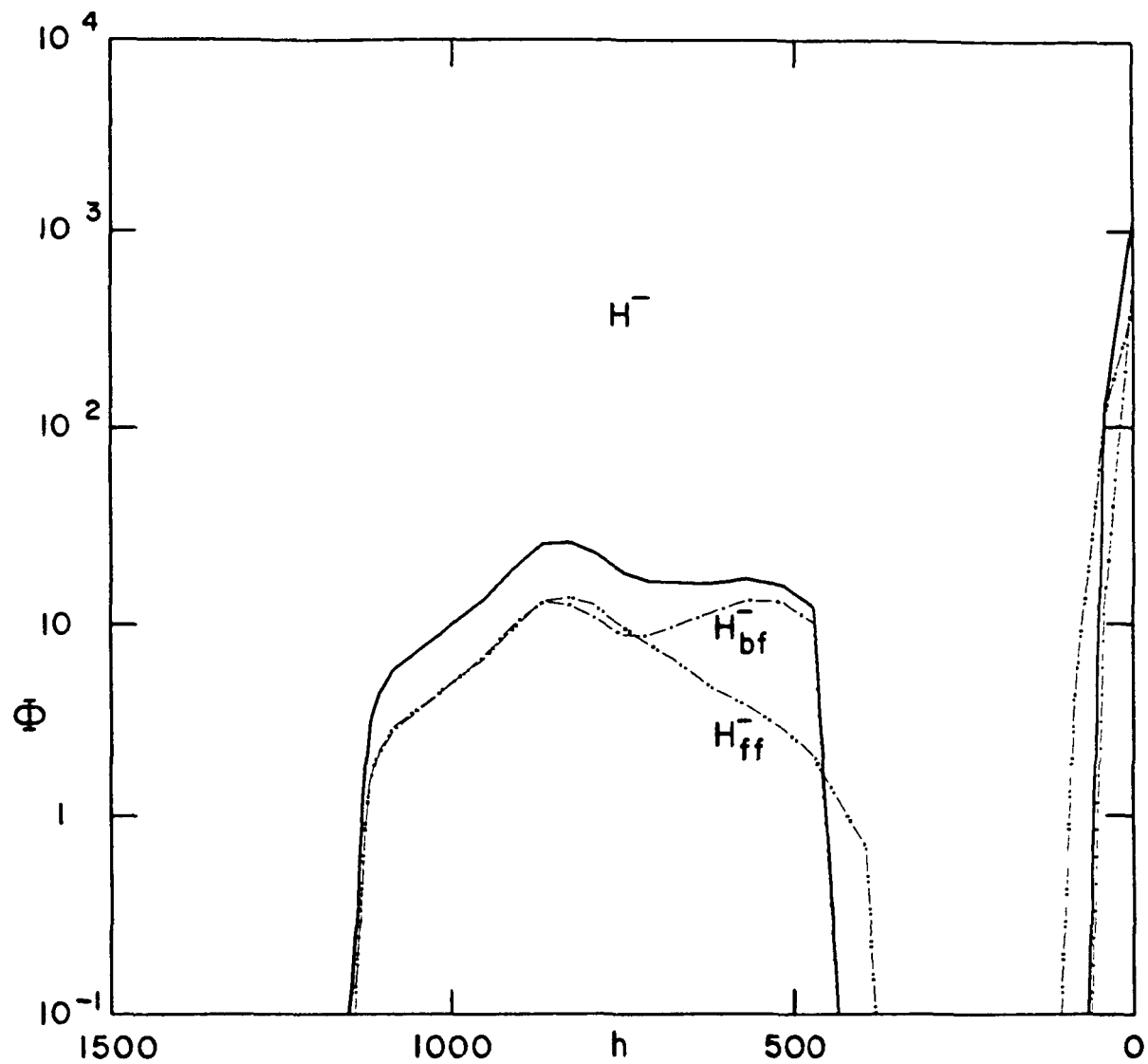


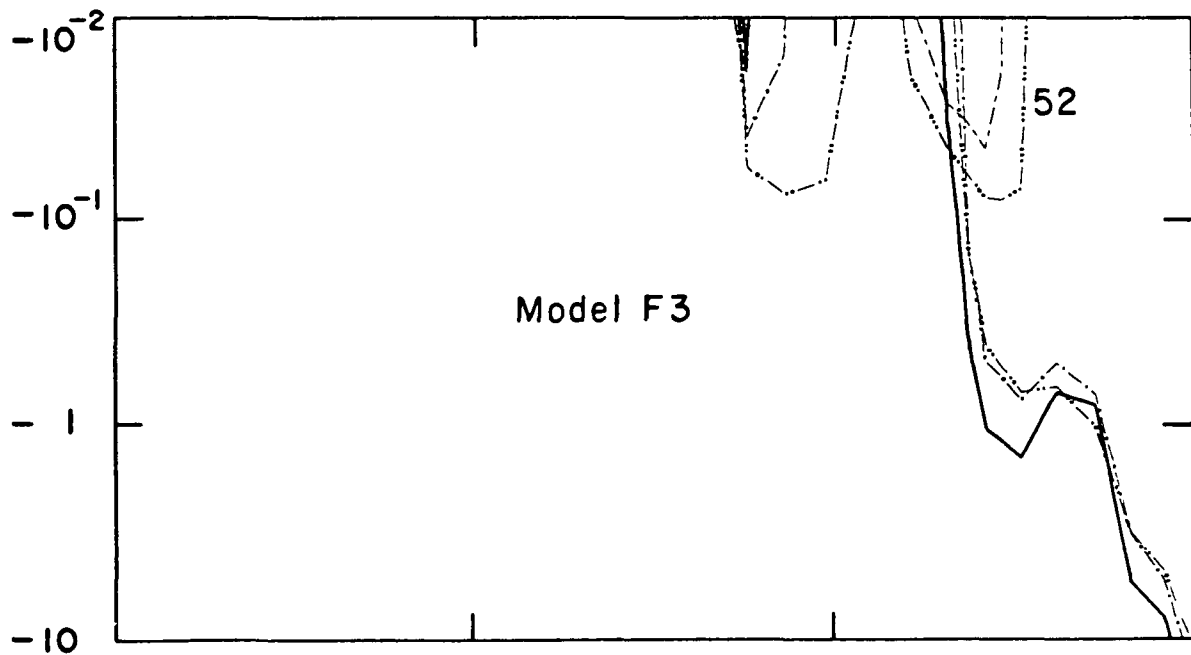
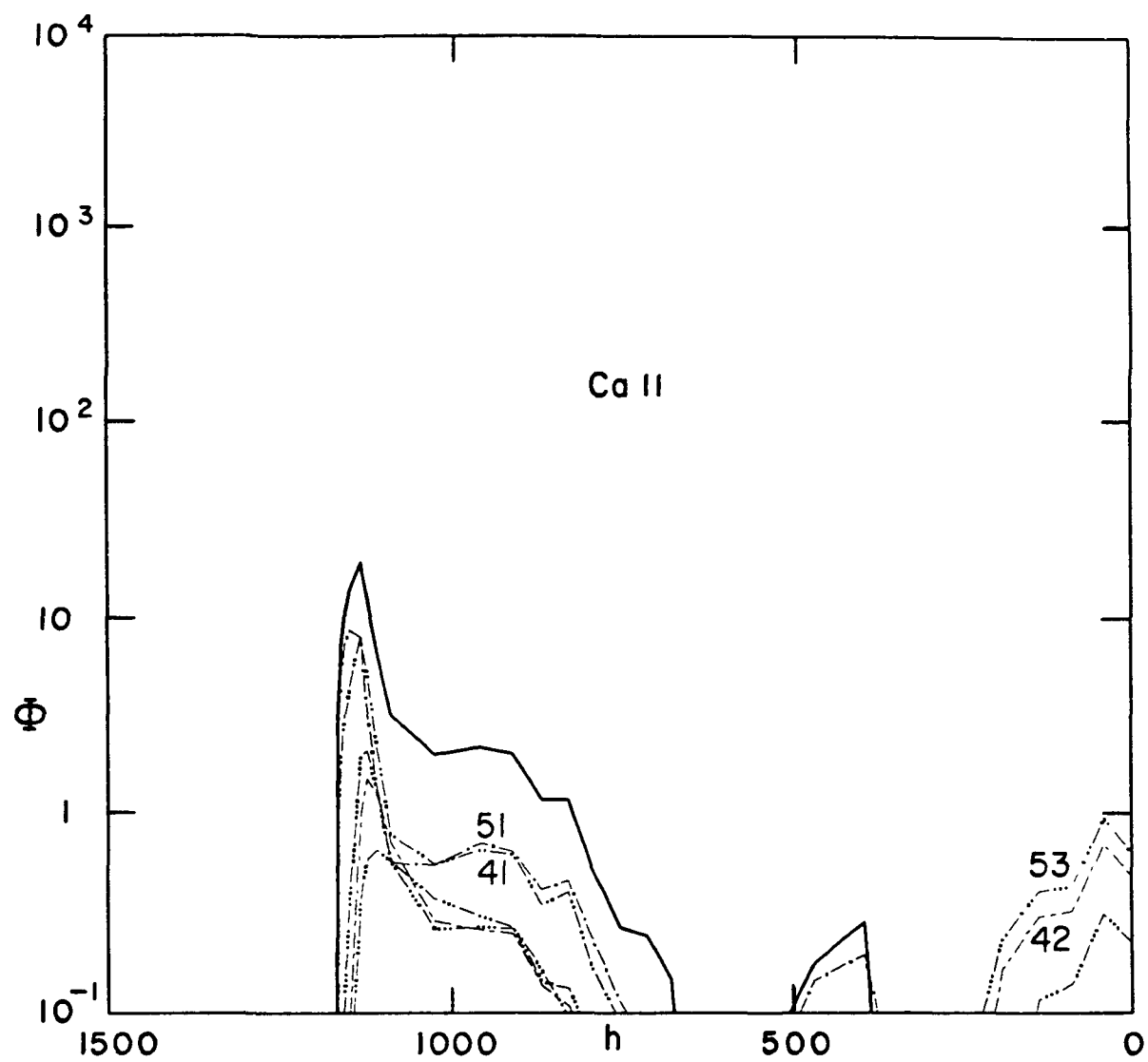


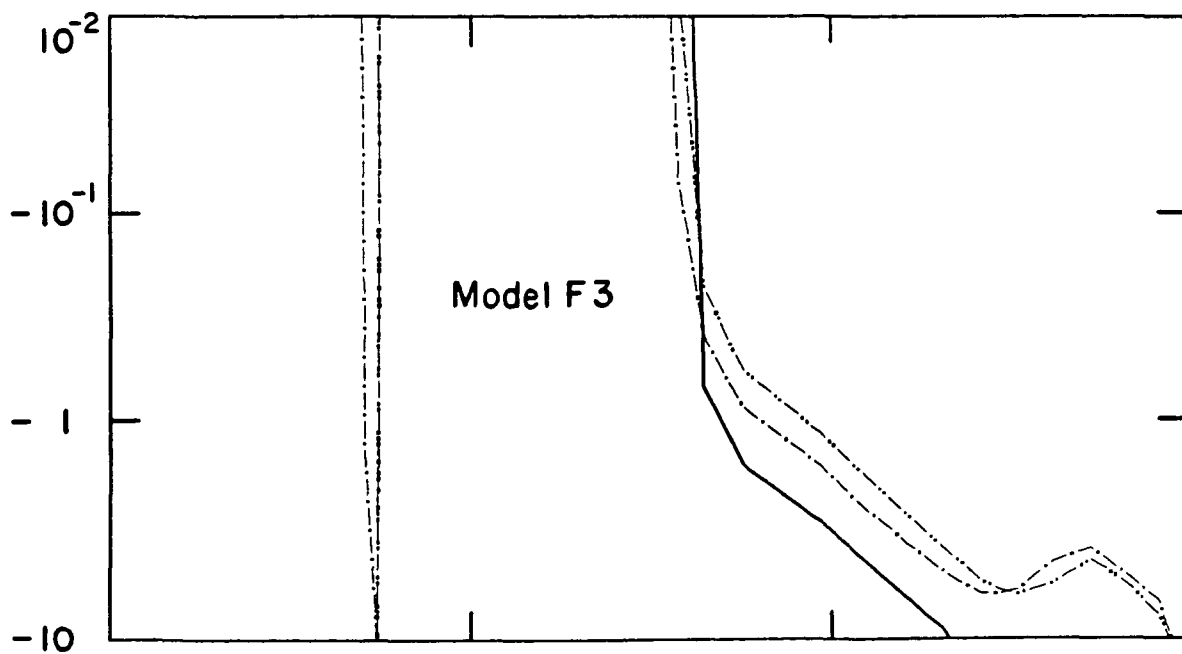
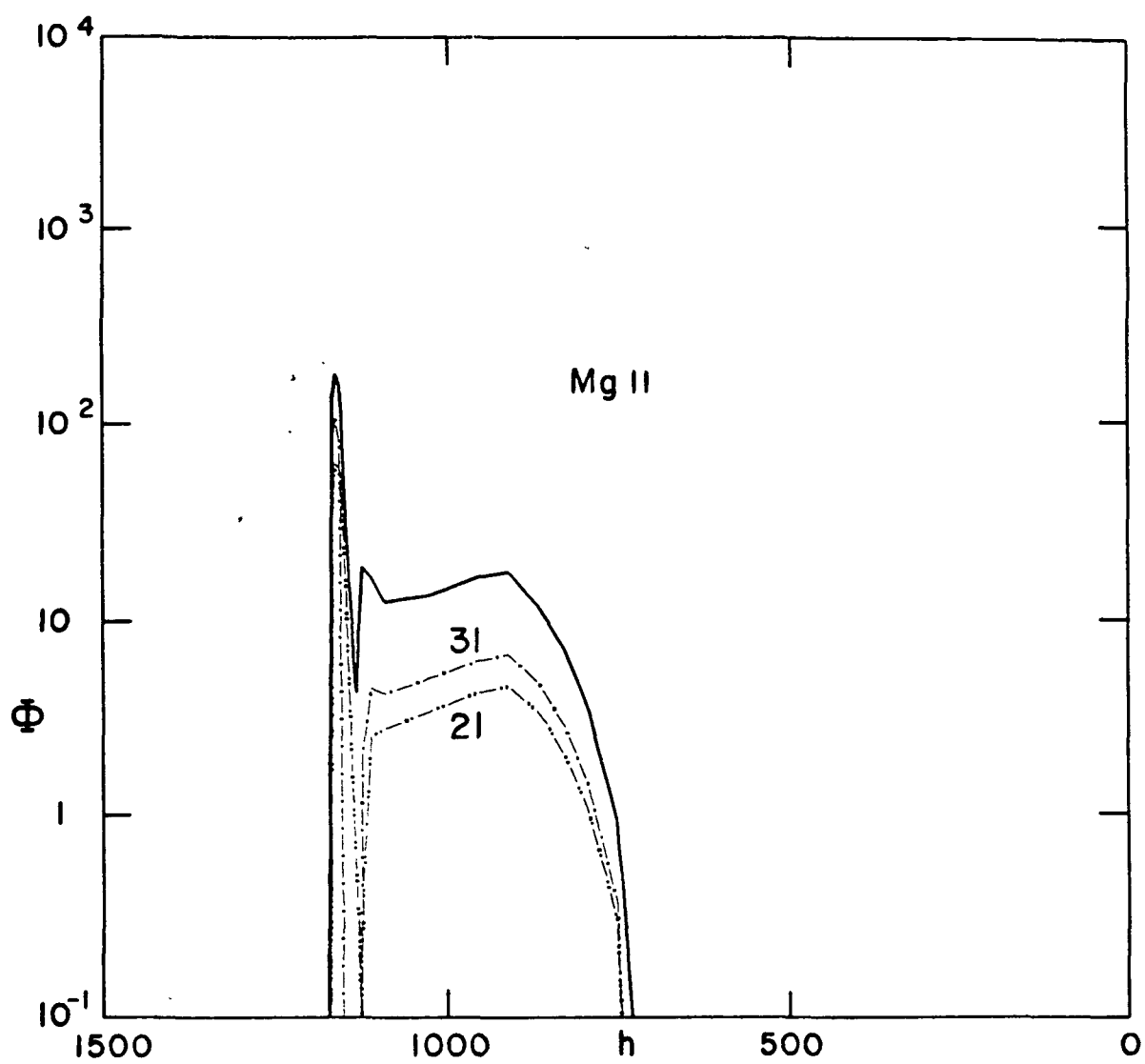


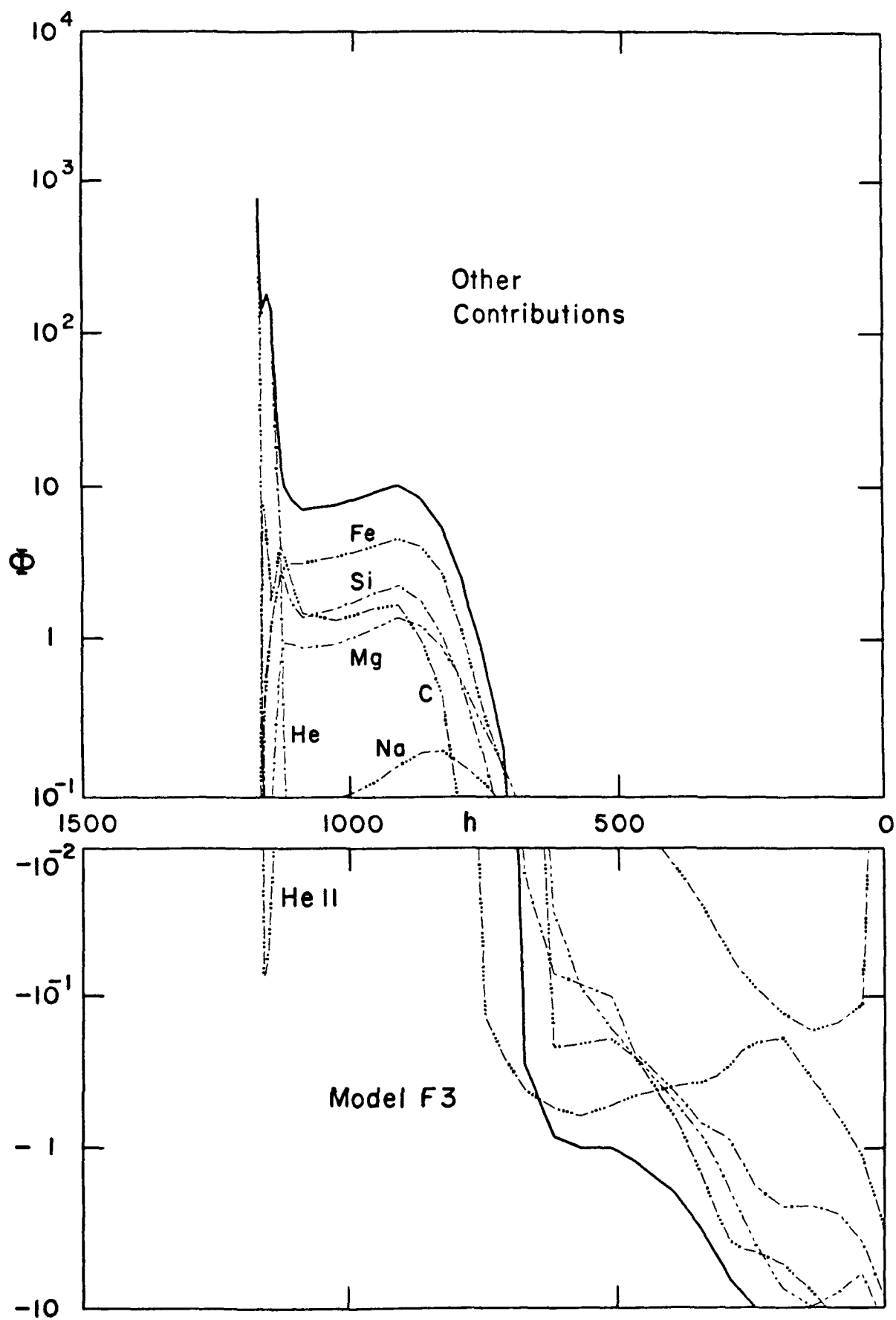












by decreasing the temperature at the depths that determine the values of J_ν . See the papers by Emslie and by Mauas and Machado in this volume. The excessively negative values of Φ in the minimum temperature region for model F3 suggest that the substantial contribution to J_ν produced in the upper chromosphere is reasonable only if S_ν , and hence the temperature, were higher in the minimum region. Radiation from the upper chromosphere apparently could produce a temperature enhancement in the minimum region.

5. CONCLUSIONS

The calculations presented here provide insights on how the observed chromospheric flare spectrum is produced. The results also suggest numerous improvements that should be made in the model calculations in order to interpret observations in better detail.

The upper chromospheric contribution to white light flare emission is due to H, not H^- , but H^- plays an important role deeper in the atmosphere, and there could be a temperature enhancement in the deeper layers as a result of enhanced radiation produced in the upper chromosphere.

Further work is needed to account for the important radiative processes, as well as time-dependent and kinetic processes, that affect the lower atmosphere in solar flares.

ACKNOWLEDGEMENTS

The authors are grateful to Donald Neidig, Per Maltby, and Roberto Falciani for useful discussions, and to Rudolf Loeser for his extensive help with the calculations reported here. This research was supported by NASA grant NSG-7054.

REFERENCES

- Aboudarham, J., and Henoux, J. C. 1986, *Astron Astrophys*, in press.
- Avrett, E. H. 1985, in *Chromospheric Diagnostics and Modeling*, ed. B. W. Lites, National Solar Observatory, Sunspot, NM, 67.
- Avrett, E. H., Kurucz, R. L., and Loeser, R. 1984, *Bull Amer Astron Soc*, **16**, 450.
- Boyer, R., Machado, M. E., Rust, D. M., and Sotirovski, P. 1985, *Solar Phys* **98**, 255.
- Canfield, R. C., and van Hoosier, M. E. 1980, *Solar Phys*, **67**, 339.
- Canfield, R. C. *et al.* 1980a, in *Solar Flares - A Monograph from Skylab Workshop II*, ed. P. A. Sturrock, Colorado Associated Univ. Press, 231.
- _____. 1980b, *ibid*, 451.
- Carbon, D. F. 1984, in *Methods of Radiative Transfer*, ed. W. Kalkofen, Cambridge, Univ. Press, 395.
- Cohen, L., Feldman, U., and Doschek, G. A. 1978, *Astrophys. J. Suppl.*, **37**, 393.
- deFeiter, L. D. 1966, *Rech. Astron Obs Utrecht*, **18**, No. 2.
- Donati-Falchi, A., Falciani, R., and Smaldone, L. A. 1984, *Astron Astrophys* **131**, 256.
- _____. 1985, *ibid*, **152**, 165.
- Emslie, A. G., Brown, J. C., and Machado, M. E. 1981, *Astrophys J.*, **246**, 337.
- Henoux, J.-C., and Nakagawa, Y. 1977, *Astron Astrophys.*, **57**, 105.
- Hiei, E. 1982, *Solar Phys.*, **80**, 113.
- Kurucz, R. L. 1985, *Bull. Amer. Astron Soc.*, **17**, 640.
- Kurucz, R. L., and Avrett, E. H. 1981, *Smithsonian Astrophys Obs Spec. Rept.* No. 391.
- Lemaire, P., Choucq-Bruston, M., and Vial, J.-C. 1984, *Solar Phys*, **90**, 63.
- Lites, B. W., and Cook, J. W. 1978, *Astrophys. J.*, **228**, 5891.
- Maltby, P., Avrett, E. H., Carlsson, M., Kjeldseth-Moe, O., Kurucz, R. L., and Loeser, R. 1986, *Astrophys. J.*, in press.
- Machado, M. E., Avrett, E. H., Vernazza, J. E., and Noyes, R. W. 1980, *Astrophys. J.*, **242**, 336.
- Machado, M. E., and Emslie, A. G. 1979 *Astrophys J.*, **232**, 903.
- Machado, M. E., Emslie, A. G., and Brown, J. C. 1978, *Solar Phys*, **58**, 363.
- Machado, M. E., and Linsky, J. L. 1975, *Solar Phys*, **42**, 395.
- Machado, M. E., and Rust, D. M. 1974, *Solar Phys*, **38**, 499.
- Neidig, D. F., and Cliver, E. 1983, AFGL-TR-83-0257, Hanscom AFB, MA.
- Neidig, D. F., and Wiborg, P. H. 1984, *Solar Phys.*, **92**, 217.
- Svestka, Z. 1965, *Advances Astron Astrophys*, **3**, 119.

- Svestka, Z. 1966. *Space Sci Rev*, **5**, 388.
- _____. 1976, *Solar Flares*, D. Reidel Publ. Co.
- Vernazza, J. E., Avrett, E. H., and Loeser, R. 1973, *Astrophys. J.*, **184**, 605.
- _____. 1981, *Astrophys J Suppl.*, **45**, 635.
- Zirin, H., and Hirayama. T. 1985, *Astrophys. J.*, **299**, 536.
- Zirin, H., and Neidig, D. F. 1981, *Astrophys J. (Lett.)*, **248**, L45.